
Doctoral Dissertations

Student Theses and Dissertations

Fall 2011

First-principles studies of complex hydrides for Li-ion battery and hydrogen storage applications

Timothy Hudson Mason

Follow this and additional works at: https://scholarsmine.mst.edu/doctoral_dissertations



Part of the [Physics Commons](#)

Department: Physics

Recommended Citation

Mason, Timothy Hudson, "First-principles studies of complex hydrides for Li-ion battery and hydrogen storage applications" (2011). *Doctoral Dissertations*. 1809.

https://scholarsmine.mst.edu/doctoral_dissertations/1809

This thesis is brought to you by Scholars' Mine, a service of the Missouri S&T Library and Learning Resources. This work is protected by U. S. Copyright Law. Unauthorized use including reproduction for redistribution requires the permission of the copyright holder. For more information, please contact scholarsmine@mst.edu.

FIRST-PRINCIPLES STUDIES OF COMPLEX HYDRIDES FOR
LI-ION BATTERY AND HYDROGEN STORAGE APPLICATIONS

by

TIMOTHY HUDSON MASON

A DISSERTATION

Presented to The Graduate Faculty of the
Missouri University of Science and Technology

and

University of Missouri-St.Louis

In Partial Fulfillment of the Requirements for the Degree

DOCTOR OF PHILOSOPHY

in

PHYSICS

2011

Approved by:

Eric Majzoub, Advisor
Julia Medvedeva, Co-Advisor
Keith Stein
Alexei Yamilov
Philip Fraundorf

ABSTRACT

We employ density functional theory in a computational study of two energy storage systems.

In the first, we explore the thermodynamic viability of light metal hydrides as a high capacity Li-ion battery negative electrode. Given a set of solid-state and gas-phase reactants, we have determined the phase diagram in the Li-Mg-B-N-H system in the grand canonical ensemble as a function of lithium electrochemical potential. We present computational results for several new conversion reactions with predicted capacities between 2400 and 4000 mAhg⁻¹ that are thermodynamically favorable and that do not involve gas evolution. We provide experimental evidence for the reaction pathway on delithiation for the compound Li₄BN₃H₁₀ and compare with our theoretical prediction. The maximum volume increase for these materials on lithium insertion is significantly smaller than that for Si, whose 400% expansion hinders its cyclability.

In the second study, we attempt to gain understanding of recent experimental results of lithium borohydride nanoconfined in highly ordered nanoporous carbon. The carbon environment is modeled as a single sheet of graphene, and adsorption energies are calculated for nanoparticles of the constituent phases of LiBH₄ desorption processes (LiBH₄, LiH, lithium and boron). We find good agreement with previous studies of a single lithium atom adsorbed onto graphene. We predict that infiltrated LiBH₄ will decompose such that boron is trapped in carbon vacancies, and that the resulting boron doping is required to achieve negative wetting energies for the remaining LiBH₄. Desorption enthalpies are found to increase with shrinking cluster sizes, suggesting that the observed lowering of desorption temperatures is a kinetic effect although interactions with the carbon surface itself are predicted to have an overall effect of decreasing the desorption enthalpy.

ACKNOWLEDGMENTS

I would like to thank my advisor Dr. Eric Majzoub for teaching me his methods as well as guiding me through the processes of computational research, and to team members Xiangfeng Liu and David Peaslee for their collaboration. I wish to thank the Boeing Company for funding the majority of my graduate school education and for the patience of my managers Thomas Cavedine, Ron Krull, and James Nischwitz for their flexibility, which allowed me to pursue this work. I also thank the NASA Missouri Space Grant Consortium and the American tax payers who fund them for a grant that funded a semester of my research. Thank you to Dr. Philip Fraundorf, Dr. Keith Stine, Dr. Julia Medvedeva, and Dr. Alexey Yamilov for serving on my dissertation committee.

Thanks to Will Lemon and Anthony Eckert for their work in reliably maintaining the computing cluster at IT-enterprises to make running my calculations a smooth affair. I thank the University of Missouri-St. Louis Department of Physics and Astronomy for delivering a quality graduate school education as well as the rich experience of a teaching assistantship.

Finally, I thank my parents Eric and Gayle, as well as my brother and sisters, Jen, Ben, Lizzy and Lydia for their support, encouragement, and a considerable number of free dinners.

TABLE OF CONTENTS

	Page
ABSTRACT	iii
ACKNOWLEDGMENTS	iv
LIST OF FIGURES	viii
LIST OF TABLES	xi
SECTION	
1 INTRODUCTION	1
1.1 LITHIUM-ION BATTERIES	3
1.1.1 Capacity	4
1.1.2 Insertion and Conversion Materials	5
1.2 FUEL CELLS AND HYDROGEN STORAGE	8
1.3 MOTIVATION AND DISSERTATION OUTLINE	11
2 COMPUTATIONAL METHODS	14
2.1 INTRODUCTION	14
2.2 DENSITY FUNCTIONAL THEORY	15
2.2.1 DFT Beginnings	15
2.2.2 Exchange-Correlation Functional	17
2.2.3 DFT in a Periodic Lattice	18
2.2.4 Psuedopotentials	19
2.2.5 Projector Augmented Wave Method	22

2.3	AN EXAMPLE OF A FIRST PRINCIPLES SUCCESS: UNDERSTANDING TRANSITION METAL HYDRIDES	25
2.4	REACTION ENTHALPIES OF METAL HYDRIDES: PHASE DIAGRAMS FROM FIRST PRINCIPLES	28
2.5	PHONON CALCULATIONS	33
2.6	SURFACE CALCULATIONS WITH DFT	36
2.7	PROTOTYPE ELECTROSTATIC GROUND STATES (PEGS)	39
2.7.1	Complex Ionic Compounds and Hydrogen Storage	40
2.7.2	The PEGS Method	41
2.7.3	Nanopegs	44
3	DFT PREDICTIONS OF HIGH-CAPACITY METAL HYDRIDE CONVERSION MATERIALS FOR LI-ION BATTERIES	46
3.1	INTRODUCTION TO LITHIUM-ION BATTERY MA- TERIALS	46
3.2	LINEAR PROGRAMMING	49
3.3	EXPERIMENTAL METHODS	53
3.4	RESULTS AND DISCUSSION	54
3.5	INCLUSION OF BORONITRIDE	64
3.6	INCLUSION OF CLOSOBORANES	67
3.7	CHEMICAL POTENTIAL FOR GAS PHASES	67
3.8	CONCLUSIONS	69
4	DFT STUDY OF NANOCUSTER LITHIUM BOROHYDRIDE ENERGETICS ON CARBON NANOSCAFFOLDS	72
4.1	INTRODUCTION	72

4.2	METHODS	75	
4.2.1	DFT Methods	75	
4.2.2	Approximations	76	
4.2.3	Calculations	79	
4.3	CONFIGURATION STUDIES	81	
4.3.1	Lithium	81	
4.3.2	Boron	84	
4.3.3	Lithium Hydride	84	
4.3.4	Lithium Borohydride	87	
4.4	WETTING ENERGIES	87	
4.5	VACANCIES	89	
4.6	MAGNESIUM HYDRIDE WETTING	93	
4.7	BORON DOPED GRAPHENE SHEETS	93	
4.8	COMPARISON OF SURFACE EFFECTS WITH SIZE EFFECTS	95	
4.9	CONCLUSION	98	
5	CONCLUSIONS	99	
APPENDICES			
A.	COMPUTATIONAL SCRIPTS	102	
B.	PERMISSIONS FOR FIGURES	136	
BIBLIOGRAPHY			138
VITA			146

LIST OF FIGURES

Figure	Page
1.1 Schematic of lithium-ion battery processes taken from a review article by Tarascon and Armand.[76]	4
1.2 Structure of LiCoO_2	6
1.3 Arrhenius plots showing the kinetics in terms of rates of hydrogen desorption of NaAlH_4 when doped with titanium-halide catalysts.	10
2.1 A figure from a paper by Payne et al. illustrating the pseudo wave function.	21
2.2 Electron density change as a result of step 3.	26
2.3 Metal hydride formation energies of the 3d transition metals in various crystal structures.	27
2.4 Van't Hoff plots for hydrogen desorption reactions by Ackbarzadeh et al.	32
2.5 An example of a large supercell with a vacuum layer used to model a graphene surface.	36
2.6 Convergence plot of DFT energy vs. the length of the vacuum layer.	37
2.7 Structure for NaAlH_4 highlighting the complex Al-H anion.	41
3.1 TEM imagery of silicon nanowires developed to combat the pulverization effects of silicon volume expansion taken from the work of Chan et al.[12]	47
3.2 Experimental I-C curve for lithiation (red) and delithiation (blue) of $\text{Li}_4\text{BN}_3\text{H}_{10}$ infiltrated into nanoporous carbon.	55
3.3 Idealized I-C curve predicted by GCLP for both lithiation (red) and delithiation (blue) of $\text{Li}_4\text{BN}_3\text{H}_{10}$	55

3.4	Pseudo-ternary phase diagram with N:H ratio of 1:2 in which $\text{Mg}(\text{NH}_2)_2$ is the highest capacity material.	56
3.5	Pseudo-ternary phase diagram with no nitrogen content in which MgB_2H_8 is the highest capacity material.	57
3.6	Pseudo ternary phase diagrams for four nitrogen-hydrogen ratios.	57
3.7	Phases after lithiation of the $\text{Mg}(\text{NH}_2)_2 / \text{MgB}_2\text{H}_8$ mixture.	64
3.8	Idealized C-V plots versus Li^+/Li for selected mixtures.	65
3.9	Pseudo-ternary phase diagram with N:H ratio of 1:2 with BN included as a candidate phase.	66
4.1	TEM images of highly ordered nanoporous carbon of Liu et al.[35]	74
4.2	Configuration of graphene with fully adsorbed lithium from Medeiros et al.[48]	78
4.3	Boron adsorbate system in which the 50 nearest atoms (cyan) were allowed to relax in order to estimate the effect of the rigid sheet approximation.	78
4.4	Changes in C-C lengths as a result of a boron adsorbate.	79
4.5	Super cell of graphene sheet approximating nano porous material.	80
4.6	Charge density plot of LiBH_4 relaxed onto graphene sheet.	81
4.7	Configuration studies for lithium.	82
4.8	Configuration studies for boron.	85
4.9	Configuration studies for lithium hydride.	86
4.10	Configuration studies for lithium borohydride.	88
4.11	Wetting energies of defect free graphene sheet as compared to E_{bulk}	89

4.12 Simulated amorphous carbon with a single vacancy.	90
4.13 Relaxed wetting configuration of species in LiBH_4 desorption on the carbon vacancy.	91
4.14 LiBH_4 on a boron dopant which has been wetted with lithium.	95
4.15 Plot of desorption energies for the three reaction pathways considered.	97

LIST OF TABLES

Table	Page
2.1 Enthalpies of reaction calculated using equation 2.16 (μ_{H_2} neglected) with and without the zero point energy included. . .	30
3.1 Boundaries of the explored space of atomic quantities A_g . . .	51
3.2 First-principles DFT energies and enthalpies of formation for the anode and cathode phases at 300 K.	52
3.3 Selected reactions at 300 K.	60
3.4 Reaction 9 with closoboranes tuned to eliminate NH_3 gas. . .	68
3.5 Fugacities required for reaction stability.	71
4.1 B-H stretching and bending mode frequencies calculated at gamma by VASP linear response for bulk and various configurations of BH_4 in the vacancy.	92
4.2 Wetting energies of various compounds for 1 fu adsorbate on both a perfect graphene sheet and one with a single vacancy.	94
4.3 Reaction energies per molecule H_2 released for four reactions calculated on different surfaces. To show the change in reaction pathways between a product of LiH and metal lithium, the lower energies for each surface are in bold face.	97

1 INTRODUCTION

Many technologies responsible for the high standard of life we enjoy in modern times are dependent on the efficient and accessible storage of portable energy. Although more exotic technologies exist and continue being developed such as super capacitors, energy storage today is usually accomplished by the use of batteries because of their reliable performance within a wide range of temperature and pressure conditions. Active research also continues in fuel cells with the hopes that their theoretically higher energy and power density can be realized at practical operating conditions. In both batteries and fuel cells, energy is stored in the chemical bonds between atoms in a phase of matter, and is released via electrochemical redox reactions. The difference between a battery and a fuel cell is that batteries are a closed system in which the active masses shift between two internal electrodes of differing electrochemical potential during charge and discharge, while a fuel cell is an open system in which the active masses come from the outside as fuel during charging and exit the cell during energy extraction. Rechargeable batteries can be recharged under practical conditions simply by applying a reverse bias voltage across the electrodes making it energetically favorable for the active components to return to their charged state.

The reactions in a fuel cell, on the other hand, must be manipulated by controlling the pressure and temperature conditions to force the system to cross phase boundaries, the lines in temperature-pressure phase space that separates the hydrided phase from the dehydrided phase. The phase boundaries thus define at what conditions the desired desorption reactions take place. Low temperature systems that are nearing technical maturity exist today that use platinum or platinum alloys as a catalyst for the hydrogen redox reactions. These systems, however, are currently too expensive for broad use because of the scarcity of the catalytic elements. Searching

for ways to reduce the necessary amount of catalytic loading continues to be a large component of low temperature fuel cell research.[26] Unfortunately, within the realm of economically feasible materials, no system has yet been discovered in which the redox phase boundary exists at practical temperatures and pressures.

Hybrid systems are also being investigated such as lithium air batteries, in which lithium ions traverse an electrolyte from a standard negative electrode, to a chamber in which they react with atmospheric oxygen gas that comes from outside the system forming Li_2O . This design effectively turns the atmosphere into a cathode. These systems exhibit capacities 5 to 10 times that of a Li-ion battery bringing them in close competition with gasoline, but currently perform inadequately in terms of cyclability and power density.[16]

Because of the obstacles mentioned above for fuel cells and hybrid systems, conventional rechargeable batteries accomplish most of the energy storage for portable electronic devices despite the theoretically higher energy capacity of fuel cells. Great interest continues in engineering improvements in battery systems and in pushing fuel cells towards the realm of feasibility. Properties of interest are energy density per weight and per volume, reversibility, the number of usable charge cycles, safety, cost, practical operating conditions, and energy transfer kinetics that allow for practical charge times.[82] Many quantum mechanics based first-principles methods such as quantum chemistry or density functional theory exist that can be used to predict some of these properties for hypothetical material systems and their energy transfer reactions. One work reported in this dissertation applies these methods to search for potentially suitable materials for a negative electrode of a lithium ion battery. The study explores thermodynamically optimal materials within a system of lithium, boron, magnesium, nitrogen, and hydrogen. Although very important, investigating the kinetics will be out of scope and will have to remain the subject of further experimental or theoretical research.

1.1 LITHIUM-ION BATTERIES

The focus of Section 3 is rechargeable batteries and specifically the lithium-ion battery which is currently at the forefront of research and dominates the market for powering portable electronic devices. It has mostly displaced nickel cadmium batteries and nickel-metal hydride batteries due to its greater capacity, higher operating voltages, lower self-discharge, and easier maintainability.[26] In response to increased demand for longer operating times, its energy capacity has been more than doubled since it was introduced by Sony in 1991.[82] Most commercial lithium-ion batteries in use today consist of a graphite anode and a cobalt oxide cathode into which lithium ions freely intercalate in and out during charging and discharging. The most recent variant currently in production, however, uses an iron phosphate cathode which is attractive because of reduced cost and improved safety.[66] This battery employs the following redox reaction in the anode



while the reaction in the cathode can be written



The active mass in this case is the lithium ion which travels from anode to cathode during discharge and back to the anode during charging. Between the two anodes, there is a non-aqueous electrolyte material which is conductive for lithium ions but not for electrons.[52] The positive lithium ions thus complete the charge path within the battery, and when discharging, the electrons close the circuit externally depositing the desired energy to the load. Figure 1.1 is a graphic from a review article by Tarascon and Armand[76] that illustrates the process well. The two anode and cathode

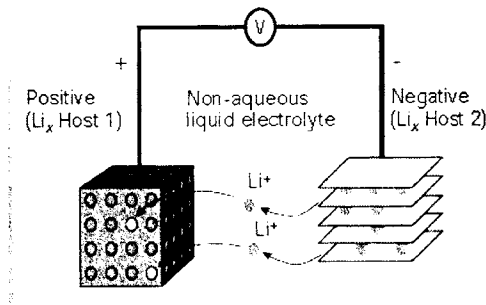
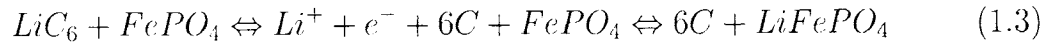


Figure 1.1: Schematic of lithium-ion battery processes taken from a review article by Tarascon and Armand.[76]

reactions can be written together as a single reaction



The voltage of the battery can be defined as the energy of the total reaction per electron. The change of enthalpy for this reaction is equal to the energy that can be delivered by the transferred electron over the load which in this case is approximately 3.3 V.

1.1.1.Capacity. As the purpose of the work in Section 3 is to research materials that improve the charge capacity per mass of the anode, the concept of capacity merits discussion. For the case of a battery, the total capacity can be expressed as equation 1.4[26]

$$C_{cell} = \frac{1}{\frac{1}{C_a} + \frac{1}{C_c} + \frac{1}{Q_m}} \quad (1.4)$$

in which C_a and C_c are the theoretical specific capacities of the anode and cathode, and Q_m is the specific mass of the non-electrode components which necessarily reduces the overall capacity per weight. The high end capacities for today's batteries are a C_a of 372 mAhg⁻¹ for carbon anodes and a C_c ranging from 160 to 200 mAhg⁻¹

for the most advanced cathode materials such as $FePO_4$. While given equation 1.4, improvements in cathode capacity would yield more dramatic improvements to overall capacity, this has so far proven very difficult[26] and it is for this reason that the anode side of the problem is being actively pursued. Assuming a typical Q_m of 130.4, a $LiFePO_4$ battery with a carbon anode has a capacity of about 65.1 mAhg^{-1} . Increasing the anode capacity to 1200 mAhg^{-1} yields a total capacity of 74.1 mAhg^{-1} after which any increase is negligible.[26] This implies that the theoretical limit to which the total capacity can be improved by only increasing anode capacity is about 14%, but it is important to note that improving anode capacity also allows for more dramatic improvements if and when cathode materials are improved.

1.1.2.Insertion and Conversion Materials. There are two classes of candidate materials for lithium ion battery electrodes. All commonly used electrodes today such as the LiC_6 anodes and the $LiCoO_2$ cathodes are known as insertion or intercalation materials. This means that the structure of the host material is not altered as it is charged apart from an increase in the lattice parameter and the insertion of lithium ions into interstitial sites. Since charging and discharging causes little or no structural change, these materials tend to have excellent reversibility repeated over several cycles. It can also lead to very good kinetics assuming that there are minimal potential barriers between the lithium sites to allow for easy ionic mobility. The layered structure of $LiCoO_2$ is shown below in Figure 1.2 in which the 2D conduction pathways for the lithium ions can clearly be seen.

Despite their success, however, insertion materials suffer from comparatively low gravimetric energy density because of the large relative mass of the host material. LiC_6 for example has an energy density of 372 mAhg^{-1} versus $3,600 \text{ mAhg}^{-1}$ for

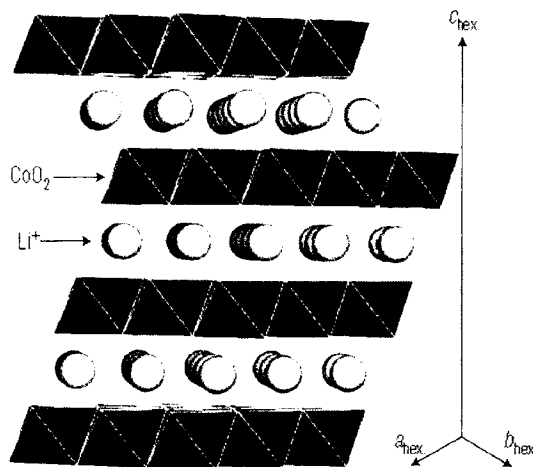


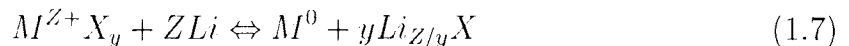
Figure 1.2: Structure of LiCoO_2 . Figure from Shao-horn et al.[71]

metallic lithium.[5] Furthermore, many insertion materials react as follows:



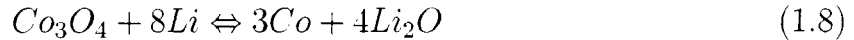
where M is a metal and X is an anion to which M is bound. Since the HOST is a constant in the reaction, a lithium atom can at best share the anion X with the host metal M inhibiting full reduction.

In the case of the other class of materials, known as *conversion materials*, the host undergoes a complete change of phase in order to accommodate the carriers. Conversion reactions involving transition metals follow the general reaction:



where Z is the oxidation state of the metal. In this case, upon lithiation, the metal atoms form neutral metallic nanoparticles which frees the cations to bond with more lithium. An example of this is the material Co_3O_4 , which, upon lithiation converts

to metal cobalt and lithium oxide per equation 1.8 below.



Theoretical capacities are typically three times as high as those of insertion materials attracting great interest and warranting further research. Unfortunately, these systems have some problems including poor capacity retention upon cycling, irreversible capacity loss on the first cycle (known as coulombic efficiency) and large polarizations (the difference in voltage between charge and discharge implying irreversible energy loss upon the change of phase).[43]

The same phenomenon can occur with alkaline earth metals. The work of Oumellal, Rougier, and Nazri have demonstrated the following metal hydride reaction:



The unlithiated cathode consists of tetragonal MgH_2 , which, upon lithiation converts to hexagonal Mg and LiH.[58] Oumellal et al. demonstrated that their MgH_2 electrode has a reversible capacity of $1,125 \text{ mAhg}^{-1}$, over three times that of today's commercial anodes. Furthermore, the polarization was only 0.25 volts as compared with the next best of conversion materials of 0.4 V for CoP_2 . This followed the trend of reduced polarizations with reduced ionic-covalency of the $M - X$ bond.[58] Furthermore, The small size of the hydrogen atom suggests it would offer better kinetics for such phase changes than its larger cation counterparts. This result suggests there could be great value in further research of more metal hydrides as conversion materials.

Problems still persist, however, for the MgH_2 system in that capacity was only retained for 20 cycles. This is assumed to be largely due to the degradation of the material during each cycle. Large volume changes that accompany the phase transitions lead to cracking in the material, degrading its electronic and ionic conductivity.[58]

While these problems seem to make conversion reactions untenable, potential cures to these mal effects may lie in nano structuring. For example, conversion materials can be mixed with scaffolding material that is inert to lithium. The scaffolding, such as nano porous carbons or SnO glasses confines the reactants to nano sizes that limit the macroscopic cracking and degradation and also provide electronic conducting pathways. Si-C nanocomposites have shown capacities of up to 1000 mAhg^{-1} for over 100 cycles.[5] With these promising solutions in mind, conversion materials remain worthy of study. In Section 3, we evaluate the thermodynamic viability of metal hydrides as conversion materials.

1.2 FUEL CELLS AND HYDROGEN STORAGE

A fuel cell, on the other hand, is an open system in which the active masses come from the outside as fuel during charging and exits the cell during energy extraction.[82] For low temperature fuel cells, the carrier is typically hydrogen gas from which significant energy can be extracted as hydrogen reacts exothermically with oxygen to form water releasing 235.76 kJ/mol of heat. One obstacle to practical fuel cell use is the difficulty of storing the hydrogen fuel in a manner in which it can be readily extracted when needed. In high temperature fuel cells, hydrogen can be reformed from more complex hydrocarbon fuels.[82] This can be an excellent utilization of hydrocarbons like natural gas, but limits flexibility in the energy source in the sense that it excludes the use of renewable energy sources, or even the conversion of power from the existing electric grid to energy in the fuel cell.

Preferred are hydrogen storage systems that can be loaded directly with hydrogen and released at a later time into the fuel cell. For a practical amount of energy for vehicular purposes, the hydrogen must be strongly compacted well beyond its gaseous density at standard temperature and pressure. One solution has been to compress the gas with high pressure tanks. However, using conventional high pressure

tanks with enough energy to give vehicles comparable driving range to their gasoline fueled counterparts would require an impractical sixty-gallons of storage using tanks rated at 300 bar. Reducing the tank size results in vehicle ranges uncompetitive with gasoline. A second solution is to liquefy the hydrogen by keeping the tank below its condensation temperature of -241°C , but this requires heavy and complex accompanying cooling systems.[72]

At the forefront of current research is the reversible storage of hydrogen within host solids. During storage (or absorption), H_2 is first disassociated at the surface into individual hydrogen atoms and then dissolved into the solid. In the case of interstitial hydrides such as $\text{PdH}_{0.6}$; hydrogen atoms initially flow through the host much like a gas. As hydrogen pressure is increased, and along with it the density of hydrogen atoms in the solid, the local interactions between hydrogen atoms increase. Here begins a two phase state in which particles of fully formed hydride begin to appear. For hydrides in which the hydrogen is ionically bound to the host, such as MgH_2 , the gaseous phase does not occur and the two phase region begins immediately. In the two phase region, one sees a pressure plateau in the isotherm in which hydrogen can be absorbed with very small changes in pressure until the hydride is fully formed. When the fuel is needed, desorption is induced by heating the system to a temperature at which the kinetic energy of the hydrogen atoms exceeds the small potential wells in which they sit. They return to free motion, ultimately exiting through the surface of the material and recombining to form H_2 gas which can then be directed towards the fuel cell. A classic example of this is a storage device made of magnesium which is charged under hydrogen pressure to form MgH_2 under the following reaction.



and releases hydrogen during discharge



MgH_2 stores a plentiful 7.6% hydrogen by weight, but has very slow charging kinetics from bulk Mg and is so stable that a temperature of 300°C is required to reverse the reaction and retrieve the fuel. To date, no affordable material has been discovered that escapes these issues while still offering energy densities competitive with gasoline. As such, current efforts are underway to improve the kinetics and stabilities of such systems. In the case of sodium alanate (NaAlH_4), it was demonstrated that the desorption temperature can be successfully lowered by doping with the catalyst TiO_2 . [72] Further work by Majzoub and Gross showed that many other halides of titanium also successfully improve the desorption rates suggesting that the titanium itself is the critical actor. [41] The arrhenius plot of Figure 1.3, taken from their study, demonstrates the improved kinetics when using the Ti-halides catalysts.

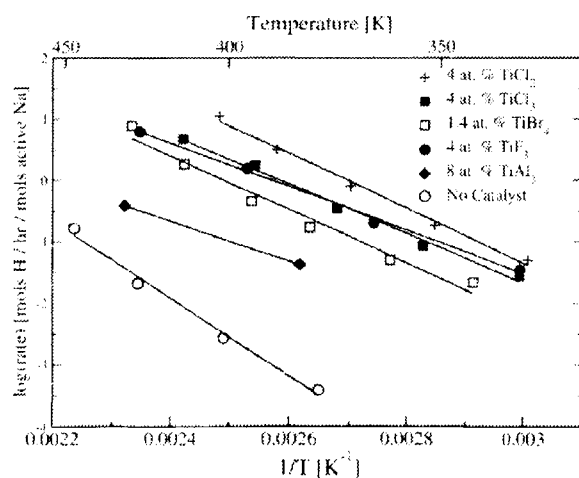


Figure 1.3: Arrhenius plots showing the kinetics in terms of rates of hydrogen desorption of NaAlH_4 when doped with titanium-halide catalysts. Figure is from the work of Majzoub et al. [41]

The second important approach has been to move from the bulk regime of the material to the micro, or nano regime via a constraining material such as nanoporous carbons. A nanoparticle of a hydride has a greater fraction of hydrogen atoms on the surface. The surface hydrogen atoms are bonded to fewer host atoms and thus have a weaker attachment than the internal hydrogen. It is hoped that this leads to lower desorption temperatures. In the case of MgH_2 , Even simple ball milling down to 10-50 nm grain sizes can drastically improve kinetics. At these large grain sizes, this is thought to be a result of increased surface area, decreased diffusion lengths and disruption of the outer oxide layer which can block desorption.[84]

Size can also affect thermodynamics. A density functional theory study (see Section 2) conducted by Wagemans et al.[79] demonstrates the change in enthalpy (a concept described in Section 2.4) of MgH_2 hydrogen desorption reactions as one varies the cluster sizes of the reactant MgH_2 clusters and product Mg clusters. Their calculations show that the cluster energies per formula unit decrease, as expected, for both compounds as the particle sizes are increased and eventually level off to bulk energies at higher cluster sizes. The resulting desorption enthalpies are generally reduced at smaller cluster sizes because the product metal Mg clusters are more drastically affected by size than the ionic MgH_2 because a larger volume allows the electrons of the metal to delocalize and lower its energy. This suggests the advantage of nanoconfinement for hydrogen storage applications, since, As explained in Section 2.4, a decreased enthalpy implies the desired lower desorption temperature.

1.3 MOTIVATION AND DISSERTATION OUTLINE

When putting forth the considerable effort required to do physics research, it is nice to have a useful application in mind. Ours is the further development of energy storage materials. This is a worthy application in and of itself simply for any gains that might be made in the extension of battery capacity for the existing

everyday portable devices that increasingly enrich our lives. The larger motivator however, is to push the limits of energy storage into a realm of performance suitable for the common automobile. Automobiles are the primary consumers of gasoline in the United States to the tune of 46 percent of all petroleum consumed according to the U.S. Energy Information Administration's 2011 report on U.S. refinery yields.[77] Meanwhile, only an estimated 826,000 automobiles in use in 2009 in the United States ran on a fuel other than gasoline.[2] Such reliance on any single product for so critical a need as transportation is a global economic vulnerability that could be ameliorated by the development of alternatives. While there are currently several other manners in which we harvest energy, burning coal for example, gasoline for the moment has the unique advantage of stable and safe transportability and immediate convertibility into useful work using the internal combustion engine. It is also currently relatively inexpensive and plentiful. However, should we at some future time find gasoline to be in short supply, the value of replacement options would very quickly and dramatically increase. To significantly increase economic robustness therefore, efficient and practical methods of storing generically produced energy are needed to extend all of our energy harvesting resources to use on the open road.

In this dissertation, a common first-principles frame work, density functional theory (DFT) is applied to two projects in the field of energy storage materials. In Section 2, A background of density functional theory and the projector augmented wave method is presented, followed by a description of the PEGS method (Prototype Electrostatic Ground States) which we employ to find low energy nanocluster geometries for the study in Section 4. Following that, in Section 3, is a DFT study on novel new materials for lithium ion batteries in which a Gibbs free energy is constructed as a function of DFT energies and lithium electrochemical potential. From this, reaction pathways are predicted for a metal hydride negative electrode composed of materials in the Li-Mg-B-N-H system. Twelve mixtures are uncovered with high theoretical

lithium capacities with relatively small expansions in volume, which it is argued, is a prerequisite for good cyclability. Finally, in Section 4, we relate another DFT study that attempts to gain understanding of the underlying chemical mechanisms of some recent results from experiments on the hydrogen storage properties of lithium borohydride confined to nanosizes via infiltration in highly ordered nanoporous hard carbon scaffolding.[35] In particular, we try to explain why LiBH_4 wets the carbon, while MgH_2 does not; why desorption temperatures appear to be lower than in bulk LiBH_4 ; and why diborane gas seems to disappear from the reaction pathways for small pore sizes. We find that many of the experimentally observed phenomena can be explained with a model of a single sheet of graphene, whose surface is permanently altered by the binding of boron to carbon defects.

2 COMPUTATIONAL METHODS

2.1 INTRODUCTION

A remarkable advancement of the last 20 years of computational physics has been the ability to accurately compute properties of condensed matter using only the geometric configuration of the atoms as an input. Specifically, the total energy of the configuration can be calculated from quantum mechanical first principles and from this most fundamental property any of the dependent properties. The bond length of a hydrogen molecule, for example, can be accurately predicted by calculating the total energy at various separation lengths between two hydrogen atoms. The bond length is then the separation distance at which the total energy is minimum. A similar exercise with bulk material can yield lattice parameters by varying a lattice vector of a unit cell. Vibrational modes, and all of the thermal properties that can be derived from them, can be found by calculating the energies of small displacements from equilibrium and the bulk modulus can be arrived at by noting changes in the total energy as one varies the volume of a unit cell of material.[62] Calculating the total energy requires solving the many body electron wave function problem, which demands so much computation, that theoretical application was quite limited in the past. As the accuracy and efficiency of these methods has improved, however, and as the power of computing systems has continued to multiply, the practicality of their use has gone beyond simply being theoretically interesting and is now an important player in increasing the understanding of material phenomenon and thus in the engineering of new materials. Since the 1970s one of the more dominant first principles theories in solid state research has been Density Functional Theory (DFT). This framework is the basis for much of the work in this dissertation and therefore warrants detailed discussion.

2.2 DENSITY FUNCTIONAL THEORY

2.2.1.DFT Beginnings. The key feature of DFT's increased computational power as compared to all electron methods such as Hartree-Fock, arises from the proof by Hohenberg and Kohn in 1964[24] that the total ground state energy and indeed all properties of any electronic system are a unique functional of the ground state electron density defined as

$$n(r) = 2 \sum_i |\psi_i(r)|^2. \quad (2.1)$$

This insight implies that in order to extract any system property of the ground state, one need not solve explicitly for the many body quantum mechanical wave function itself, as is done for Hartree-Fock methods, and which quickly becomes intractable for systems of even just a few atoms. One can instead minimize the energy as a functional of a single manageable three dimensional variable to obtain the ground state density.[62] This reduction in complexity greatly expands the universe of possible systems which can be computationally explored to reasonable accuracy and within a practical amount of time. Shortly after, in 1965, Kohn and Sham introduced a formulation[29] to exploit the Hohenberg and Kohn theorem including a functional of the density which is the basis for much of current day DFT work.[44] The Kohn-Sham functional, as it is now known, for the total energy can be written as

$$\begin{aligned} E[\{\psi_i\}] = & 2 \sum_i \int \left(-\frac{\hbar^2}{2m}\right) \nabla^2 \psi_i d^3r + \int V_{ion}(r)n(r)d^3r \\ & + \frac{e^2}{2} \int \frac{n(r)n(r')}{|r-r'|} d^3r d^3r' + E_{xc}[n(r)] + E_{ion}(\{R_i\}) \end{aligned} \quad (2.2)$$

where E_{ion} is the coulombic interaction energy of the ions, V_{ion} is the electrostatic potential from the ions, $n(r)$ is the electron density and $E_{xc}[n(r)]$ is the exchange-correlation functional, which describes the more complex interactions between the electron wave functions.[62]

One notices immediately that despite the assertion that the electron density is all that is needed, the individual electron wave functions ψ_i appear not to have been removed from the energy functional. Although in principle, Hohenberg and Kohn's theorem asserts that the total kinetic energies should be directly extractable from the density, there is no known way of doing so in an explicit manner. One must instead calculate them in the normal fashion from a set of single body wave functions. Using the real wave functions would defeat the purpose of the exercise as we would be again stuck with a many body electron problem. Kohn and Sham instead replaced the interacting electron system with a set of non-interacting electrons with the assumption that it is possible to modify the external potential V_{ext} such that the ground state density is identical to that of the real interacting system.[44] The idea is to move the effects of the electron-electron interaction to the external potential. The result is the following Hamiltonian for for each of the non-interacting electrons.

$$H = \frac{1}{2}\nabla^2 + V_{eff}(r) \quad (2.3)$$

where $V_{eff}(r)$ contains the effects of both the ions and the electron-electron interactions. To solve for the ground state, the wave function for this Hamiltonian is solved for as many lowest eigenvalues ϵ_i as there are electrons divided by two (assuming a spin symmetric system). V_{eff} consists of terms two, three and four from equation 2.2, and can be written entirely in terms of the electron density, which can in turn be calculated from equation 2.1. The second term, $\int V_{ion}(r)n(r)d^3r$ represents the electron-ion interaction, the third term is the electron-electron coulomb energy,

or Hartree term, and the fourth term $E_{xc}[n(r)]$, known as the exchange-correlation term, represents all of the remaining many body electron effects including the difference of the kinetic energies and the interaction energies between the interacting and the non-interacting system.[44] Separating out the long range Hartree term allows the remaining many body effects embedded in the exchange correlation term to be handled as a local functional of the density.[44]

2.2.2.Exchange-Correlation Functional. The exchange-correlation term $E_{xc}[n(r)]$ is now the only term in the Kohn Sham energy functional that does not have a unique definition. For all but ideal cases, an exact definition is not known and the accuracy of the calculation is directly related to how well this term is approximated. The proposal in the original Kohn-Sham paper currently known as the local density approximation (LDA) is to take advantage of the known analytical results for the exchange-correlation energy of the homogeneous electron gas approximation in which the positively charged nuclei are replaced by a uniform background sheet of positive charge.[44] The effect is taken to be local and evaluated with the following integral.

$$\int \epsilon_{xc}(n)n(r)ndr \quad (2.4)$$

$\epsilon_{xc}(n)$ is defined as the exchange-correlation energy per electron for a large homogeneous electron gas with density $n(r)$. [29]

$\epsilon_{xc}(n)$ can be further broken down into a functional for the exchange energy $\epsilon_x(n)$ plus a functional for correlation $\epsilon_c(n)$. The exchange functional represents the fact that any system of identical fermions must be antisymmetric under particle exchange. This is the quantum mechanical manifestation of the Pauli exclusion principle that result in electrons of like spin being spatially separated. Separating the electrons has the effect of reducing the Coulomb energy. When working with real wave functions, the approximation that includes this effect is known as Hartree-Fock.

The correlation functional $\epsilon_c(n)$ takes into account all of the other effects of electron correlation including both the difference between the interacting and non-interacting kinetic energies and the fact that the coulomb energies can be further reduced by spatially separating electrons of opposite spin which is not addressed by the exchange term.[62] The exact exchange functional for a homogeneous electron gas of any density is known analytically and the correlation functional is arrived at via interpolation from analytically known low density and high density limits.[44] Due to its roots in the homogeneous electron gas model, LDA is accurate to the extent that the density is slowly varying. The functional used for this research is a modification of the LDA known as the generalized gradient approximation (GGA). This functional remains local but also involves a term proportional to the gradient of the density thus increasing accuracy by accounting for linear variations in the density.[62] This is especially important for the ionic compounds examined in this thesis because the large degree of charge localization causes the charge density to vary sharply in space as compared to metallic or covalently bonded systems whose electrons are more delocalized.

2.2.3.DFT in a Periodic Lattice. Since most solids contain a very large number of electrons which would be impossible to treat individually, special techniques are employed to reduce a system of an essentially infinite number of electrons in a periodic potential of nuclei to a finite and manageable number. The trick is to take advantage of the crystal periodicity to reduce the number of degrees of freedom in the system. The foundation of the new framework is Bloch's theorem which states that eigenstates $\psi_k(x)$ in a periodic potential can be written as the product of a plane wave with wave number k and a function $U_k(r)$ that is periodic with the lattice such that

$$U_k(r + T_n) = U_k(r) \quad (2.5)$$

where T_n is a translation operator of the lattice. The wave function can thus be written with basis functions in k as shown below.[44]

$$\psi_k(r) = e^{ik \cdot r} U_k(r) \quad (2.6)$$

The cell periodic part can itself be expanded into spatial Fourier components with crystal reciprocal lattice vectors G as wave vectors.

$$U_k(r) = \sum_G U_G e^{iG \cdot r} \quad (2.7)$$

Thus, the full wave function for any k can be written as

$$\psi_{i,k}(r) = \sum_G c_{i,k+G} e^{i(k+G) \cdot r} \quad (2.8)$$

where $c_{i,k+G}$ are the expansion coefficients of the wave functions in the basis of the plane wave expansion and the expansion of the periodic potential.[44] For a complete calculation, the Schroedinger equation must be solved for each wave number ($k + G$). As the G represents discrete Fourier components of the periodic potential, it is possible to calculate with a finite set of basis functions up to some cutoff. Higher G values represent electronic plane waves with higher kinetic energy. Since most of the contributions to the total energy tend to come from the lower kinetic energies, a cutoff can be chosen that encompasses an arbitrarily large percentage of the total energy. The cutoff energy, defined as the plane wave energy above which no G numbers are calculated, is thus used as a convergence parameter when doing DFT calculations.

2.2.4.Pseudopotentials. If one attempts to expand in plane waves the core electrons in an atom, one quickly finds that a very large energy cutoff (see Section 2.2.3) is needed for adequate convergence. This is due to the heavy oscillations that occur in the wave functions of the core electrons that are tightly bound around a

nucleus. This can also be understood in terms of the Heisenberg uncertainty principle $\Delta x \Delta p = \hbar$. A heavily localized core electron has a small Δx which implies a large Δp . A large momentum in turn implies a large kinetic energy. A large energy cutoff is therefore necessary to capture the high energy components of the localized core electrons. The valence electrons also oscillate heavily near the nucleus due to the Pauli-exclusion requirement to be orthogonal with the core electrons. The pseudopotential approximation elegantly addresses this problem by taking advantage of the fact that the core electrons generally change very little from system to system.[62] The approach is to take advantage of the fact that most all chemical effects are a result of the response of the loose valence electrons. The core electrons generally change very little from system to system and so may be treated as approximately constant. Furthermore, the core electrons act to screen the valence electrons from the full force of the ions positive Coulomb charge. The solution is to combine the core electrons and the hard external potential of the nuclei into a single pseudopotential that represents both. This results in fewer electrons for which we must solve the Kohn Sham equations, and also gives us a softer external potential. Since the requirement to be orthogonal with the real core electrons has been removed, the valence electron wave function are replaced by pseudo wave function which are much smoother near the nucleus, but identical to the real wave functions in inter-ionic space. Figure 2.1, taken from Payne et al. graphically compares the pseudo and all-electron wave functions and potentials. The smoothing of the wave function near the nucleus greatly reduces the number of plane waves required in the expansion and thus lowers the computational demand.[62]

One common variant of this approach is the norm-conserving pseudopotential which is designed to produce nodeless wave functions up to a chosen core radius as described above, but with the additional constraint that the total charge, or norm,

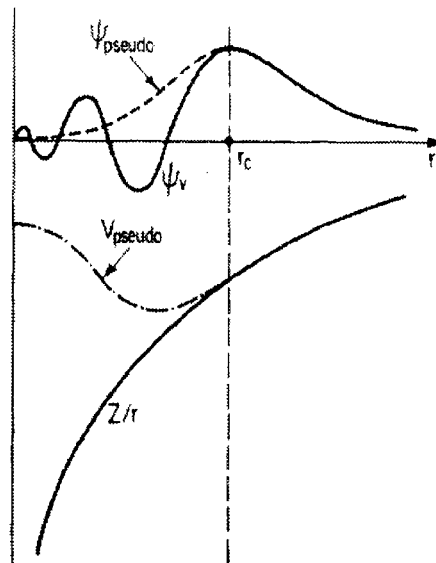


Figure 2.1: A figure from a paper by Payne et al. illustrating the pseudo wave function. Inside r_c , the wave function is replaced by a smooth nodeless pseudo wave function while beyond r_c it remains identical to the all-electron wave function.[62]

of the exact wave function must be preserved. Norm-conservation is critical for pseudopotentials to correctly reproduce approximately the same bonding descriptions as well as scattering powers that are seen with all electron methods.[22] These pseudopotentials have some drawbacks. Transferability, the extent to which the model remains consistent in different chemical environments, is best when the core radius exactly covers the extent of the core electrons but does not extend beyond this. For the case of elements with valence d electrons, which are highly localized near the core radius, high energy cutoffs are needed for convergence, making the calculations expensive. This can be remedied by pushing the core radius farther out into the inter-ionic region where there is a smoother charge density, but there is a price to be paid in the form of poor transferability. Vanderbilt proposed what are now known as ultrasoft pseudopotentials to tackle this problem in 1990. This approach removes the requirement of norm-conservation in order to obtain pseudopotentials with optimal core radii that require lower energy cutoffs. All-electron scattering behavior is

regained by adding an augmentation charge around the atom center (away from the cutoff radius) which has a total charge equal to the charge deficit that results from not enforcing norm-conservation.[34]

2.2.5. Projector Augmented Wave Method. Another approach related to the pseudopotential method is the projector augmented wave (PAW). This is the method chosen for this work. As in the pseudopotential method, the goal is to resolve the problem of the large oscillations of the wave functions near the nucleus due to orthogonality with the core states. Also like the pseudopotential method, we wish to transform the real wave functions into smoother pseudo wave functions. Instead of doing this by inventing a fictitious potential that then generates smoother wave functions however, this is done by finding a linear transformation T between a Hilbert space of all electron wave functions ψ that oscillate near the core and a Hilbert space of smooth pseudo wave functions $\tilde{\psi}$ that are better suited for computation.

The PAW method separates space into two regions. One region known as the augmentation region near the center of the atoms where the all electron wave function is highly oscillatory and more readily represented by a spherical harmonic basis, and the smoother interstitial bonding region which is easier to describe with plane waves. In the bonding regions, the all electron wave functions are identical to the pseudo wave functions. The transformation T thus applies only to the augmentation regions and is applied atom by atom as below.

$$T = 1 + \sum_R \tilde{T}_R \quad (2.9)$$

where \tilde{T}_R is the local transformation for each atomic site's augmentation region R . The pseudo wave function $\tilde{\psi}$ and the all electron wave function ψ are both decomposed

into a complete basis of partial waves θ and $\tilde{\theta}$ per Equations 2.10 and 2.11

$$|\tilde{\psi}\rangle = \sum_i |\tilde{\theta}_i\rangle c_i \quad (2.10)$$

$$|\psi\rangle = \sum_i |\theta_i\rangle c_i \quad (2.11)$$

so that the transformation can be defined as a mapping between each partial wave and and its pseudo partial wave counter part as $|\theta_i\rangle = (1 + \tilde{T}_R)|\tilde{\theta}_i\rangle$. Since this is a linear transformation, the coefficients c_i are the same for the all electron wave function ψ and the pseudo wave function $\tilde{\psi}$. The all electron wave function can thus be expressed as

$$|\psi\rangle = |\tilde{\psi}\rangle - \sum_i |\tilde{\theta}_i\rangle c_i + \sum_i |\theta_i\rangle c_i \quad (2.12)$$

the coefficients c_i can be expressed as the pseudo wave function's projection onto the dual of the pseudo partial wave as $c_i = \langle \tilde{p}_i | \tilde{\psi} \rangle$ where this dual \tilde{p}_i is known as the projector. From equations 2.9 and 2.12, the transformation T can be written

$$T = 1 + \sum_i (|\theta_i\rangle - |\tilde{\theta}_i\rangle) \langle \tilde{p}_i | \quad (2.13)$$

with the transformation consisting of the partial wave, the pseudo partial waves, and the projectors all of which still must be defined. As can be seen in the above equation, the projectors probe the pseudo wave functions to find how it is to be decomposed into pseudo partial waves and from this the all electron decomposition is recovered since the coefficients for basis sets are identical.[7]

The all electron wave functions $|\theta_i\rangle$ are found by solving the Schroedinger equation in spherical coordinates for the case of an isolated atom enforcing orthogonality with the core states. At least one such partial wave thus exists for each angular momentum state for each site R up to some truncation.[9] The result is a basis set

of valence partial waves all of which are orthogonal to the core states. For each all electron partial wave, the task is now to find a pseudo partial wave that is identical to the all electron wave in the bonding region but smooth in the augmentation region. This is accomplished by first calculating an all electron potential, and then finding a nodeless potential that matches the all electron potential outside the augmentation region. The pseudo partial waves are then obtained as solutions to the Schroedinger equation given the pseudopotential. The core states are decomposed in a similar fashion with an all electron highly nodal version and a transformed version with a smoothly varying electron density for the purpose of yielding a smooth effective potential for the pseudo wave functions. The projectors are then found by finding the dual of the pseudo wave function such that $\langle \tilde{p}_i | \tilde{\theta}_i \rangle = \delta_{ij}$. The core states themselves have no projector function since they are always assumed to be completely populated manifesting the frozen core approximation.[7]

The electronic ground state of the pseudo wave functions can now be found by iteratively solving the Kohn-Sham equations for a potential consisting of Hartree and exchange correlation terms using the pseudo-electronic density. Once this has been found, the all electron total energy can be obtained by using the projector functions to transform the pseudo wave functions into all electron wave functions and calculating the Kohn-Sham equation in terms of the all electron density. It is possible to look at the PAW method as simply an all electron method with a clever change of coordinates that match far from the core. Once the system is solved with the more convenient pseudo wave functions, one can look at the behavior near the boundary of the augmentation region to determine to which real wave functions the solution corresponds.[9] Using an all electron approach yields some advantages to the PAW method. A pseudopotential constructed from an atom will not necessarily work well once placed in a chemical environment, PAW results on the other hand come from the real density and potential and do not depend on the reference system. Convergence is

faster than in norm-conserving pseudo potentials and the calculation itself is simplified and should therefore be more efficient than ultra soft pseudopotential calculations.[9]

2.3 AN EXAMPLE OF A FIRST PRINCIPLES SUCCESS: UNDERSTANDING TRANSITION METAL HYDRIDES

Using first principles calculations, it is possible to decompose physical phenomena into components in such a way that would not be possible in the laboratory. As an example, Smithson et al.[74] completed a detailed first principles study in 2002 on the stability and electronic structure of transition metal hydrides. They endeavored to examine the processes by which a host metal absorbs hydrogen to become a metal hydride and determine the relative importance of each process as a means of understanding the varying hydride stabilities among the transition metals.

The energy of hydride absorption is broken down by the authors into three components.

- 1) E_{phase} : The energy of the phase change of the metal from its equilibrium structure (hexagonal for Mg) to the structure of the metal hydride (tetragonal casiterite for MgH_2)
- 2) $E_{expansion}$: The energy of expansion of the metal unit cell required to accommodate the hydrogen
- 3) $E_{insertion}$: The energy of inserting the hydrogen atom and the accompanying changes to the electronic structure

The hydrogen formation energy can thus be written as

$$E_{formation} = E_{phase} + E_{expansion} + E_{insertion} \quad (2.14)$$

By calculating the changes in energy at each step using density functional theory, the relative importance of these components was determined. Their findings reveal that the structural effect (E_{phase}) is mostly negligible. The lattice stretching ($E_{expansion}$) contributes a large positive energy to the formation enthalpy and the hydrogen insertion ($E_{insertion}$) can be either a positive or negative contribution to the energy as the hydrogen atom introduces new electron states to which the metal electrons may transfer. Illustrating the trends in $E_{insertion}$, a set of electron density plots from their work is copied below in Figure 2.2. Here, the charge density of the hydride has been subtracted from the that of the metal expanded to the same lattice parameters. This picture reveals the migration of electrons from the metal to the hydride, and in some cases from the hydrogen to the metal.

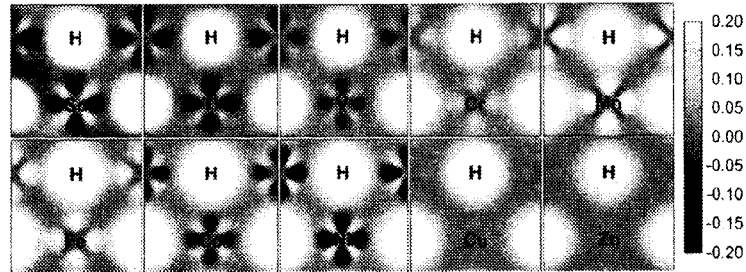


Figure 2.2: Electron density change as a result of step 3. Light (dark) areas indicate an increase (decrease) in charge density after inserting the hydrogen atom into the expanded metal. Figure from Smithson et al.[74]

Having eliminated E_{phase} as an important component, the stability of the metal hydrides as one moves across the periodic table can be explained as a competition between the effects of $E_{expansion}$ and $E_{insertion}$. A graph from their paper is presented in Figure 2.3 showing the relevant trends in the 3d transition metals.

The early transition metals are known experimentally to form stable hydrides. These metals have low cohesive energies due to the smaller number of d electrons

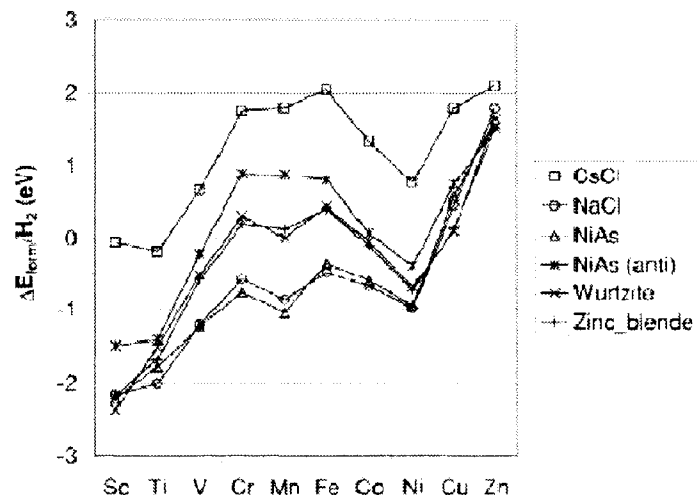


Figure 2.3: Metal hydride formation energies of the 3d transition metals in various crystal structures. Figure from Smithson et al.[74]

participating in the metallic bonding. A low cohesive energy indicates that the metal atoms are easier to separate, which in turn means a smaller contribution from the positive $E_{expansion}$ term as compared to strongly cohesive metals found later in the series where there are more d electrons. At the same time, the formation energy can be either lowered or increased significantly through the bonding of the metal d electrons with the hydrogen atoms. As one progresses through the 3d series, more d electrons participate in metallic cohesion making $E_{expansion}$ more important. $E_{insertion}$ meanwhile, varies as one progresses to the right of the series depending on whether or not the inserted hydrogen atom introduces electron states that are above or below the Fermi level causing this term to be positive or negative. Figure 2.2 shows a lack of a clear trend for this term. Large electron transfers to the hydrogen atom occur for the early series metals Sc, Ti, and V, lowering the energy. This is followed by electron transfer in the opposite direction, from the hydrogen atom to the metals, in Cr, Mn, and Fe resulting in a positive $E_{insertion}$. A negative insertion energy returns for Co, and Ni and almost no charge transfer at all can be seen for the apparently inert Cu, and Zn. The generally unfavorable charge transfer situations coupled with the higher

cohesive energies help to explain why the later 3d metals do not form stable hydrides. By using computational methods to tease our multiple effects that are difficult to separate in experiment, this study highlighted the importance of the stretching term which had previously been largely neglected as compared to the insertion term in the engineering of new metal hydrides.

2.4 REACTION ENTHALPIES OF METAL HYDRIDES: PHASE DIAGRAMS FROM FIRST PRINCIPLES

A particularly useful quantity in the study of hydrogen storage chemistries of metal hydrides (discussed in Section 1) that can be arrived at from first principles is the change in enthalpy ΔH of hydride desorption. Section 1.2 makes much mention of attempts to shift ΔH to thermodynamically favorable regions for the case of MgH_2 . Thermodynamically favorable, in this case, means the right amount of hydride stability. If ΔH is too high, vehicles that operate at lower temperatures will be unable to provide the energy of vaporization necessary to trigger hydrogen desorption. In other words, it implies that the hydride is too stable. If ΔH is too low, then the hydride is not stable enough, and will generally be more difficult to rehydride. ΔH , together with the capacity, are the two parameters used by the Department of Energy to qualify a candidate reaction as promising in their 2006 annual progress report. A chemistry with capacity > 6.5% and $15 < \Delta H < 75$ kJ/mol H_2 is considered a candidate by DOE[25] (although a more realistic enthalpy range is $15 < \Delta H < 24$ kJ/mol H_2 corresponding to operating conditions of 0-100 bar and 0-100 °C).[72] Furthermore, from this single fundamental quantity, the equilibrium pressure-temperature relationship of a metal hydride reaction can be approximately determined.

We now show how ΔH can be readily calculated from first principles, and how from ΔH , the phase diagram can be obtained. We start with the definition of the

enthalpy

$$H = U + pV \quad (2.15)$$

where U is the system's total internal energy, p is the pressure, and V is the volume. U can be decomposed into the static bonding energies whose calculations are described in Section 2, and the energies of the vibrational modes at finite temperatures, which can be calculated per Section 2.5.[25] As one does not know *a priori* what the reaction temperature is, zero point energies can suffice as an approximation. In fact, this will be consistent with our final equation which assumes that ΔH does not change with temperature. In a hydrogen desorption reaction, the pV term represents the displacement energy necessary to make room for the released hydrogen gas. The change in volume of the hydride itself is small compared to the released gas and can be neglected. We can therefore write the change in enthalpy as

$$\Delta H = \mu_{H_2} + \sum_{products} (E_{static} + E_{vib}) - \sum_{reactants} (E_{static} + E_{vib}). \quad (2.16)$$

All terms are normalized to a quantity representing the release of a single molecule of H_2 . μ_{H_2} is the chemical potential of the released hydrogen gas which encompasses both its static and vibrational DFT energy plus its contribution to the pV term (see Section 3.7 for a treatment of this term). As the change in volume is nearly common among hydrides and is difficult to calculate, this term is also often neglected for enthalpy estimates. Table 2.1 shows calculated desorption enthalpies for selected metal hydride reactions. In these calculations, the static energies seem to much more closely approach the experimental values than when zero point energies are included.

Having obtained ΔH , we attempt to infer from it the pressure-temperature line for equilibrium. We make use of a relationship between a reaction's Gibbs free energy

Table 2.1: Enthalpies of reaction calculated using equation 2.16 (μ_{H_2} neglected) with and without the zero point energy included. Reported experimentally determined values are included for comparison.

Hydride Desorption Reaction	ΔH Static (kJ/mol H_2)	ΔH with Z.P. (kJ/mol H_2)	ΔH exp. (kJ/mol H_2)
$LiBH_4 \rightarrow LiH+B+\frac{3}{2}H_2$	70.8	48.8	74[47]
$LiBH_4 \rightarrow Li+B+2H_2$	95.7	78.0	–
$LiH \rightarrow Li+\frac{1}{2}H_2$	170.3	165.9	182[21]
$NaAlH_4 \rightarrow \frac{1}{3}Na_3AlH_6+\frac{2}{3}Al+\frac{3}{2}H_2$	30.7	20.24	37[10]
$Na_3AlH_6 \rightarrow 3NaH+Al+\frac{3}{2}H_2$	49.4	33.3	47[10]
$NaAlH_4 \rightarrow NaH+Al+\frac{3}{2}H_2$	37.0	24.6	–
$NaH \rightarrow Na+\frac{1}{2}H_2$	86.0	86.9	112 [1]
$MgH_2 \rightarrow Mg+H_2$	63.3	57.4	75 [67]

and its equilibrium constant (equation 2.17) as well a relationship that exists under the ideal gas approximation between the equilibrium constant K and the pressure (equation 2.18).

$$\Delta G = -RT \ln K \quad (2.17)$$

$$K = \frac{p_0}{p_{H_2}} \quad (2.18)$$

p_0 is a thermodynamic reference pressure and p_{H_2} is the partial pressure of the hydrogen gas. Substituting equation 2.18 into equation 2.17, and subsequently substituting this result into the definition of the change in Gibbs free energy (equation 2.19)

$$\Delta G = \Delta H + T\Delta S \quad (2.19)$$

yields what is known as the van't Hoff equation (equation 2.20)

$$\ln \left(\frac{p_{H_2}}{p_0} \right) = -\frac{\Delta H}{RT} + \frac{\Delta S}{R} \quad (2.20)$$

where R is the gas constant, and ΔS is the entropy change of the reaction.[4] With this equation we now have the equilibrium pressure-temperature relationship for the metal hydride. ΔS in the y-intercept term can be calculated from first principles vibrational modes using equation 2.31 if desired, but it is dominated by the formation of molecular hydrogen gas and is typically about $130 \text{ JK}^{-1}\text{mol}^{-1}$ for all metal hydride systems. The change in enthalpy therefore, remains the characteristic quantity of the hydride stability.[72]

Ackbarzadeh et al. demonstrate nicely how a refined ΔH , as well as a full phase diagram, can be calculated from first-principles in their work predicting hydrogen storage reactions in the Li-Mg-N-H system.[3] In their method, DFT energies are calculated for a complete phase space as well as a chemical potential term for the hydrogen gas as a function of temperature and pressure. The phase diagram is calculated by minimizing the Gibbs free energy at every point in phase space and equilibrium phase boundaries are defined to occur wherever multiple mixtures equally minimize the free energy such that $\Delta G = 0$ for the reaction. Equation 2.19 can then be reduced to equation 2.21 below.

$$\Delta H = -T\Delta S \tag{2.21}$$

ΔH can be thus obtained by holding the pressure constant, increasing the temperature until a $\Delta G = 0$ condition is reached for two phases, and noting the temperature and ΔS between them. Figure 2.4 shows their predicted van't Hoff plots for seven reactions along with a region of feasibility represented by the dashed square. In this case, the plot shows clearly that since unfortunately none of the van't Hoff lines cross into the feasibility region, none of the studied materials can be practically applied for light vehicle applications although two reactions come close. Thanks to their theoretical work, however, we can identify which chemistries may have potential with

further treatment (perhaps with doping or other methods). For the less promising reactions, wasted efforts in further exploring these chemistries experimentally can be averted. We note here that the van't Hoff relation assumes that ΔH does not change

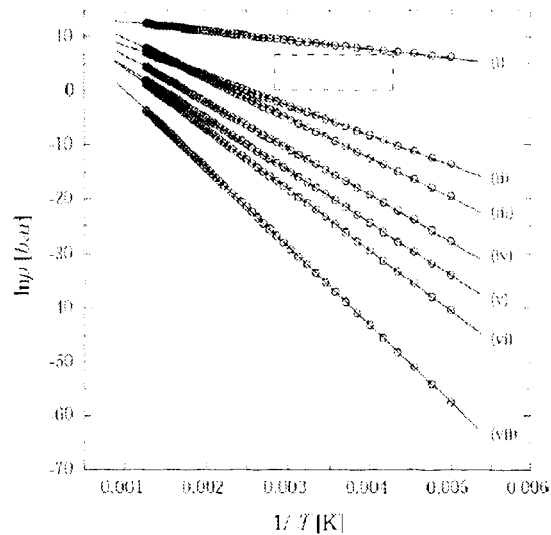


Figure 2.4: Van't Hoff plots for hydrogen storage reactions by Ackbarzadeh et al. The figure is taken from their paper.[3]

with temperature. This is not completely true as the vibrational terms for the energy of each phase will indeed decrease as temperature is increased. The example in Figure 2.4, however, whose data points were calculated individually from first principles using finite temperature and then fitted to the van't Hoff equation, shows that the linearity is maintained demonstrating the quality of the approximation. Moreover, The relation can be used in the reverse. The enthalpies and entropy of reaction for a metal hydride can be extracted from an experimentally determined phase diagram by fitting it to the van't Hoff equation.

2.5 PHONON CALCULATIONS

Several observables in materials are the direct results of ionic vibrations in the crystals including including Raman, infrared and neutron diffraction and a wide variety of thermodynamic properties. That these experimental properties can often be reproduced from calculating phonon mode frequencies in DFT calculations offers further strong validation to the theoretical framework.[6] In Section 3, we calculate phonon modes in order to calculate temperature dependent vibrational energies for each compound in the lithium-ion battery study.

Because the ions are many orders of magnitude more massive than the electrons, they move much faster and can be said to always instantly find their new ground state after any ionic displacement. This is known as the Born-Oppenheimer approximation and allows one to calculate ionic dynamics in DFT by calculating the ground state electron density at various points near equilibrium in ionic configuration space. To calculate phonons in the harmonic approximation, in which all lattice vibrations have energies quadratic in the atomic displacement, an equilibrium geometry must first be found by relaxing the system to a state in which the forces acting on each ion are zero. From this geometry, vibrational frequencies are calculated by finding eigenvalues of the Hessian of the energy normalized by the masses as:

$$\det \left| \frac{1}{\sqrt{M_i M_j}} \frac{\partial^2 E(R)}{\partial R_i \partial R_j} - \omega^2 \right| = 0 \quad (2.22)$$

leaving only the challenge of calculating the first and second derivatives.[6] This can be, and often is, accomplished by the finite difference method in which points on the energy surface are sampled as individual ions are displaced short distances from equilibrium and second derivatives are extracted from the resulting parabolas. Our calculations, however, use what is known as the linear response method.

In the linear response method, all first and second derivatives are calculated with only one ground state density calculation at equilibrium with the application of both Hellman-Feynman theory and first order perturbation theory. According to Hellman-Feynman theory, first derivatives of Hamiltonian eigenvalues with respect to any parameter can be calculated as the ground state expectation value of derivative of the Hamiltonian derivative as shown below.[6]

$$\frac{\partial E}{\partial \lambda} = \langle \psi_0 | \frac{\partial H}{\partial \lambda} | \psi_0 \rangle \quad (2.23)$$

Forces can then be written by using ion displacements as the parameter λ and evaluating the inner product:

$$F_{i,j} = \int n_0(r) \frac{\partial V(r)}{\partial R_{i,j}} dr \quad (2.24)$$

where $R_{i,j}$ is the displacement of atom i in the direction j and V is the self consistent interaction potential,

$$V(r) = V_{ion}(r) + e^2 \int \frac{n(r')}{|r - r'|} dr' + v_{xc}(r) \quad (2.25)$$

From these forces, Hessian matrix components can be obtained by trivially taking a second derivative[15]:

$$\frac{\partial^2 E}{\partial R_j \partial R_i} = \int \frac{\partial n(r)}{\partial R_j} \frac{\partial V_R(r)}{\partial R_i} dr + \int n(r) \frac{\partial^2 V_R(r)}{\partial R_i \partial R_j} dr \quad (2.26)$$

We are now left only with finding the linear response of the density $\frac{\partial n}{\partial R}$ which can be found with first order perturbation theory using the change in potential ΔV as the perturbation. In first order perturbation theory, corrections to the wave function are calculated as an expectation value of the change in potential in the ground state wave

function,

$$\Delta\psi_n(r) = \sum_{m \neq n} \psi_m(r) \frac{\langle \psi_m | \Delta V | \psi_n \rangle}{\epsilon_n - \epsilon_m} \quad (2.27)$$

Summing over all of the non-interacting electrons yields the linear response of the electron density to the perturbation in the potential.

$$\Delta n(r) = 4 \sum_{n=1}^{N/2} \sum_{m \neq n} \psi_n^*(r) \psi_m(r) \frac{\langle \psi_m | \Delta V | \psi_n \rangle}{\epsilon_n - \epsilon_m} \quad (2.28)$$

At the same time, V is a function of the density per equation 2.25, which can be linearized to obtain Δn as a function of ΔV ,

$$\Delta V(r) = \Delta V_{ion}(r) + e^2 \int \frac{\Delta n(r')}{|r - r'|} dr' + \left. \frac{dv_{xc}(n)}{dn} \right|_{n=n(r)} \quad (2.29)$$

Equations 2.29 and 2.28 can now be solved iteratively to find the linear response which can in turn be utilized to find the components of the Hessian matrix[6] and from them the vibrational frequencies. The frequencies in turn can be used to calculate temperature dependent enthalpy and entropy terms in the Gibbs free energy given below.[73]

$$H_{vib}(T) = \sum_i \frac{1}{2} \hbar \omega_i + \hbar \omega_i \left[\exp\left(\frac{\hbar \omega_i}{k_B T}\right) - 1 \right]^{-1} \quad (2.30)$$

$$S_{vib}(T) = k_b \sum_i \frac{\hbar \omega_i / k_B T}{\exp\left(\frac{\hbar \omega_i}{k_B T}\right) - 1} - \ln \left[1 - \exp\left(\frac{-\hbar \omega_i}{k_B T}\right) \right] \quad (2.31)$$

The sum is over all of the normalized phonon modes except for the three gamma point longitudinals which represent uniform translations of the entire lattice. Using this method as it is implemented in the VASP package,[32, 33, 30, 31] we are able to determine finite temperature properties at 300K for the lithium ion battery study to follow. Because of the magnitude of the computational resources required, this

method is untenable for the surface calculations in Section 4 where we are limited to the study of static effects in our study of borohydride wetting properties on carbon.

2.6 SURFACE CALCULATIONS WITH DFT

Because we use a framework of DFT based on periodic boundary conditions, simulating the surface of a material is a matter of some delicacy because of the existence of the slab's periodic images. To minimize the error due to the mutual interaction of periodic slabs, a large supercell is used in which the surface images are separated by a large vacuum layer. Supercells can be generated from fundamental unit cells using the POS_supercells.awk script shown in appendix 5. The dimensions of the supercell then become convergence parameters that can be increased until the energy of interaction between periodic images becomes as small as desired. Figure 2.5 shows a supercell example used in Section 4 for a sheet of graphene. In the case of

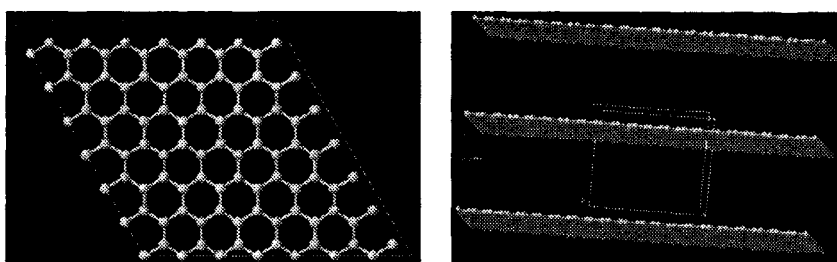


Figure 2.5: An example of a large supercell with a vacuum layer used to model a graphene surface.

a slab calculation, the aperiodicity is only in the direction perpendicular to the slab which is thus the only direction that needs to be extended in the supercell. This results in the cell being split into a slab and a vacuum region where the length of the vacuum is now an extra convergence parameter that must be adjusted to energy

convergence to ensure adequate isolation of the sheet. Figure 2.6 shows the result of a convergence plot determining the amount of vacuum necessary for calculations on a sheet of graphene. Judging from the graph, convergence seems to appear at about 7 Å. That exercise, however, only ensures separation of the carbon sheet itself.

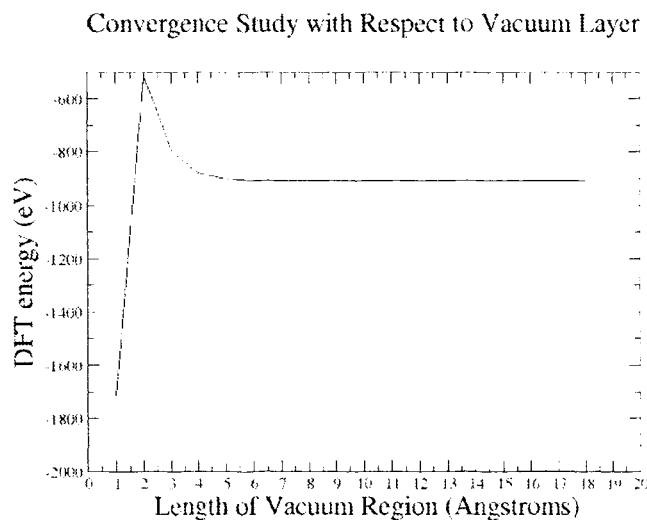


Figure 2.6: Convergence plot of DFT energy vs. the length of the vacuum layer.

Calculations involving adsorption as are performed in Section 4 require additional vacuum to make sure that the adsorbate is only interacting with the surface and not its periodic image. Further, adsorbate nanoclusters introduce periodicity in the directions parallel to the surface requiring that the supercell also be extended in those directions multiplying the number of carbon atoms and greatly increasing the computational cost.

Relaxing the supercell can also be tricky as one wishes the cell to find optimum size and shape in the planar directions but not for the direction perpendicular to the surface. This is because the real energetic minimum, as far as DFT is concerned, is one

in which the periodic slabs are brought into contact to form a layered system. As of the writing of this thesis, we are aware of no way in the VASP package to independently select lattice vectors as fixed during cell optimizations. A work around is to limit the interaction of the periodic surface images by making the vacuum region sufficiently large during the relaxation such that changes in the inter-slab distances will cause energy changes small enough such that they lie within the tolerances that define a completed relaxation. After a relaxed supercell has been attained, one can then increase or reduce the vacuum layer to a level appropriate for the tolerances required by the study. Although not used in this research, a simpler method is to simply keep the cell volume constant during the relaxation (Setting the ISIF switch to '4' in VASP) so as to inhibit cell size collapse. The needed expansions or contractions that occur in the planar directions are accommodated by trivial changes in the dimension of the vacuum layer.

Once a supercell environment has been generated, further tools are needed to manipulate the adsorbate clusters. In Section 4, the nanoclusters are first relaxed as a gas molecule in a large cubic vacuum unit cell to obtain a minimum energy configuration. In VASP, atomic configurations are stored in reduced coordinates, which use the lattice vectors as a basis. In order to translate the nanoparticle to the lattice environment, the script `POS_rehost.sh` (see appendix 5) converts the VASP POSCAR file to common Cartesian coordinates of the XYZ format using the AWK script `POS-toXYZ.awk` (see appendix 5) and from Cartesian coordinates to the coordinate system of the supercell. Once the adsorbate has been rehosted, one needs to translate and rotate it to the desired position on the substrate. This can be accomplished using the `shift_atoms.sh` script (appendix 5), which again transforms coordinates to Cartesian where the cluster is then translated to the origin. Here, it accomplishes the rotations and then the translations as specified by the user before transforming back to the crystal coordinate system of the supercell.

Once the cluster is in the desired initial configuration, the system is relaxed again to reflect the surface interactions. Depending on the nature of the calculation, it may be desired to ignore changes in the surface itself. In this case, the VASP selective dynamics feature can be utilized to keep the atoms of the surface fixed to greatly simplify the relaxation. For slab calculations, it is important to perform an initial relaxation with the minimum energy cutoff recommended in the pseudopotential files in order to achieve reasonable computational times. From the new relaxed positions, final production level energies can be more easily obtained by performing a second relaxation at the desired cutoff.

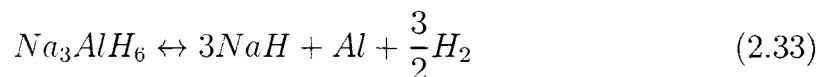
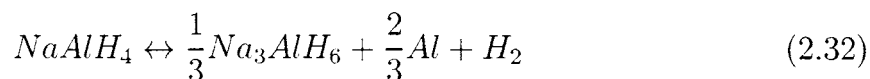
2.7 PROTOTYPE ELECTROSTATIC GROUND STATES (PEGS)

Density Functional Theory (DFT) as described in Section 2 can be a useful tool for investigating and understanding the materials in hydrogen storage and lithium ion battery reactions. A common impediment to DFT investigations however is the unavailability of a crystal structure for the target compound. As these compounds are often difficult to synthesize for proper X-ray diffraction studies, structural determination from first principles is often the only option. Even when structures are available, they are sometimes too complex to calculate DFT properties in a reasonable time. In our lithium ion battery work for example, $\text{Mg}(\text{BH}_4)_2$ contains 330 atoms per unit cell with 165 symmetry inequivalent degrees of freedom making the calculation of phonon modes extraordinarily time consuming. In this case, feasibility can be recovered by finding simpler structures with similar energetics.

One common approach to crystal structure determination is the *database searching method* in which several crystal structures that appear frequently among other compounds are attempted for the target material. After relaxing all candidates of a particular chemistry in DFT, the lowest energy result, if reasonable, is assumed

to be the ground state. An obvious drawback of this method is the inability to search for new structures or even structures that appear only rarely in the literature. Finally, systematic searches of the configuration space using Monte Carlo techniques with DFT energies as a heuristic have been attempted but have limited practicality due to the computational expense of the DFT calculations.[59]

2.7.1. Complex Ionic Compounds and Hydrogen Storage. Intermetallic hydrides such as LaNi_5 , and TiFe were the focus of early hydrogen storage work because of their excellent kinetics and practical operating conditions characterized by a favorable desorption enthalpy of 30.6 kJ/mol H_2 for the case of LaNi_5 . Their hydrogen capacity, however, has remained stubbornly below 2% by weight in spite of several attempts to improve it.[75, 68] The field was refocused in 1997 when Bogdanovic and Schwickardi demonstrated that hydrogen cycling of the complex ionic compound NaAlH_4 can be made reversible by doping with a small amount of titanium catalyst via the following reactions



yielding capacities of approximately 5 weight percent.[11] This discovery has attracted researchers to examine other compounds of this class composed of a metal cation and a complex hydrogen based anion such as $[\text{AlH}_4]^-$, $[\text{AlH}_6]^{-3}$, $[\text{BH}_4]^-$, and $[\text{NH}_2]^-$ among others for their hydrogen storage potential. These compounds all have the similar feature of a metal or metalloid atom bonded to hydrogen ligands as is represented for sodium alanate in Figure 2.7.

The many different stoichiometries that can be imagined for this class leads to a vast set of possible compounds to be explored requiring considerable experimental resources as well as significant effort in developing new synthesis techniques for

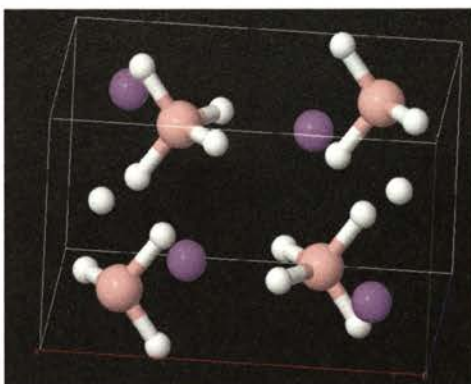


Figure 2.7: Structure for NaAlH_4 highlighting the complex Al-H anion.

each compound. To filter out the thermodynamically more promising candidates, first principles calculations can be employed to predetermine viability by calculating the enthalpy of desorption reaction, the critical quantity discussed in Section 2.4.[59] However, as mentioned above, DFT requires a crystal structure and as these are mostly novel compounds, their structures are largely unknown especially for mixed cation compounds. Experimentally determined structures are sparse for mixed cation alanates, and the situation is even worse for mixed cation borohydrides. This has generated the need for the capability to generate guess structures for the purpose of accessing the power of DFT for compounds for which there is no supporting experimental knowledge.[59]

2.7.2. The PEGS Method. To assist with the case of complex ionic hydrides, Majzoub and Ozolins have invented the PEGS method (prototype electrostatic ground state), an efficient way of searching a large configuration space of ionic compounds. The PEGS concept takes advantage of a few useful characteristics of ionic solids to form a computationally inexpensive approximation for the system energy based solely on point particle electrostatic forces, which are the largest players in the total energy of ionic hydrides. Chemistry is in most cases local. This remains generally true for these complex anions. Established electronic structure studies of

existing compounds, as well as diffraction data in experiment both demonstrate that the geometry, charge states, and anion center to vertex lengths are largely invariant with respect to chemical environment allowing anion models to be readily transferred from one chemical environment to another. The PEGS method uses Monte Carlo optimization to predict a ground state structure using the following Hamiltonian:

$$E_{tot} = \sum_{i>j} \frac{Q_i Q_j}{R_{ij}} + \sum_{i>j} \frac{\epsilon_{ss}}{R^{12}} \quad (2.34)$$

where the summations are over all ion pair potentials. The first term represents the electrostatic interactions of the ions, and the second represents a Pauli-exclusion repulsive term which is simply a hard shell potential that effectively disallows overlap of the nominal atomic radii. With this empirical potential, several candidate structures can be quickly generated to find a configuration with minimal electrostatic energy which can then be relaxed and comparatively evaluated with DFT.

The two object types in a PEGS minimization are the positively charged cations and the rigid model for the complex anion that charge balances the cation. The input parameters include the charge and hard sphere radius of each individual atom, the number of vertices of each complex anion, and the distance between the center and vertex atoms which remains fixed during the configuration search. The sphere radius can be extracted from nominal ionic radii found in the literature, and the center to vertex length can be taken from DFT calculations on other compounds. For example, the B-H distance found in DFT relaxed LiBH_4 structure can be used for the anion center-vertex length for B-H in the $[\text{BH}_4]^-$ anion if one were to search for a structure for MgBH_4 .

The global minimum energy in PEGS is found using Metropolis Monte Carlo. Configuration space is explored by allowing any of the following changes in random order one at a time: unit cell lattice parameters, translations of the cation or anion,

rotation of the anion, and swapping of the positions of an anion cation pair. Simulated annealing scheduling is used to control the efficiency of the minimization. In simulated annealing, the change in the system's energy according to equation 2.34 determines the probability of the transition such that steps that decrease the energy are automatically accepted while steps that increase the energy are accepted with the probability of a Boltzmann weighting factor. That is, the probability is modulated by a *temperature* parameter such that at high temperatures, states that increase the energy are more likely to be allowed. The simulation begins at a high temperature in which the ions move freely, as in a molten phase, exploring large areas of the configuration space. The temperature is then lowered, steadily decreasing the probability of large energy increases until the system finally settles on a local minimum. In practice, PEGS is run several times with different seeds for the internal pseudo-random generator. This results in multiple local minimums being identified, one of which is hoped to be the global minimum. The others are candidate polymorphs.

Further improvement is attained by smoothing of the potential energy surface in order to minimize the opportunities for the algorithm to get stuck in local minima. This is accomplished by scaling the interatomic distance R in equation 2.34 with a parameter $\alpha > 1$, such that $R' = R\alpha$. This allows the hard spheres of the ions to overlap during the first phases of the minimization without affecting the energy, allowing greater freedom for the system to find favorably structures. The proper physical distances are then enforced by gradually decreasing α to 1.

This method has enjoyed several successes. Notably, the known structures of NaAlH_4 , $\text{Mg}(\text{AlH}_4)_2$ and K_2LiAlH_6 are all reproduced and a structure with energy equal to that of the known ground state is produced for LiAlH_4 . [59] In some cases involving AlH_6 , PEGS finds new structures with lower DFT energy than those found in database searches raising interesting questions as to why the lower energy structures are not seen in nature. In separate works, a ground state structure for

Mg(BH₄)₂ was predicted with promising thermodynamics that allows for reversible hydrogen storage[60], and an energetically competitive candidate structure was found for CaBH₄. [40] Low energy structures were also found for the closoboranes CaB₁₂H₁₂, MgB₁₂H₁₂, and Li₂B₁₂H₁₂. [61] Most recently, structures were predicted for another closoborane Sc₂(B₁₂H₁₂)₂, and also the borohydrides Sc(BH₄)₃ and LiSc(BH₄)₄. [27]

2.7.3. Nanopegs. In the LiBH₄ adsorption study described in Section 4, we examine the energetics of the hydrogen storage materials LiBH₄ and LiH nanoconfined in a hard carbon environment by placing nanoclusters of the materials on a sheet of graphite within the density functional theory framework. To improve our odds of accurately representing the system in DFT, we require that the geometries of the clusters be in their minimum energy configurations, a task that would seem to lend itself to PEGS especially for a system like LiBH₄ with its complex [BH₄]⁻¹ anion. However, because of the large number of independent object geometries, using the above method to search the configuration space for a nanocluster can be prohibitively expensive computationally. Furthermore, the more complex potential energy surface results in higher risk of the search becoming trapped in local minima. To develop nanoclusters of LiBH₄ and LiH, we used the nanopegs method implemented by Majzoub et al. [42] This method employs a twist on a clever trick by Wang and Landau. [80] In an attempt to develop methods for determining partition functions, Wang and Landau needed a method by which to calculate accurate density of states from Monte Carlo. The simulated annealing method mentioned above tends to generate a very narrow sampling distribution around the temperature parameter. If one equates states sampled to a density of states, the distribution appears as $g(E)e^{\frac{-E}{k_b T}}$ which greatly under samples important regions far the the temperature and unnecessarily oversamples the narrow band wasting computation time and requiring multiple runs at several temperatures to get a complete partition function. To overcome this, Wang and Landau calculate a running density of states $g(E)$ as a function of how often a configuration

is accepted by MMC whose energy fits within a given energy bin. The probability of accepting a transition is then determined as a function of $g(E)$ per Equation 2.35 below

$$p(E_1 \rightarrow E_2) = \min \left[\frac{g(E_1)}{g(E_2)}, 1 \right]. \quad (2.35)$$

The effect is that states of any energy which have already been heavily sampled will be increasingly unlikely to be accepted, forcing the system to sample states of different energies. For their purposes, the result was a sampling histogram that was flat in energy, or effectively, a random walk in energy space.

Nanopegs adapts the random energy walk to avoid local wells. When the nanopegs algorithm finds a local minimum, it will continue to sample in that area updating $g(E)$ until the density of states term for that energy bin becomes so high that transitions to other energies are more likely than transitions that keep the system in the local minimum. This continues to occur for each energy bin in the well until the configuration is finally pushed over the well into an effective molten phase where it can renew the search of the potential energy surface for other deeper wells. This method was first used to obtain cluster geometries for NaAlH_4 , NaH , and Na_3AlH_6 in order to calculate cluster phase diagrams as a function of particle size and to predict the hydrogen desorption thermodynamics of nanoconfined NaAlH_4 . [42]

3 DFT PREDICTIONS OF HIGH-CAPACITY METAL HYDRIDE CONVERSION MATERIALS FOR LI-ION BATTERIES

3.1 INTRODUCTION TO LITHIUM-ION BATTERY MATERIALS

While current batteries are based on the Li insertion process in carbon anodes, greater capacity has been shown to be possible through conversion reactions. Specifically, Oumellal et al. have demonstrated the potential of a MgH_2 cathode that lithiates into Mg metal and LiH versus a metal lithium anode offering a capacity of $1,480 \text{ mAhg}^{-1}$ with an average voltage of 0.5V [58] versus a lithium metal anode. Unfortunately, this material experiences dramatically degraded reversibility after less than 20 cycles. This effect is believed to be largely due to fracturing that occurs during the large volume expansion of approximately 85% that accompanies the conversion reaction.

Silicon is another potential anode material of great interest. In the alloying process of lithium with silicon, each silicon atom can accommodate 4.4 lithium atoms forming $\text{Li}_{22}\text{Si}_4$ leading to a capacity of 4200 mAhg^{-1} , ten times that of a graphite anode. However, like MgH_2 , silicon is also hindered by large volume expansions upon lithiation (a 400% increase in volume, far more severe than the MgH_2 anode). During de-alloying, the shrinking of the material causes it to pulverize and crack, greatly decreasing material continuity, and thus reducing both ionic and electrical conductivity. The result is severe capacity fade as a large portion of the Li-ions become trapped in electrically disconnected particles. This effect was confirmed in an experiment in which conductivity was improved by applying pressure during de-alloying in order to increase the electrical contact between the pulverized particles.[26] While silicon nanowires have successfully been employed to overcome the fracturing problems with Li-Si alloys (see Figure 3.1),[12] one would expect that the empty space

between each nanowire means that the capacity per unit volume of these batteries is very poor.

In other attempts to mitigate the volume expansion, several compounds consisting of silicon finely dispersed via ball milling in an inactive host matrix have been studied. The idea is that the inactive material will inhibit pulverization by acting as a cushion to accommodate the expansion of the silicon. One example, CaSi_2 , performed for 10 cycles with a capacity of 1500 mAhg^{-1} , but subsequently fell to 310 mAhg^{-1} . It is thought that this degradation was due not only to persistent silicon pulverization, but to the alloy's inability to sustain the large volume changes.[26] To further

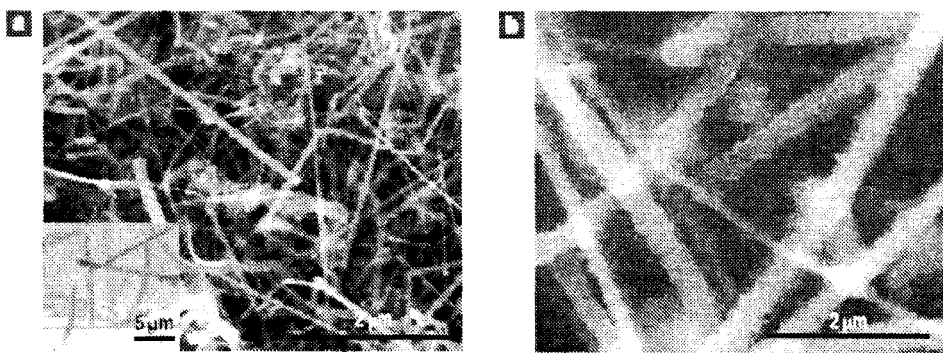


Figure 3.1: TEM imagery of silicon nanowires developed to combat the pulverization effects of silicon volume expansion taken from the work of Chan et al.[12] The left image shows pure silicon nanowires and the right shows fully alloyed Li_{22}S_4 . While excellent capacity per weight has been demonstrated, one can see here the large amount of empty space which suggests poor volumetric capacity

isolate the effects of pulverization, Si_3N_4 , a low-ductile material that can withstand the stresses, was investigated. In this material, reversibility was greatly enhanced, but capacity was reduced to a very poor 83 mAhg^{-1} .[26] The experiments on these two materials seem to confirm that volume expansion is both necessary for the high capacities, and responsible for the rapid degradation. This suggests that a material

that exhibits both high capacity and minimal volume expansion might perform very well in both capacity and reversibility.

Compounds rich in lithium that have been investigated for hydrogen storage applications are also attractive as battery materials. These are typically light-metal hydrides containing covalently bound complex anions such as $[\text{AlH}_4]^-$, $[\text{BH}_4]^-$, $[\text{NH}]^{-2}$, and $[\text{NH}_2]^-$, forming compounds such as LiBH_4 , LiNH_2 , LiAlH_4 , $\text{Mg}(\text{BH}_4)_2$, and $\text{Li}_2\text{Mg}(\text{NH})_2$. The crystal structures and phase stability of many of these compounds are already known, making first principles studies of this system possible.[36, 37, 56, 13, 49] Furthermore, the potential of practical lithium kinetics in metal hydrides has recently been demonstrated by the work of Matsuo et al.[45] whereby the high temperature phase of LiBH_4 was shown to have excellent lithium conduction. Maekawa et al.[38] and Miyazaki et al.[50] showed how this phase can be stabilized with the addition of LiI and other lithium halides. Fast ion kinetics have also been achieved with new complex hydrides involving $[\text{BH}_4]^-$ and $[\text{NH}]^{-2}$ anions.[46]

A detailed knowledge of the phase diagram for conversion compounds, as a function of lithium concentration, is necessary to design new electrodes. Useful thermodynamic models, that utilize first principles total energy calculations on a full set of possible compounds in phase-space, aid in the effort to understand and predict the reactions that might occur within a system of a given atomic composition. These models can be useful for searching the composition space for possible conversion materials where intuition may fail. In this work the Li-Mg-B-N-H multicomponent system is examined. We present a calculated phase diagram relevant for lithium-ion battery electrodes over an extensive set of stoichiometries by minimizing the grand canonical free energy as a function of the lithium chemical potential. This results in a five dimensional phase space with one axis for the atomic quantities of magnesium, boron, nitrogen, and hydrogen, plus one axis for the lithium electrochemical potential (i.e. the voltage). We note that our study trivially identifies the recently studied MgH_2

conversion reaction of Oumellal et al.[58], and within the wider phase space, predicts several noteworthy reactions with very high lithium density by mass.

3.2 LINEAR PROGRAMMING

In order to determine the competing phases present at equilibrium at a given temperature and lithium chemical potential, we calculate and minimize the grand canonical Gibbs free energy while the lithium chemical potential varies up to a potential corresponding to plating of metallic lithium at the anode. The method described below examines only the thermodynamics of the system and does not address kinetic mechanisms or their influence on reaction rates. Some of the reactions we predict may therefore be inhibited or slowed by activation barriers that we do not explore. For each possible phase we calculate the finite temperature Helmholtz free energy at 300 K, including entropy in the harmonic approximation. The atoms at each point in the phase diagram are distributed among a set of possible phases such that the total Gibbs free energy of the system (Equation 3.1) is minimized. We vary the lithium chemical potential, and assume an infinite lithium reservoir available to the electrode.

$$G(V) = \sum_a x_a (F_a - qV n_a^{Li}) \quad (3.1)$$

F_a is the free energy per formula unit for the anode phase, and x_a is the unknown molar fraction of those phases, and n_a^{Li} is the lithium count per formula unit in phase a of the anode. The first term in equation 3.1 describes the cohesive energies of all existing phases present in the anode and the second term describes the energy due to the chemical potential of lithium ions. The Gibbs free energy is minimized subject to the atomic quantity constraints in equation 3.2

$$A_s = \sum_a x_a n_a^s \quad (3.2)$$

where A_s is the total quantity of non-Li species “s” in the anode. Minimizing the free energy at varying lithium electrochemical potentials subject to the linear constraints is the GLCP method of Akbarzadeh et al.[3] and can be quickly accomplished through linear programming. The Gnu Linear Programming Kit (GLPK) package[70] in the open source numerical software package Octave[14] was utilized to solve for the molar fractions of each phase. For each set of atomic constraints, we vary the electrochemical potential of the anode Li atoms from 10 to 0 eV, representing a voltage swing of 10 to 0 volts versus Li/Li⁺. For small voltage steps, changes in molar fractions can be interpreted as conversion reactions that gain or lose lithium.

We scan the composition space (the multi-component phase diagram) to search for mass ratios that result in suitable conversion reactions. In this study, anode material in the Li-Mg-B-N-H system is scanned for reversible reactions that do not result in the creation of gases (N₂, H₂, NH₃, or B₂H₆) as byproducts. The phase space is explored by determining the molar fractions of coexisting phases for each point on a grid of atomic quantities A_s that samples the quaternary phase space of Mg-N-B-H within predetermined boundaries. The calculation on each point on the quaternary composition space results in a set of reactions that occur as the electrochemical potential of lithium is varied. For presentation, we reduce the dimensionality of the phase space by combining nitrogen and hydrogen onto a single axis, creating a pseudo-ternary phase diagram for each of several ratios of nitrogen and hydrogen. On each of these pseudo-ternary phase diagrams, a 20x20x20 array is used to sample 20³ points, such that the composition range shown in Table 3.1 is sampled to enough resolution that the phase boundaries are clearly visible in Figures 3.4.

First-principles DFT calculations using the Vienna Ab-initio Simulation Package (VASP) package were performed to obtain free energies for the candidate anode compounds within the phase space as shown in Table 3.2.[32, 33, 30, 31] The projector

Table 3.1: Boundaries of the explored space of atomic quantities A_s .

Element	Minimum	Maximum
Mg	0	4
B	0	4
N	0	6
H	0	15

augmented wave method (PAW), discussed in Section 2.2.5, was used for the interaction between conduction electrons and the ion cores,[8, 34] in combination with the correlation-exchange functional of Perdew and Wang.[63, 64] We employed a plane wave energy cutoff of 600 eV and Monkhorst-Pack k-point meshes of $4 \times 4 \times 4$ or larger. All structural parameters were relaxed until the forces on the ions were below 0.05 eV/Å and stresses were below 0.1 GPa.

Gamma phonons modes were also calculated using VASP linear response capability for vibrational contributions to the free energies at finite temperature. We present results for compounds at 300 K. The static energies, vibrational energies, volumes per formula unit, and the number of supercells used for each compound is listed in Table 3.2. Supercells were only used for very small unit cells such as the two metals and the single formula unit cell of Li_3N to ensure that some level of long range interactions were captured in the phonon calculations.

Some compounds resulted in unstable phonon modes. In the case of Li_3N , there is a single unstable phonon. This is in agreement with Yan and Zhang[83], who report that the B_{2g} mode is destabilized at slightly smaller volumes. Similarly, the mode in the present work stabilizes with increased volume suggesting that the instability may be a result of the harmonic approximation. Soft modes were also found in Mg_3N_2 , $\text{Mg}(\text{NH}_2)_2$, and $\text{Li}_4\text{BN}_3\text{H}_{10}$. In the case of Mg_3N_2 , these modes disappeared when the VASP Mg PAW pseudopotential was replaced with the Mg_pv

Table 3.2: First-principles DFT energies and enthalpies of formation for the anode and cathode phases at 300 K.

Phase	DFT Energy (eV/fu)	ΔH of form (kJ/mol*fu)	Zero point (kJ/mol*fu)	F_{vib} 300 K (kJ/mol*fu)	Volume/fu (\AA^3)	Unit cells for phonons
Li	-1.9	0	3.8	0.1	20.40	2x2x2
H ₂	-3.4	0	27.3	22.7	N/A	1x1x1
N ₂	-8.4	0	15.0	7.3	N/A	1x1x1
Mg	-1.5	0	2.9	-1.4	22.9	2x2x2
B-alpha	-6.7	0	12.4	12.0	7.3	1x1x1
NH ₃	-19.2	-100.8	90.9	78.0	N/A	1x1x1
B ₂ H ₆	-34.2	-35.5	162.1	138.4	N/A	1x1x1
LiH	-6.2	-85.1	19.7	18.3	16.1	1x1x1
LiNH ₂	-19.2	-202.7	68.6	62.6	32.7	1x1x1
Li ₂ NH	-17.7	-205.8	46.0	40.8	34.1	1x1x1
Li ₁ NH	-21.9	-246.6	48.6	40.2	58.5	1x1x1
Li ₁ BN ₃ H ₁₀	-82.0	-828.5	313.5	284.0	149.9	1x1x1
Li ₂ BNH ₆	-43.6	-418.5	176.0	163.2	92.2	1x1x1
Li ₃ N	-15.7	-162.0	27.8	20.9	44.6	2x2x2
LiN ₃	-27.5	-52.7	36.4	27.0	45.2	1x1x1
LiBH	-12.7	-72.0	36.5	33.8	27.1	1x1x1
LiBH ₂	-14.7	-62.4	51.8	47.1	35.0	1x1x1
LiBH ₄	-24.3	-207.5	106.2	98.2	56.5	1x1x1
LiMgH ₃	-15.1	-143.9	59.7	54.0	175.7	1x1x1
LiMgN	-14.0	-216.1	20.1	15.8	31.5	1x1x1
LiMgBN ₂	-31.8	-481.2	44.4	36.9	64.2	1x1x1
Li ₃ BN ₂	-34.4	-514.4	51.6	42.8	56.9	1x1x1
Li ₂ Mg(NH) ₂	-33.3	-425.6	84.4	75.5	64.5	1x1x1
Li ₂ Mg ₂ (NH) ₃	-47.8	-551.5	123.6	106.9	91.0	1x1x1
Mg(NH ₂) ₂	-35.8	-375.6	131.4	124.0	72.0	1x1x1
MgB ₂ H ₈	-44.8	-263.6	212.3	200.0	114.5	1x1x1
MgH ₂	-9.0	-63.3	36.1	34.2	30.4	1x1x1
Mg ₃ N ₂	-25.5	-400.9	26.5	16.2	62.3	1x1x1
Li ₂ B ₁₂ H ₁₂	-133.2	-806.2	458.4	444.4	255.8	1x1x1
MgB ₁₂ H ₁₂	-128.9	-611.2	446.8	425.3	296.3	1x1x1

in which the p core electrons are treated as valence indicating that some instabilities may be due to the frozen core approximation.

Battery electrodes often operate far from equilibrium, and forming metastable phases in the Li-Mg-N-B-H system may therefore be possible. In order to account for the most probable of these phases within the GCLP scheme, we have generated low energy structural candidates using the method of prototype electrostatic ground states (PEGS).[60, 59] The PEGS method has proven extremely successful in predicting the correct structure of ionic compounds containing complex anions and cations with structures including dimers (e.g. $[\text{NH}]^{2-}$ in Li_2NH , $[\text{NH}_2]^-$, in LiNH_2), tetrahedra (e.g. $[\text{BH}_4]^-$ in $\text{Ca}(\text{BH}_4)_2$)[40], and octahedra (e.g. $[\text{AlH}_6]^{3-}$ in K_2LiAlH_6).[59] Even in cases where the correct structure is not determined, the total energies of the candidate PEGS structures are often within a few meV per formula unit of the ground state, and therefore present excellent energy estimates for the type of rough-estimate calculations that are presented in this chapter. The following compounds were generated using PEGS: LiMgN , LiMgBN_2 , $\text{Li}_2\text{Mg}(\text{NH})_2$, and Li_3BN_2 . The recently discovered quaternary compound $\text{Li}_4\text{BN}_3\text{H}_{10}$ [65] was also included and used for experimental comparison.

3.3 EXPERIMENTAL METHODS

To compare our results with experiment, phase pure $\text{Li}_4\text{BN}_3\text{H}_{10}$ was infiltrated into an ordered nanoporous carbon (NPC) at 240°C under 60 bar H_2 by Xiangfeng Liu at the Center for Nanoscience at the University of Missouri-St. Louis. J. Hong, and J. Graetz at Brookhaven National Laboratory performed electrochemical measurements in a 2016 coin cell using a $\sim 10\text{mg}$ electrode composed of 90 wt% $\text{Li}_4\text{BN}_3\text{H}_{10}@C30$ and 10 wt% polytetrafluoroethylene (PTFE), which was pressed into a pellet. Lithium metal was used as the counter electrode (anode) and a solution of ethylene carbonate (EC) and dimethyl carbonate (DMC) (1:1 by volume) with 1 M LiPF_6 was used as

the electrolyte. Two electrochemical cells were prepared and each exhibited an open circuit voltage of 1.8 V (as-prepared). One cell was charged to 3.4 V at a current of 20 mA and the second cell was discharged to 0.05 V at a current of -20 mA.

3.4 RESULTS AND DISCUSSION

We first present results that can be compared with experimental C-V curves obtained from attempting to electrochemically cycle $\text{Li}_4\text{BN}_3\text{H}_{10}$ versus a lithium metal anode. This material does not appear in the phase diagrams below because there is gas release involved in the reactions. Nonetheless, we set the B:N:H ratio to 1:3:10 and vary the lithium chemical potential over a range corresponding to insertion and deinsertion. Figure 3.2 shows the experimental results, compared to the ideal C-V curve generated from our GCLP calculations shown in Figure 3.3. On delithiation, the relative capacities of each step in the reaction agree with experiment. The experimental voltage levels are over a volt higher for each step suggesting a large overpotential. On lithiation, the experiment does not compare as well with the predicted results, suggesting that it may be problematic to form nitrides, and boro-nitrides (Li_3N , and Li_3BN_2) as shown in Figure 3.3.

The results of the full phase diagram search can be seen in Figures 3.4, 3.5, and 3.6, which show the lithium capacity as a function of composition in the form of pseudo-ternary phase diagrams for several ratios of nitrogen and hydrogen. The phase field boundaries are generally discernible as changes in the contrast. In order to view only theoretically reversible reactions, a capacity of zero was assigned to any of the points in which any of the four gases (N_2 , H_2 , NH_3 , or B_2H_6) were present creating a visible dark blue forbidden region on the ternary plots. The highest capacity reactions exist on the borders of the active regions with the forbidden zone. Figure 3.4, for example, shows the pseudo-ternary phase diagram for a nitrogen to hydrogen ratio of 1:2. Two local maximums of lithium capacity can be clearly seen. A maximum

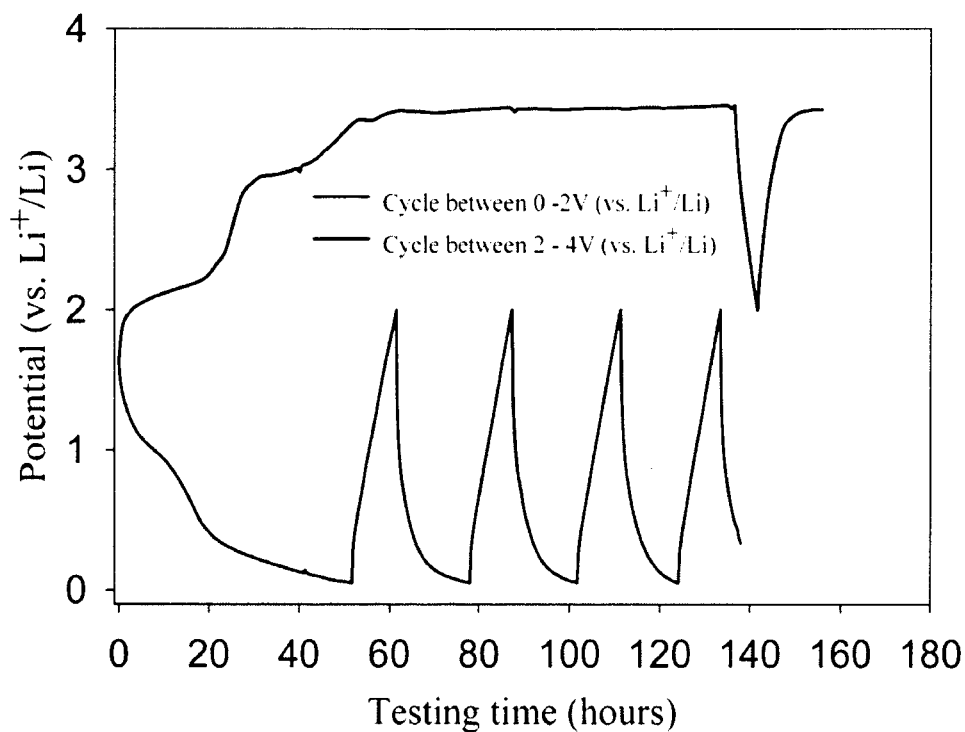


Figure 3.2: Experimental I-C curve for lithiation (red) and delithiation (blue) of $\text{Li}_4\text{BN}_3\text{H}_{10}$ infiltrated into nanoporous carbon.

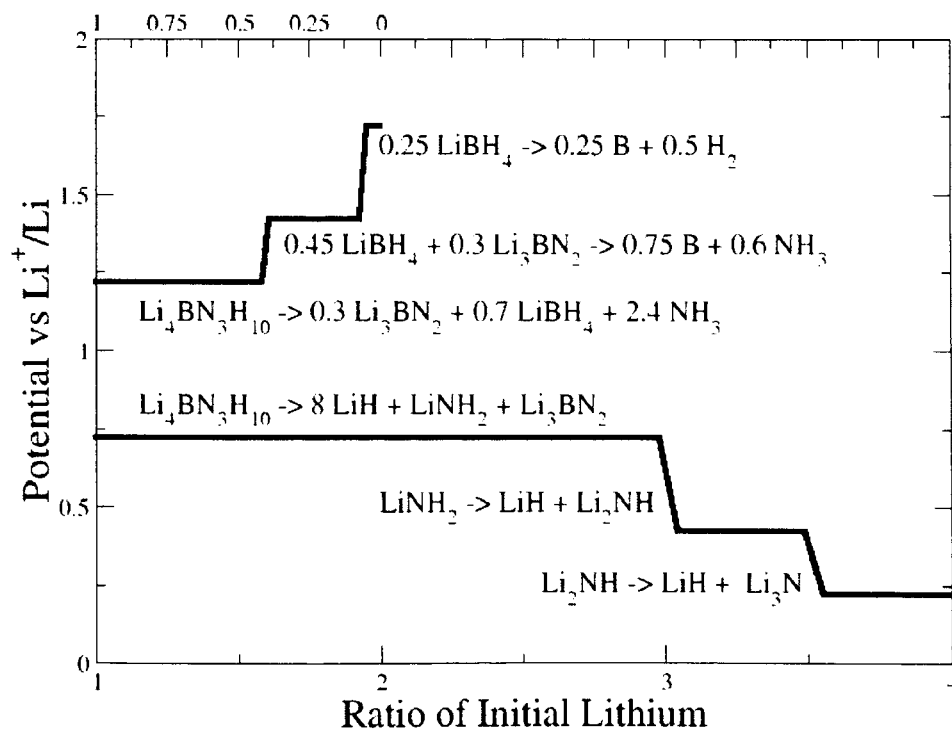


Figure 3.3: Idealized I-C curve predicted by GCLP for both lithiation (red) and delithiation (blue) of $\text{Li}_4\text{BN}_3\text{H}_{10}$.

exists on the zero boron line, with the stoichiometry of $\text{Mg}(\text{NH}_2)_2$, where a capacity of 3803 mAhg^{-1} is predicted. As one follows the border with the gas containing region into the boron rich area, the second local maximum can be found representing a theoretical anode consisting of $\text{B} + \text{Mg}(\text{NH}_2)_2$ in it's unlithiated state. Figure 3.5 shows the results when no nitrogen is present. Here, there is one clear global maximum where we find the compound MgB_2H_8 , magnesium borohydride, which is the most promising material found and is discussed below in further detail. The remaining plots of interest are shown together in Figure 3.6.

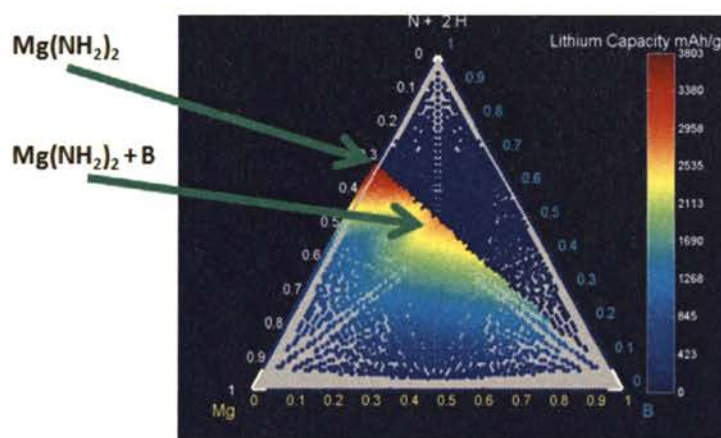


Figure 3.4: Pseudo-ternary phase diagram with N:H ratio of 1:2 in which $\text{Mg}(\text{NH}_2)_2$ is the highest capacity material.

Searching for local maximums in each of the ternary phase diagrams uncovered several promising materials with high capacities whose reaction pathways are listed in Table 3.3. All of the discovered reactions occur in multiple steps. A recurring class consists of varying initial mixtures of $\text{Mg}(\text{NH}_2)_2$ and MgB_2H_8 that are notable for their high capacities, competitive volume expansion, and the relative simplicity of their reaction pathways. Figure 3.7 shows the resulting weight percentages of phases upon lithiation of the mixture as a function of the unlithiated mixture. In the pure

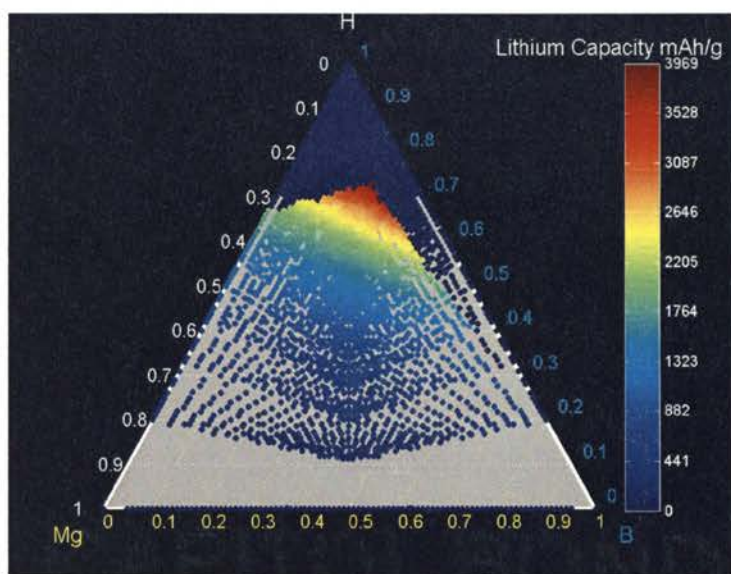


Figure 3.5: Pseudo-ternary phase diagram with no nitrogen content in which MgB_2H_8 is the highest capacity material.

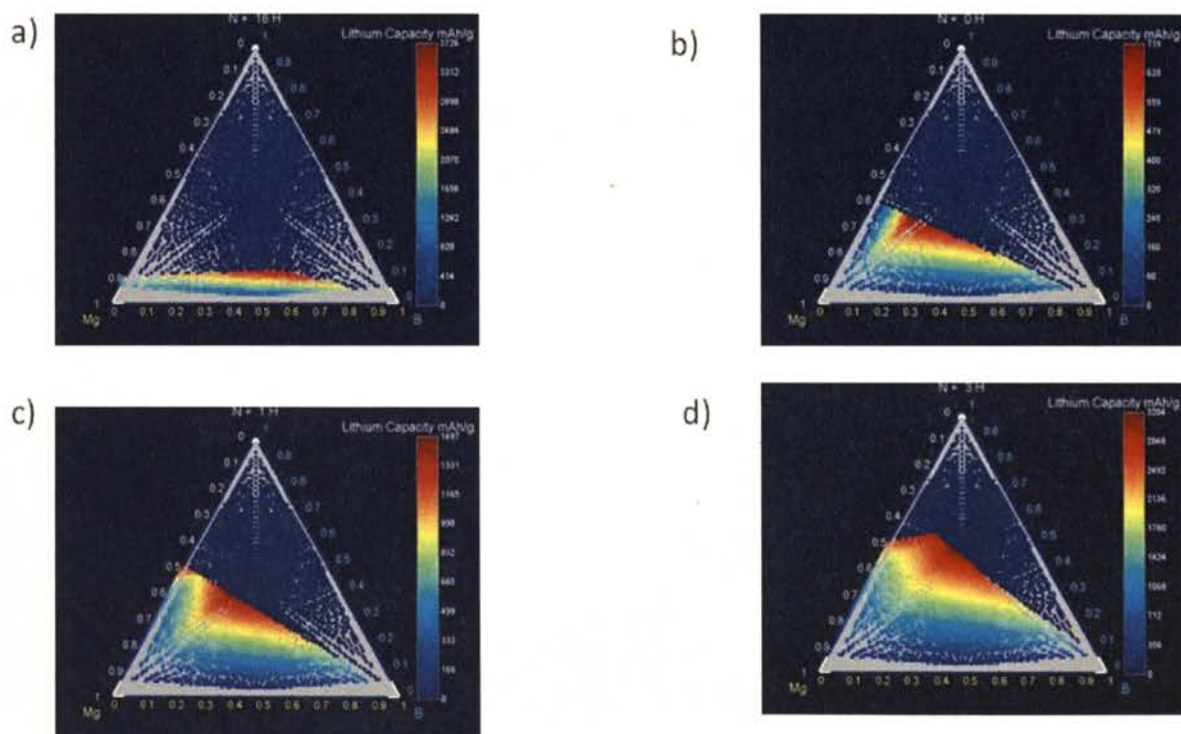


Figure 3.6: Pseudo ternary phase diagrams for nitrogen-hydrogen ratios of a) 1:18 b) 1:0 (zero hydrogen), c) 1:1, and d) 1:3.

$\text{Mg}(\text{NH}_2)_2$ state, the material lithiates to a mixture of LiH , Li_3N and Mg_3N_2 , a reaction differing from the traditional conversion reactions consisting of metal products in the lithiated state. At a mixture of 0.22 $\text{Mg}(\text{NH}_2)_2$, where the capacity is at a minimum, magnesium metal appears as a product, more resembling conventional conversion reactions. From this point in the mixture, the capacity rises linearly with one change of slope at 0.33 $\text{Mg}(\text{NH}_2)_2$, where pure boron also appears after lithiation. The capacities as a function of the mixture can be seen in the inset of Figure 3.7.

The best theoretical capacity of the mixture occurs for pure MgB_2H_8 . Fortunately, this material is also predicted to have the smallest increase in volume upon lithiation of only 42%, making it by far the most promising reaction. At 0.8 V with respect to Li/Li^+ , MgB_2H_8 converts to elemental boron, LiBH_4 , and MgH_2 , contracting in volume by 2% with an uptake of 744 mAhg^{-1} . Boron and MgH_2 react at 0.6 V to form metal Mg, and LiBH_4 , absorbing a further 248 mAhg^{-1} , and expanding to 11.2% of the initial volume, already an impressive capacity for the small expansion in volume. The bulk of the capacity comes from the final reaction at 0.5 V where LiBH_4 converts to boron and LiH , expanding to a final 43% with a final overall capacity of 3969 mAhg^{-1} .

Ten other materials (also listed in Table 3.3) were identified among local capacity maximums as candidate materials, although they are not predicted to perform as well as the above mixture on capacity or volume expansion. They are essentially mixtures of $\text{Mg}(\text{NH}_2)_2$, MgB_2H_8 , and Oumella's MgH_2 anode along with components of initial metal boron, and Mg_3N_2 . The largest expansion occurs in $\text{Mg}(\text{NH}_2)_2$, where the volume increases by about 100%, which still compares favorably with silicon. Adding boron as in $2\text{B} + \text{Mg}(\text{NH}_2)_2$ yields a smaller 75% expansion but renders the reaction less competitive by lowering its lithium capacity from 3803 mAhg^{-1} to 2405 mAhg^{-1} . An initial mixture of pure MgB_2H_8 performs remarkably well on both capacity and volume expansion yielding 3969 mAhg^{-1} with 43% expansion, significantly

lower than both the silicon and the MgH_2 anodes. Surprisingly, the first step during lithiation in this compound should result in slight physical volume contraction.

Table 3.3: Selected reactions at 300 K.

Reaction	Capacity (mAhg ⁻¹)	μ_{Li} (Volts)	Vol % inc
1) Mg=1; B=0; N=2; H=4 (3803 mAhg⁻¹) Discharged state: Mg(NH ₂) ₂			
Mg(NH ₂) ₂ → 2LiH + Li ₂ Mg(NH) ₂	1902	0.6	34
Li ₂ Mg(NH) ₂ → LiH + Li ₂ NH + LiMgN	951	0.4	58
Li ₂ NH → LiH + Li ₃ N	951	0.2	95
Final lithiated anode: 4LiH + Li₃N + LiMgN			
2) Mg=5; B=8; N=2; H=36 (3836 mAhg⁻¹) Discharged state: Mg(NH ₂) ₂ + 4MgB ₂ H ₈			
Mg(NH ₂) ₂ + 4MgB ₂ H ₈ → 7LiBH ₄ + LiMgBN ₂ + 4MgH ₂	787	1.0	4
7LiBH ₄ + 4MgH ₂ → 4Mg + 7B + 36LiH	2853	0.5	46
LiMgBN ₂ → Mg + Li ₃ BN ₂	197	0.1	49
Final lithiated anode: 36LiH + Li₃BN₂ + 7B + 5Mg			
3) Mg=1; B=2; N=0; H=8 (3969 mAhg⁻¹) Discharged state: MgB ₂ H ₈			
MgB ₂ H ₈ → 0.5B + 1.5LiBH ₄ + MgH ₂	744	0.8	-2.1
0.5B + MgH ₂ → Mg + 0.5LiBH ₄	248	0.6	11.2
2LiBH ₄ → 8LiH + 2B	2977	0.5	42.7
Final lithiated anode: 8LiH + 2B + Mg			
4) Mg=1; B=1; N=0; H=5 (3336 mAhg⁻¹) Discharged state: 0.5MgH ₂ + 0.5MgB ₂ H ₈			
0.5 MgB ₂ H ₈ → 0.25B + 0.75LiBH ₄ + 0.5MgH ₂	534	0.8	-1.7
0.25B + 0.5MgH ₂ → 0.5Mg + 0.25 LiBH ₄	200	0.6	8.9
LiBH ₄ + 0.5MgH ₂ → 0.5Mg + B + 5LiH	2668	0.5	50.7
Final lithiated anode: 5LiH + B + Mg			

Table 3.3: Selected reactions at 300 K cont.

Reaction	Capacity (mAhg ⁻¹)	μ_{Li} (Volts)	Vol % incr
5) Mg=5; B=4; N=8; H=24 (3204 mAhg⁻¹)			
Discharged state: 2B + MgB₂H₈ + 4Mg(NH₂)₂			
2B + Mg(NH ₂) ₂ → LiBH ₄ + LiMgBN ₂	178	1.6	7.4
MgB ₂ H ₈ + 0.25Mg(NH ₂) ₂ → 1.75LiBH ₄ + MgH ₂ + 0.25LiMgBN ₂	178	1.0	8.6
2.75LiBH ₄ + 2.75Mg(NH ₂) ₂ → 22LiH + 2.75LiMgBN ₂	1958	0.8	52.9
MgH ₂ → Mg + 2LiH	178	0.5	58.8
4LiMgBN ₂ → 4Mg + 4Li ₃ BN ₂	712	0.1	73.7
Final lithiated anode: 5Mg + 24LiH + 4Li₃BN₂			
6) Mg=2; B=2; N=1; H=11 (3513 mAhg⁻¹)			
Discharged state: 0.5MgH₂ + MgB₂H₈ + 0.5Mg(NH₂)₂			
MgB ₂ H ₈ + 0.25Mg(NH ₂) ₂ → 1.75LiBH ₄ + MgH ₂ + 0.25LiMgBN ₂	562	1.0	3.3
0.25LiBH ₄ + 0.25Mg(NH ₂) ₂ → 2LiH + 0.25LiMgBN ₂	562	0.8	13.2
1.5LiBH ₄ + 1.5MgH ₂ → 1.5Mg + 1.5B + 9LiH	2107	0.5	51.6
0.5LiMgBN ₂ → 0.5Mg + 0.5Li ₃ BN ₂	281	0.1	56.3
Final lithiated anode: 2Mg + 1.5B + LiH + 0.5Li₃BN₂			
7) Mg=3; B=1; N=2; H=0 (719 mAhg⁻¹)			
Discharged state: B + Mg₃N₂			
B + Mg ₃ N ₂ → 2Mg + LiMgBN ₂	240	0.7	57.9
LiMgBN ₂ → Mg + Li ₃ BN ₂	479	0.1	80.5
Final lithiated anode: 3Mg + Li₃BN₂			
8) Mg=1; B=1; N=2; H=4 (2792 mAhg⁻¹)			
Discharged state: B + Mg(NH₂)₂			
B + 0.5Mg(NH ₂) ₂ → 0.5LiBH ₄ + 0.5LiMgBN ₂	399	1.6	19.5
0.5LiBH ₄ + 0.5Mg(NH ₂) ₂ → 4LiH + 0.5LiMgBN ₂	1595	0.8	62.0
LiMgBN ₂ → Mg + Li ₃ BN ₂	798	0.1	81.8
Final lithiated anode: Mg + 4LiH + Li₃BN₂			

Table 3.3: Selected reactions at 300 K cont.

Reaction	Capacity (mAhg ⁻¹)	μ_{Li} (Volts)	Vol % incr
9) Mg=1; B=2; N=2; H=4 (2405 mAhg⁻¹)			
Discharged state: 2B + Mg(NH₂)₂			
2B + Mg(NH ₂) ₂ → LiBH ₄ + LiMgBN ₂	687	1.6	35.7
LiBH ₄ → B + 4LiH	1031	0.5	56.8
LiMgBN ₂ → Mg + Li ₃ BN ₂	687	0.1	74.9
Final lithiated anode: Mg + B + 4LiH + Li₃BN₂			
10) Mg=2; B=0; N=3; H=6 (3048 mAhg⁻¹)			
Discharged state: 0.12Mg₃N₂ + 0.25MgH₂ + 1.38Mg(NH₂)₂			
0.25MgH ₂ + 0.12Mg(NH ₂) ₂ → LiH + 0.12Mg ₃ N ₂	277	0.7	6.3
1.25Mg(NH ₂) ₂ → 2.5LiH + 1.25Li ₂ Mg(NH) ₂	1385	0.6	33.2
0.25Li ₂ Mg(NH) ₂ + 0.25Mg ₃ N ₂ → 0.5LiH + LiMgN	277	0.5	40.1
Li ₂ Mg(NH) ₂ → LiH + Li ₂ NH + LiMgN	554	0.4	55.1
Li ₂ NH → LiH + Li ₃ N	554	0.2	78.2
Final lithiated anode: 6LiH + 1.67Li₃N + 0.67Mg₃N₂			
11) Mg=6; B=4; N=3; H=27 (3267 mAhg⁻¹)			
Discharged state: 2.5MgH₂ + 2MgB₂H₈ + 1.5Mg(NH₂)₂			
2MgB ₂ H ₈ + 0.5Mg(NH ₂) ₂ → 3.5LiBH ₄ + MgH ₂ + 0.5LiMgBN ₂	415	1.0	2.5
LiBH ₄ + Mg(NH ₂) ₂ → 8LiH + LiMgBN ₂	830	0.8	18.7
2.5LiBH ₄ + 4.5MgH ₂ → 4.5Mg + 2.5B + 19LiH	1711	0.5	56.3
1.5LiMgBN ₂ → 1.5Mg + 1.5Li ₃ BN ₂	311	0.1	61.9
Final lithiated anode: 6Mg + 2.5B + 27LiH + 1.5Li₃BN₂			

Table 3.3: Selected reactions at 300 K cont.

Reaction	Capacity (mAhg ⁻¹)	μ_{Li} (Volts)	Vol % incr
12) Mg=10; B=13; N=3; H=60 (3555 mAhg⁻¹)			
Discharged state: 0.25Mg₃N₂ + 1.5MgH₂ + 6.5MgB₂H₈ + 1.25Mg(NH₂)₂			
0.25Mg ₃ N ₂ + 0.14MgB ₂ H ₈ + 0.04Mg(NH ₂) ₂ → 0.64 MgH ₂ + 0.29LiMgBN ₂	17	1.1	0.3
4.86MgB ₂ H ₈ + 1.21Mg(NH ₂) ₂ → 8.50LiBH ₄ + 4.86MgH ₂ + 1.21LiMgBN ₂	535	1.0	3.2
1.5MgB ₂ H ₈ → 0.75B + 2.25LiBH ₄ + 1.5MgH ₂	127	0.8	2.8
0.75B + 1.5MgH ₂ → 1.5Mg + 0.75LiBH ₄	39	0.6	5.3
11.5LiBH ₄ + 7MgH ₂ → 7Mg + 11.5B + 60LiH	2673	0.5	47.5
1.5LiMgBN ₂ → 1.5Mg + 1.5Li ₃ BN ₂	165	0.1	50.1
Final lithiated anode: 10Mg + 11.5B + 60LiH + 1.5Li₃BN₂			

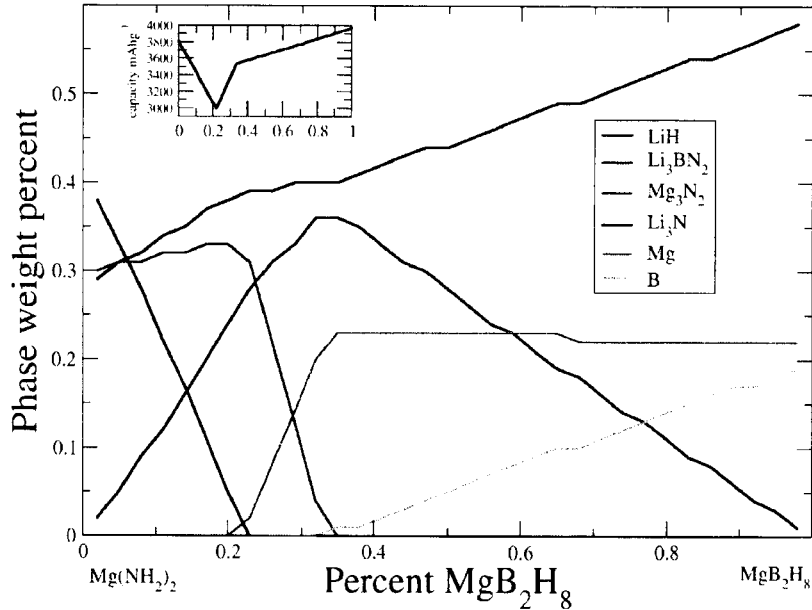


Figure 3.7: Phases after lithiation of the $\text{Mg}(\text{NH}_2)_2 / \text{MgB}_2\text{H}_8$ mixture. The left side of the graph represents pure $\text{Mg}(\text{NH}_2)_2$ and on the far right is pure MgB_2H_8 . The inset shows lithium capacity as a function of the initial mixture

All of the reaction sets we have identified consist of multiple steps. This naturally implies that the C-V traces in experimental measurements will have multiple steps corresponding to the lithium chemical potential for each successive reaction. Figure 3.8 shows the idealized C-V curves predicted for the reaction sets in Table 3.3. While reaction 4 performs better on volume expansion, reaction 3 represents higher energy density due to the 3.4 volt reaction compared with 3.0 volts for reaction 4. Remarkably, the first lithiation step in systems 3 and 4, with potentials of 2.7 and 2.9 volts, have very low volume increases of 9.7% and 18.7%, respectively.

3.5 INCLUSION OF BORONITRIDE

It is important to note that in this study, the graphite like compound boronitride (BN) was omitted even though it is thermodynamically very stable. This can be justified by considering that the known synthesis techniques of BN require very

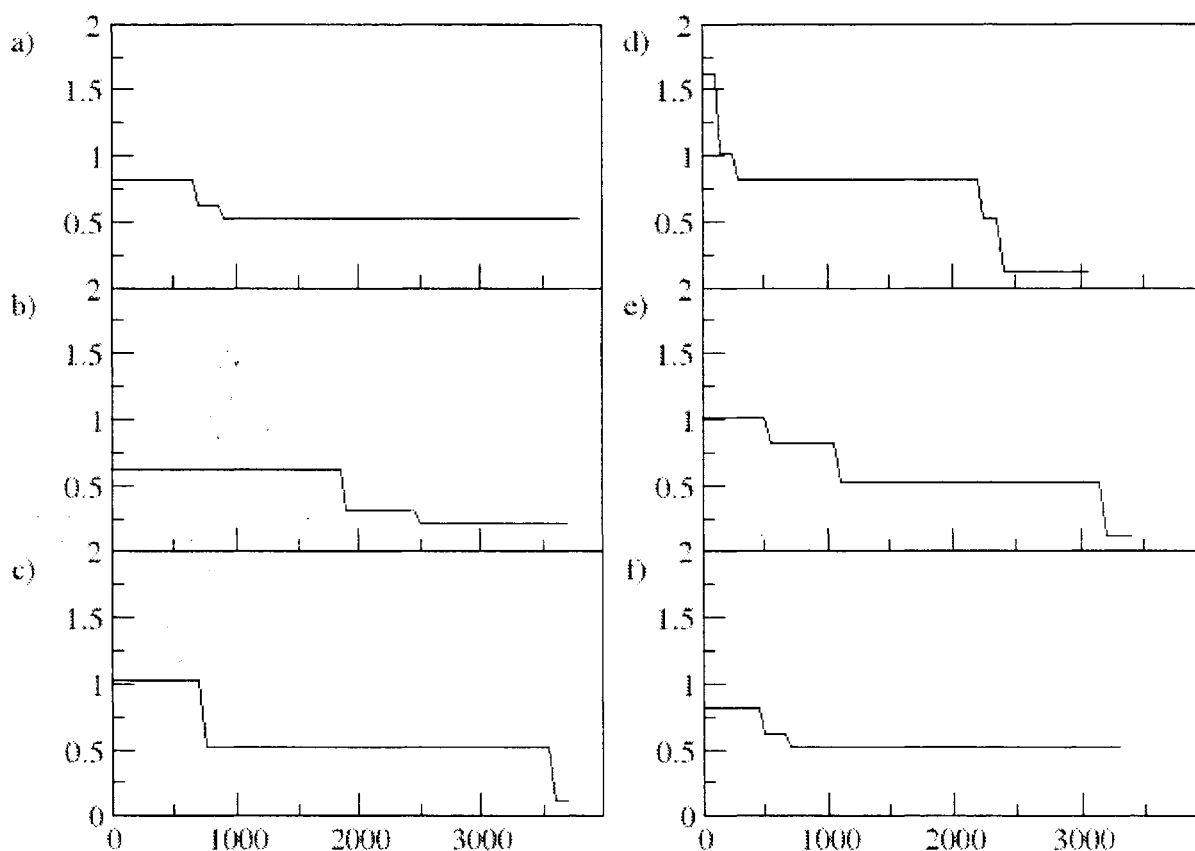
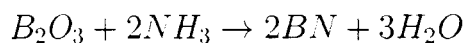


Figure 3.8: Idealized C-V plots versus Li^+/Li for selected mixtures. a) MgB_2H_8 , b) $\text{Mg}(\text{NH}_2)_2$ c) $\text{Mg}(\text{NH}_2)_2 + 4 \text{MgB}_2\text{H}_8$ d) $2\text{B} + \text{MgB}_2\text{H}_8 + 4\text{Mg}(\text{NH}_2)_2$ e) $0.5 \text{MgH}_2 + \text{MgB}_2\text{H}_8 + 0.5 \text{Mg}(\text{NH}_2)_2$ f) $\text{MgH}_2 + \text{MgB}_2\text{H}_8$. The corresponding reaction steps can be found in Table 3.3

high temperatures far above typical operating temperatures for a lithium-ion battery. The synthesis technique with the lowest temperature commonly used today reacts boric-acid with ammonia at 900°C per the reaction below.[69]



Nonetheless, it is worth discussing the impact to the calculations when BN is included. Generally, hexagonal BN is thermodynamically preferred anywhere in the phase diagram where both boron and nitrogen are present. This has an effect of greatly reducing the solution space of non gas emitting mixtures as well as reducing

the capacity of most existing solutions as many of them now contain essentially inert amounts of BN. Figure 3.9 below shows the pseudo-ternary phase diagram for an N:H ratio of 1:2 when BN is included as a phase. By comparing this with Figure 3.4,

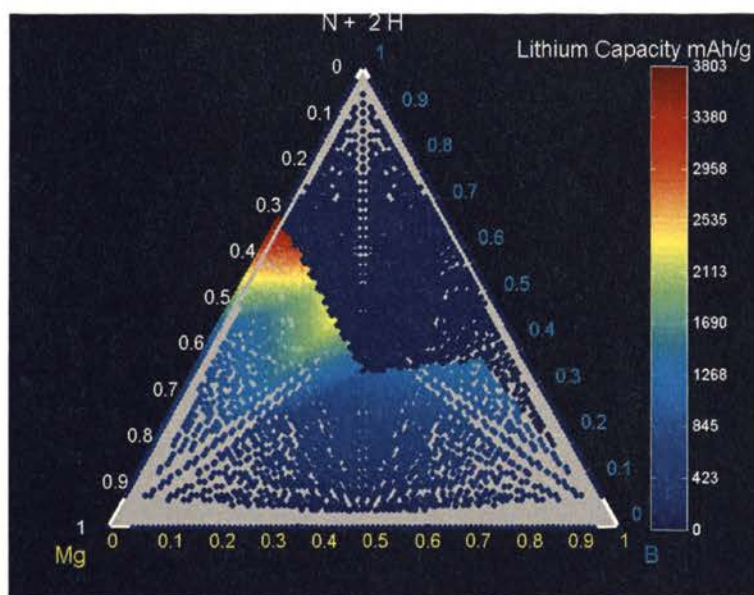
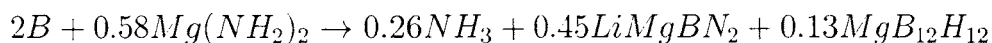


Figure 3.9: Pseudo-ternary phase diagram with N:H ratio of 1:2 with BN included as a candidate phase.

it can be seen that a large region of the solution space has been converted to the forbidden gas emitting region. Including BN causes every reaction listed in Table 3.3 to emit H_2 except for those that either contain no boron (reactions 1 and 10), no nitrogen (reactions 3 and 4), or no hydrogen (reaction 7). Fortunately, the two high capacity MgB_2H_8 and $Mg(NH_2)_2$ reactions discussed above fall under this category and survive the inclusion of BN.

3.6 INCLUSION OF CLOSOBORANES

Ozolins, Wolverton, and Majzoub investigated lithium and magnesium closoboranes ($\text{Li}_2\text{B}_{12}\text{H}_{12}$, and $\text{MgB}_{12}\text{H}_{12}$) as intermediate phases in hydrogen storage reaction of various borohydrides.[61] PEGS[60, 59] was employed in this work to predict ground state structures for these compounds. In the present work, these phases were neglected because they are not observed to form until 700-800 K in hydrogen storage experiments.[57] However, calculations using the resulting structures were added to the anode phase space to investigate their potential impact on the linear programming calculations. When included, the closoboranes appear as intermediate compounds in boron containing reactions. Final lithiated states are not affected except for reactions 8 and 9. These two reactions have starting materials of $\text{Mg}(\text{NH}_2)_2$ and varying amount of bulk boron and in both cases, including closoboranes causes NH_3 gas production in the first step per the reaction below:



Even these reactions can be salvaged by tuning the stoichiometry. Reaction 9 can be saved by lowering the nitrogen and hydrogen content by the amount in the produced ammonia. This results in the complex but thermodynamically viable reaction detailed in Table 3.4.

3.7 CHEMICAL POTENTIAL FOR GAS PHASES

Missing from these calculations is the inclusion of the chemical potential for the gas phases(H_2 , N_2 , NH_3 , and B_2H_6). A more precise treatment would have included the pressure dependent entropic term of the canonical ensemble for the gas phases

described by Equations 3.3 and 3.4 below.[28]

$$\mu = \tau \ln \left(\frac{n}{n_q} \right) \quad (3.3)$$

$$n_q = \left(\frac{m\tau}{2\pi\hbar^2} \right)^{\frac{3}{2}} \quad (3.4)$$

Here, μ is the chemical potential, n is the volumetric density, n_q is the quantum concentration, τ is the fundamental temperature, and m is the mass of the gas species. Using the ideal gas law, the chemical potential can be related to any given partial pressure, and for real gases it can be similarly related to the fugacity. As we assumed a μ of 0, this implies a concentration equal to that of the quantum concentration. For the case of H_2 , under the ideal gas approximation, this implies an assumed pressure of approximately 11.5 GPa. At a standard pressure of 101 kPa, this would lower the free energy of H_2 species by 0.301 eV per molecule destabilizing all reactions except for reaction 1, 3, 4, and 7. The fugacities required to inhibit gas creation were calculated for each gas species for each reaction and are tabulated in Table 3.5. This physical quantity represents the pressure that an enclosure around the material would be required to withstand to maintain a stable gas solid mixture if the gas was ideal.

Table 3.4: Reaction 9 with closoboranes tuned to eliminate NH_3 gas.

Reaction	μ_{Li} (Volts)	Vol % incr
Mg=1; B=2; N=1.74; H=3.22 (2123 mAhg⁻¹)		
Discharged state: 2B + 0.6 Mg₃N₂ + 0.81 Mg₃N₂		
2B + 0.06Mg ₃ N ₂ + 0.39Mg(NH ₂) ₂ → 0.45LiMgBN ₂ + 0.13MgB ₁₂ H ₁₂	0.6	20.2
0.15Mg(NH ₂) ₂ + 0.13MgB ₁₂ H ₁₂ → 0.13MgB ₂ H ₈ + 0.15LiMgBN ₂ + 0.09Li ₂ B ₁₂ H ₁₂	2.1	23.2
0.26Mg(NH ₂) ₂ + 0.06Li ₂ B ₁₂ H ₁₂ → 0.44LiBH ₄ + 0.26LiMgBN ₂	2.2	33.7
0.13MgB ₂ H ₈ → 0.17LiBH ₄ + 0.13MgH ₂ + 0.01Li ₂ B ₁₂ H ₁₂	2.6	33.3
0.61LiBH ₄ + 0.13MgH ₂ → 0.13Mg + 2.09LiH + 0.05Li ₂ B ₁₂ H ₁₂	3.0	48.5
0.09Li ₂ B ₁₂ H ₁₂ → 1.13B + 1.13LiH	3.2	55.1
0.87LiMgBN ₂ → 0.87Mg + 0.87Li ₃ BN ₂	3.4	72.9
Final lithiated anode: Mg + 1.13B + 3.22LiH + 0.87Li₃BN₂		

While these results may at first seem devastating, one must keep in mind the limits of the ideal gas approximation. That is, while these were the tools most readily available to make these calculations, one must consider the crudeness of using the ideal gas law, a theory which assumes zero interaction between particles, in conjunction with the concept of the quantum concentration, a state in which component wave functions are in contact. There is reason, therefore, to suspect that the fugacities listed in Table 3.5 deviate significantly from the actual pressures that would be required of a container to maintain stability, although they might be useful quantities for determining the relative stability of each potential conversion material.

3.8 CONCLUSIONS

In conclusion, a new method is proposed to search for very complex conversion materials for reversible lithium-ion batteries using energies calculated from density functional theory. This method is adopted from the GCLP method[3] for hydrogen fuel cell reactions. Further refinement can be achieved by phonon calculations on each compound to produce zero point and temperature dependent energies. The method only reveals thermodynamic points of maximum stability and says nothing about kinetics. Experimentation is needed to test viability.

With this method we have calculated a multi-component phase diagram for the Li-Mg-B-N-H system as a function of lithium electrochemical potential at 300 K and have identified several sets of multi-step reactions that are candidates as high capacity conversion materials. Reactions involving the release of hydrogen, nitrogen, ammonia, and diborane were discarded. The highest capacity reactions discovered are mainly mixtures (in the unlithiated state) of MgH_2 , $\text{Mg}(\text{BH}_4)_2$, and $\text{Mg}(\text{NH}_2)_2$. The largest capacity material in the discharged state is found to be pure $\text{Mg}(\text{BH}_4)_2$, with a fully lithiated capacity of 3969 mAhg^{-1} , resulting in $\text{Mg} + 2\text{B} + 8\text{LiH}$ after lithium saturation. This material is also predicted to have the smallest volume expansion at

42% in the fully lithiated state which is suspected to be a predictor of good cyclability. This compares very favorably with competing materials, such as silicon, provided lithium mobility can be maintained. Pure $\text{Mg}(\text{NH}_2)_2$ lithiating into $4\text{LiH} + \text{Li}_3\text{N} + \text{LiMgN}$, with a predicted capacity of 3803 mAhg^{-1} is the other leading reaction and is unique in that it does not rely on LiBH_4 as a major component of capacity. It's volume, however, increases by a less competitive 95%. While inclusion of the hexagonal BN phase greatly reduces the solution space, it is argued that since it can only be synthesized at high temperatures, the action potential of a BN forming reaction can be assumed to be high enough to render the phase kinetically irrelevant at lithium ion battery operating temperatures. Including closoboranes shifts the phase diagrams to slightly less competitive regions but these are neglected since, again, they are only observed to form at high temperatures. A thorough experimental effort to explore the predicted high-capacity regions of the phase space may provide for fundamentally new lithium-ion conversion reactions.

Table 3.5: Fugacities required for reaction stability.

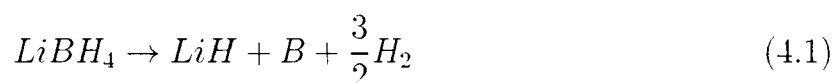
Reaction	Fugacity H ₂ (KPa)	Fugacity N ₂ (KPa)	Fugacity NH ₃ (KPa)	Fugacity B ₂ H ₆ (KPa)
1) Mg(NH ₂) ₂	1.018	$8.6 \cdot 10^{-14}$	$8.2 \cdot 10^{-4}$	NA
2) Mg(NH ₂) ₂ + 4 MgB ₂ H ₈	$5.3 \cdot 10^6$	$1.3 \cdot 10^{-35}$	$1.5 \cdot 10^{-4}$	$8.2 \cdot 10^{-16}$
3) MgB ₂ H ₈	1.018	NA	NA	$8.2 \cdot 10^{-16}$
4) 0.5 MgH ₂ + 0.5 MgB ₂ H ₈	1.018	NA	NA	$8.2 \cdot 10^{-16}$
5) 2 B + MgB ₂ H ₈ + 4 Mg(NH ₂) ₂	$5.8 \cdot 10^6$	$1.8 \cdot 10^{-14}$	$5.9 \cdot 10^6$	$5.6 \cdot 10^5$
6) 0.5 MgH ₂ + MgB ₂ H ₈ + 0.5 Mg(NH ₂) ₂	$5.8 \cdot 10^6$	$2.7 \cdot 10^{-35}$	$2.3 \cdot 10^{-4}$	$8.2 \cdot 10^{-16}$
7) B + Mg ₃ N ₂	NA	$1.8 \cdot 10^{-59}$	NA	NA
8) B + Mg(NH ₂) ₂	$5.8 \cdot 10^6$	$1.8 \cdot 10^{-14}$	$5.9 \cdot 10^6$	$5.6 \cdot 10^5$
9) 2B + Mg ₃ N ₂	$4.9 \cdot 10^6$	$1.8 \cdot 10^{-14}$	$5.9 \cdot 10^6$	$5.6 \cdot 10^5$
10) 0.12 Mg ₃ N ₂ + 0.25 MgH ₂ + 1.38 Mg(NH ₂) ₂	$2.5 \cdot 10^6$	$8.7 \cdot 10^{-14}$	$1.1 \cdot 10^{-4}$	NA
11) 2.5 MgH ₂ + 2 MgB ₂ H ₈ + 1.5 Mg(NH ₂) ₂	$5.8 \cdot 10^6$	$2.7 \cdot 10^{-35}$	$2.3 \cdot 10^{-4}$	$8.2 \cdot 10^{-16}$
12) 0.25 Mg ₃ N ₂ + 1.5 MgH ₂ + 6.5 MgB ₂ H ₈ + 1.25 Mg(NH ₂) ₂	$3.9 \cdot 10^6$	$5.9 \cdot 10^{-35}$	$1.5 \cdot 10^{-4}$	$8.2 \cdot 10^{-16}$

4 DFT STUDY OF NANOCUSTER LITHIUM BOROHYDRIDE ENERGETICS ON CARBON NANOSCAFFOLDS

4.1 INTRODUCTION

For hydrogen storage systems to be an economically viable means of energy storage for automobiles acceptable to an average customer, they will have to be competitive with petroleum in cost, energy stored per volume, and energy stored per mass. Currently, the target set forth by the United States Department of Energy is 7.5% hydrogen content by mass for use by light duty vehicle[55].

In order to find metal hydrides with large hydrogen densities per mass, researchers have focused on host materials with light metal atoms. With a theoretical hydrogen storage capacity of 18.5% by mass, well above the DOE target, LiBH_4 has garnered much attention from researchers as a potential hydrogen storage material with the capacity requirements suitable for light duty vehicles. The compound has two known possible desorption pathways described by equations 4.1 and 4.2, where reaction 4.1 is how the bulk is observed to desorb with an enthalpy of $74 \text{ kJ mol}^{-1} \text{ H}_2$. [47]



Unfortunately, in its bulk form, it is too stable for practical automotive use, releasing hydrogen only after heating to 400°C . Further discounting the material, reversibility is very poor as bulk LiBH_4 rehydrogenates to only 8.3% after 200 minutes of 600°C temperature and 155 bar of pressure. Two primary strategies have been attempted to engineer composite materials around LiBH_4 with more practical properties. The first approach is to introduce catalysts such as Pt, Ni, and carbon nanomaterials. This has yielded some success in lowering the desorption temperature. Ball milling with

Ni, for example, has been shown to lower the desorption temperature to 300 °C but does not adequately improve the recharging conditions (600 °C, 100 bar for 30 hr to charge to 12 wt% H₂). [53]

The second approach has been to confine the particle size of the metal hydride in order to evoke surface kinetics and thermodynamics more favorable to hydrogen release. The kinetic effect can be understood to be a result of the lower coordination number of the hydrogen atoms on the surface of the nanoparticle as compared to the bulk which results in weaker bonding. The weaker bonding of the surface hydrogen atoms manifests as lower observed desorption temperatures. Ngene, Zwielen, and de Jong report a decrease in desorption temperature of approximately 100-150 °C after confining LiBH₄ in a porous carbon with a surface area of 500 m²g⁻¹ as measured by Brunauer-Emmett-Teller (BET). Reversibility is significantly improved by the nanoconfinement with the composite sample releasing 5.8 wt% H₂ after being recharged at relatively mild conditions of 320 °C and 40 bar for 120 minutes. When combining the scaffolding with the Ni catalysts, reversible releases of 9.2 wt% H₂ were reported. [53]

The work of Liu, Peaslee, Jost and Majzoub, [35] sheds further light on how the decomposition pathways of LiBH₄ may be altered by nanoconfinement. In that experimental study, highly ordered nanoporous carbons were prepared by organic-organic assembly of copolymers PEO-PPO-PEO with resols via an evaporation induced self-assembly technique. This results in a carbon material with highly ordered pores featuring a very narrow pore size distribution as can be seen by the TEM imagery in Figure 4.1, and an average diameter of approximately 2 nm. LiBH₄ was physically mixed and then melt infiltrated into the carbon pores at 300 °C and 60 bar of H₂. This composite material was dehydrogenated via increased temperature and rehydrogenated through cooling and H₂ pressure.

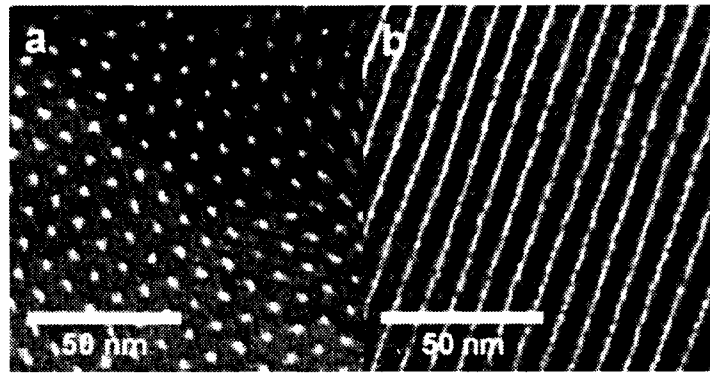


Figure 4.1: TEM images of highly ordered nanoporous carbon of Liu et al.[35]

The nanoporous carbon environment was found to have four important observable effects at the 2 nm pore size.

- 1) XRD of the sample showed a lack of any LiBH_4 signal. For an ordered material, one would expect to find the peaks found in bulk LiBH_4 broadened by the small particle size. The lack of these broadened peaks suggests that it is amorphous at 2 nm confinement. This affect is not found in similar experiments of LiBH_4 confinement in 25 nm carbon aerogels.[20]
- 2) Differential scanning calorimetry (DSC) data showed no heat of a phase transition from the orthorhombic to hexagonal phase typical of bulk LiBH_4 , nor does it show heat of a melting transition, confirming that the material is truly amorphous.
- 3) The temperature at which hydrogen gas was desorbed from the nanocomposite was reduced significantly to 220°C as compared to 460°C in the bulk.
- 4) The release of diborane (B_2H_6), which is observed in the desorption of bulk LiBH_4 appeared to have been eliminated at the 2 nm pore size based on data from a gas analyzer hinting at a change in the reaction pathways.

As the authors state, it is unclear whether these observables are due to the size effects of the nano-scaffolding or to the interactions of the hydride with the scaffolding carbon, which may cause lattice strains or other affects. Furthermore, it is very difficult to determine this experimentally as one cannot reduce the particle size without also increasing the interacting surface area. The problem lends itself, therefore, to first principles calculations to investigate the mechanisms of the changing chemistry. Size effects can be calculated with first principles, as was done in recent work by Majzoub et al., in which a phase diagram of NaAlH_4 hydrogen desorption reaction pathways was predicted as a function of nanoparticle size.[39] Adding a simulated carbon environment to the calculation allows one to compare the effects of size with the effects of carbon interaction. To gain understanding of the experimental effects reported by Liu et al., we attempt first principles calculations that model the LiBH_4 hydrogen storage reactions in the nanoporous carbon environment. We also compare some of our results with DFT work done by Valencia et al.[78] on the adsorption of single lithium atoms on a graphite surface.

4.2 METHODS

4.2.1.DFT Methods. We employ the VASP package to calculate total DFT energies as a function of geometric configurations of Li-B-H adsorbate compounds of varying particle size on a carbon surface. For the DFT calculations, the VASP package[32, 33, 30, 31] was used with ion potentials represented with the projector augmented wave method (PAW)[8, 34] in combination with the correlation-exchange functional of Perdew and Wang.[63, 64] A plane wave energy cutoff of 600 eV was chosen for a basis set and because the unit cells for these calculations are very large, only one K-point at gamma was used for most calculations but selected runs were refined with a 2x2x1 Monkhorst-Pack grid. All structural parameters were relaxed

until the forces on the ions were below $0.05 \text{ eV}/\text{\AA}$. Phonons and free energies at finite temperatures were not calculated for this study.

4.2.2. Approximations. Modeling amorphous carbons with a large amount of disorder does not lend itself well to plane wave calculations and would be beyond the abilities of the available computational resources. As an approximation, we model the carbon environment as a single graphene sheet of infinite surface area and place the material of interest directly above the surface. The adsorbate material is then allowed to relax to a local minimum energy configuration. This was done for each component of the reaction: lithium, lithium hydride, boron and lithium borohydride at a varying number of formula units.

Other approximations were made in this work that merit discussion. First, beyond our assumption that the host material is placed directly on a block of graphite, we neglect the affect of the graphene layers below the surface of the pore. Wang et al.[81] in their DFT study of platinum nanoparticles adsorption on graphite, report that extra carbon layers beyond the first had no effect on their results. This makes intuitive sense given the electronic isolation of each carbon sheet in graphite, in which the carbon layers interact only through weak Van der Waals interactions. A study by Valencia et al. on lithium adsorption on graphite reports that while geometries are not significantly affected by the number of layers used, binding energies do increase by about 0.1 eV when a second layer is included, but a third layer adds no significant change.[78] We can thus presume that for the relatively strongly reacting adsorbates (lithium and boron), excluding the sheet will causes us to slightly underestimate the binding energies.

The same study also finds significant effects from the number of k-points used on the bonding energy of the lithium adsorption system. They note a change in bonding energy from 0.76 eV for a single gamma k-point to 1.55 eV when using a 9 k-points grid on their 32 atom system surface. They show that this is due to the

fact that in the gamma calculation, the first excited state is far above the Fermi level, which raises the resulting energy of the charge transferred from the lithium atom. For expediency, the bulk of our work was nonetheless done primarily with only a gamma k-point for the purpose of finding optimum geometries and only the final optimum configurations were recalculated with a Monkhorst sampling grid of $2 \times 2 \times 1$.

We also assume that the graphene sheet itself is not perturbed in any way by the active material. For example, we assume that the inter-atomic distance between the carbon atoms on the sheet when active material is adsorbed is the same as for the graphene sheet in isolation. In fact, calculations performed by Medeiros et al.[48] and duplicated by us predict that this may be a rough assumption. For example, DFT predicts that a single graphene sheet with full adsorption of lithium on either side has an inter-atomic distance between carbon atoms of 1.54 \AA versus 1.42 \AA for the isolated sheet. This can be understood from considering that the nearest neighbor distance in metallic lithium is 2.98 \AA in DFT calculation which is greater than the second nearest neighbor distances on the graphene sheet of 2.48 \AA on which the adsorbed lithium atoms reside. The sheet must thus expand to accommodate the repulsive forces between the lithium atoms. The presence of the lithium also causes a separation between nearest neighbor carbon in the direction perpendicular to the sheet. A graphic from Medeiros et al. shown in Figure 4.2 illustrates the perturbative effects of the lithium monolayer. Because of the need to reduce complexity, we nonetheless persist with this approximation. It is hoped that carbon expansion may be limited by the larger framework of the carbonaceous material as well as the small number of adsorbate atoms we use versus that of a monolayer. We note that allowing the carbon sheet to fully relax would result in lower energies and thus energies reported herein can be considered DFT upper bounds when compared with bulk energies.

To calculate the effect of the rigid sheet approximation, VASP selective dynamics were used on selected samples to allow the 50 closest carbon atoms to the

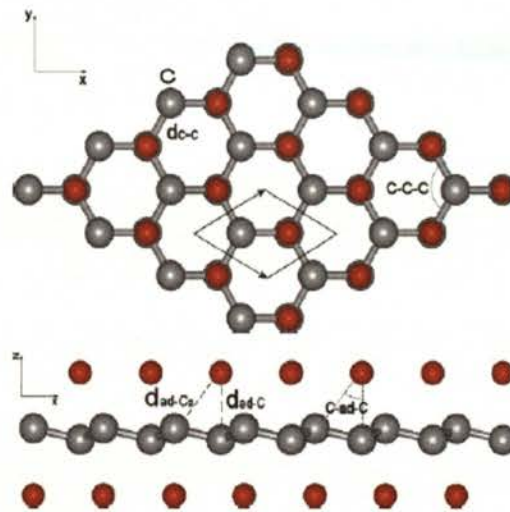


Figure 4.2: Configuration of graphene with fully adsorbed lithium from Medeiros et al.[48] Carbon and lithium atoms are gray and red respectively.

adsorbate to fully relax. In the case of a single boron adsorbate relaxed directly above a carbon atom in the sheet (see Figure 4.3), relaxing the neighboring carbon atoms resulted in calculated C-C bond lengths of 0.146 nm, only 4 pm above unperturbed 0.142 nm of C-C bonds in graphene. The next nearest bond was 0.144 nm and the next after that was back to the unperturbed 0.142 nm (see Figure 4.4). The total relaxation resulted in a total decrease in energy of 115 eV.

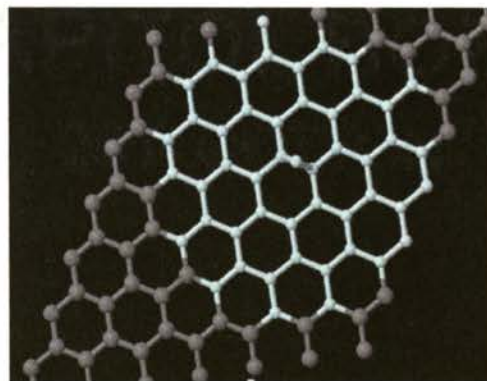


Figure 4.3: Boron adsorbate system in which the 50 nearest atoms (cyan) were allowed to relax in order to estimate the effect of the rigid sheet approximation.

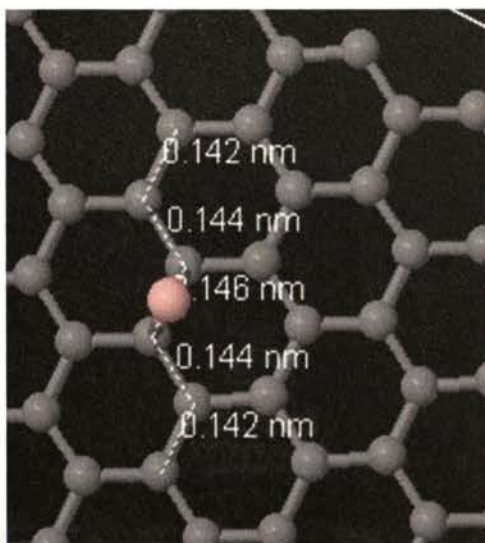


Figure 4.4: Changes in C-C lengths as a result of a boron adsorbate.

4.2.3. Calculations. To isolate size effects, energies were calculated for nano particles of Li, B, LiH, and LiBH₄ for 1, 2, 3 and 4 formula units. The nano-pegs method of Majzoub et al.[39] (see Section 2.7.3) was used to generate geometries for the ionic LiBH₄ and LiH. In this method, designed for ionic compounds, a simplified Hamiltonian involving only electrostatic pair potentials is used to search configuration space for minimum energy configurations using Monte Carlo methods. For the non-ionic lithium and boron particles, multiple configurations were relaxed in DFT and the geometry with the lowest energy was chosen for comparisons in this study.

The adsorption energies were obtained using the following method. First, a single primitive cell of graphene was relaxed. For this step only, the cell size was also allowed to relax until stresses were less than 0.1 Gpa. A z-direction cell length of 16 Å was used to provide a vacuum layer so as to minimize the effects of periodic image interaction. From this relaxed structure, a (7x7x1) supercell was created resulting in a sheet of 98 carbon atoms as seen in Figure 4.5. Calculations are then accomplished by placing adsorbed materials on the sheet at chosen locations and orientations and allowing ions to relax. In the relaxation, the dimensions of the supercell are static,

and only the adsorbed materials are allowed to move within the cell while the carbon atoms are kept fixed. The energy of the adsorbed material E_{ad} is then calculated as follows:

$$E_{ad} = \frac{E_{as} - E_s}{f.u.} \quad (4.3)$$

where E_{as} is the total DFT energy for the adsorbate relaxed onto the sheet, E_s is the total energy of the sheet in isolation, and $f.u.$ is the number of formula units. Preliminary charge density calculations of a single formula unit of LiH or LiBH₄

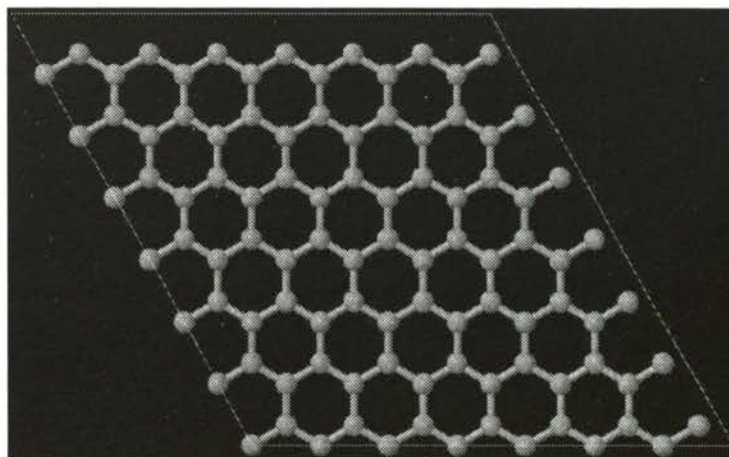


Figure 4.5: Super cell of graphene sheet approximating nano porous material.

revealed very little charge transfer from the complete ionic units to the graphene sheet as can be seen in the charge density plot of Figure 4.6. This suggests that for the case of the ionic compounds on a perfect sheet, long range Van der Waals forces are important which unfortunately, the GGA potential as used in DFT is unable to accurately describe. The VASP package offers the option of including a semi-empirical Van der Waals pair potential following the method of Grimmes [18]. For comparative purposes, many calculations in this effort were performed in duplicate

once with and once without this empirical correction. We will see however, that very little qualitative effect was found beyond a small number of slight variations in the ionic configurations described below.

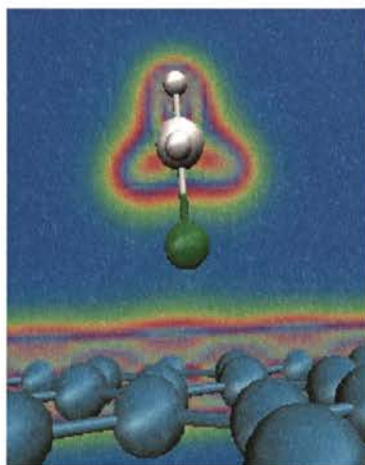


Figure 4.6: Charge density plot of LiBH_4 relaxed onto graphene sheet.

4.3 CONFIGURATION STUDIES

Configurations studies were done to make the best possible guess of the ground state configurations for adsorbed nanoclusters of 1, 2, 3 and 4 formula units of lithium, boron, LiH , and LiBH_4 . This was accomplished by placing the nanoparticles in differing orientations above each of the three sites in graphene: directly above a carbon atom, directly above a hexagon center, and directly above a carbon bond, and allowing the system to relax onto the sheet into a meta-stable configuration. The final lowest energy configurations achieved are those used in the final analysis.

4.3.1. Lithium. The relaxed locations and energies from the lithium configuration are summarized in Figure 4.7. One notes that the lowest energy configuration for a single lithium atom is in the center of a hexagon as is the case for a LiC_6 . Bader


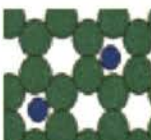
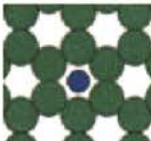



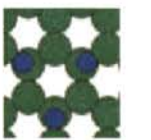
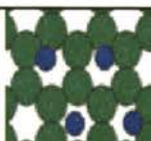



Lithium Configuration Study Wetting Energies (eV)							
1 fu				2fu			
Config	No VdW	VdW	image	config	No VdW	VdW	image
Above Carbon	1.313	1.119		horizontal	1.080	0.828	
Above Hexagon center	1.049	0.826		Li_graphene	1.099	0.944	
Above bond	1.262	1.112		Vertically Stacked	0.995	0.923	
3fu				4fu			
config	No VdW	VdW	Image	config	No VdW	VdW	image
Monolayer	0.839	0.704		monolayer	0.795	0.527	
Stacked	0.714	0.564		Layered	0.795	0.701	
				pyramid	0.686	0.493	

Figure 4.7: Configuration studies for lithium. The ground state energies are highlighted.

analysis[23] indicates 89% charge transfer from the lithium atom to the graphene sheet over which it appears to be evenly distributed. At two formula units, when the lithium atoms are placed on neighboring carbon atoms or even two carbon atoms separated by a common neighbor, the lithium relaxes to a position slightly off center from the carbon atom in opposing directions, a symptom of the fixed carbon lattice not allowing a natural lithium separation distance. Here we see our first difference in ground states when including Grimmes dispersion energies. Without them, the system finds lowest energies when the two lithium atoms are stacked vertically above the sheet. With dispersion included, the system prefers the horizontal layout in which the two atoms are pushed out almost to the hexagon center. Both cases enjoy over an 85 meV difference between their ground states and the states of next lowest energy, strongly demonstrating an example in which including the Van der Waals term results in a different configuration. This is somewhat surprising, since significant charge transfer to the carbon atoms which would suggest trivial dispersion forces. At three formula units, both with and without dispersion forces, a vertical triangle above the sheet is preferred to a horizontal triangular arrangement. The four formula unit systems also finds agreement with both methods preferring a pyramid structure. *From this we can presume that lithium will not absorb as a monolayer on pure graphene, but will instead find a stacking pattern which yields the best energetic compromise between optimal lithium metallic electron delocalization and carbon surface bonding.*

The single lithium atom results agree well with the Valencia study[78] which also finds preferential geometry with the lithium atom on top of the hallow center of the hexagon. That work also has excellent charge density plots that clearly show charge transfer from the lithium s shell to the π bonds closest to the lithium atom as well as some decrease in charge from the sigma bonds of the same atoms. Our bonding energies find good agreement with theirs at gamma within 10 meV and our

2x2x1 calculation is within 20 meV of their 9 k-point system supporting the efficacy of the approximations we have made.

4.3.2.Boron. The results summary of the boron study can be found in Figure 4.8. Contrasting with lithium, a single atom of boron preferred residing directly above a carbon atom consistent with directional p shell bonding instead of over a hexagon center. Switching the boron atom with the carbon atom in the lattice was found to increase the energy by more than 2 eV ruling out the possibility of boron displacing carbon atoms in a perfect sheet. With two boron atoms, two stable configurations were found. In the first, boron atoms are placed on consecutive carbon atoms, and in the second boron is stacked vertically on a carbon atom. Initial configurations of spaced boron atoms on the sheet would relax to a stacked configuration. As was the case for lithium, stacking above the sheet was preferred to layering by 350 meV. At three and four units the preference for conglomerating boron to layering the carbon persisted in triangular and square planar configurations.

4.3.3.Lithium Hydride. Lithium hydride results are summarized in Figure 4.9. A broad configuration study was only completed for one formula unit. Very little charge is transferred from the ionic unit to the sheet suggesting that Van der Waals forces play a critical role. Indeed, as can be seen in the table, without Van der Waals forces being considered, relatively large energetic changes are only found by inverting the ionic unit resulting in a 220 meV preference for the lithium atom facing the sheet while shifting the unit over the carbon from the hexagon center to directly over a carbon atom results in a change of only 21 meV. Including the empirical vdw correction, however, results in the hexagon center being a favorable position by 140 meV. Energies at higher formula units were accomplished by placing nanoparticles from nanopegs[39] onto the sheet with a lithium atom facing the hexagon center. For these number of formula units, the favorable energy state was found to be a planar ring of alternating atoms again with small amounts of surface interaction.








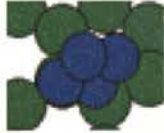
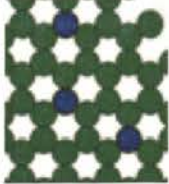

Boron Configuration Study Wetting Energies (eV)							
1 fu				2fu			
Config	No VdW	VdW	image	config	No VdW	VdW	image
On Carbon Bond	6.064	6.233		Vertically Stacked	4.499	4.672	
Above Carbon	6.093	6.242		Above adjacent Carbons	4.670	4.821	
Above Hexagon center	6.123	6.242					
Displacing Carbon	8.424	NC					
3fu				4fu			
config	No VdW	VdW	Image	config	No VdW	VdW	image
Stacked	2.963	3.162		Vertical Square	2.243	2.457	
Spaced	4.819	5.819		Floating square	2.351	2.579	

Figure 4.8: Configuration studies for boron. The ground state energies are highlighted.


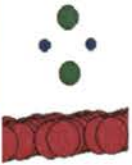
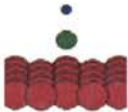
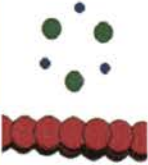
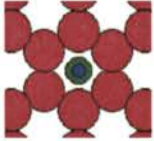
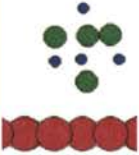
Lithium Hydride Configuration Study Wetting Energies (eV)							
1 fu				Multiple fu			
Config	No VdW	VdW	image	config	No VdW	VdW	image
Hydrogen facing carbon	2.298	2.849		2fu	1.250	1.568	
Lithium facing carbon	2.092	2.426		3fu	0.969	1.358	
Lithium facing carbon, centered on hexagon	2.071	2.287		4fu	0.760	1.020	

Figure 4.9: Configuration studies for lithium hydride. The ground state energies are highlighted.

4.3.4. Lithium Borohydride. The LiBH_4 study was accomplished in a similar fashion to LiH with similar results and negligible charge transfer to the graphene. The results are summarized in Figure 4.10. A configuration with the positive lithium cation facing the sheet favored the inverted configuration by 178 meV and the hexagon center favoring the top of a carbon atom by 15 meV. Nano particles generated from nanopegs[39] were all planar rings similar to that of LiH, and were also the lowest energy structures found when placed on the sheet consistent with a small amount of interaction.

4.4 WETTING ENERGIES

Wetting energies are defined in this work as $E_{ad} - E_{bulk}$ to convey the energy gained or lost from bulk material entering the pores and adsorbing onto the surface. These are plotted in Figure 4.11 for both the case of the empirical vdw potential being included and omitted as well as the results when using a 2x2x1 k-point grid. Also plotted are the energies of the isolated nano particles relative to bulk defined as $E_{nano} - E_{bulk}$ which were calculated without the correction. One first observes that all configurations yield positive wetting energies in contradiction with experiment indicating the model of a pure graphene sheet does not accurately capture the physics. We also note that for all four materials, the wetting curves follow almost identical trends when enabling and disabling the empirical vdw correction. For lithium, the vdw term lowers the wetting energy between 150 and 230 meV and for the other systems, it raises the energy between 150 and 380 meV. While these offsets are somewhat large, including the Grimmes Van der Waals potentials does not appear to add anything qualitatively significant to our analysis. The plot also reveals small differences between the adsorbed and isolated nanoparticles which can be thought of as bonding energies. Lithium shows a lowering of the energy (370 meV/fu at 4 fu),



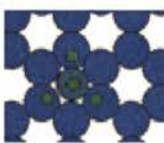
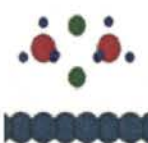
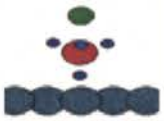
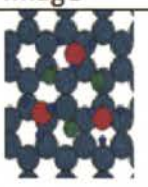
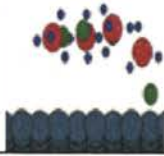
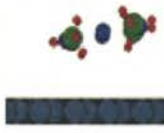
Lithium Borohydride Configuration Study Wetting Energies (eV)							
1 fu				2fu			
Config	No VdW	VdW	image	Config	No VdW	VdW	image
On carbon	1.012	1.185		Sliced from bulk	0.615	0.794	
On center	0.997	1.185		PEGS result	0.451	0.544	
BH ₄ unit facing carbon	2.768	3.099					
3fu				4fu			
config	No VdW	VdW	Image	config	No VdW	VdW	image
PEGS result	0.268	0.506		Relaxed from bulk slice	0.318	0.484	
				PEGS result	0.183	0.412	

Figure 4.10: Configuration studies for lithium borohydride. The ground state energies are highlighted.

consistent with the large amount of charge transferred to the sheet seen in the Bader analysis.[23] Boron, LiH, and LiBH_4 have nearly identical energies when compared to their isolated particles counterparts indicating almost no surface interaction.

Wetting Energies ($E_{\text{ad}} - E_{\text{bulk}}$)

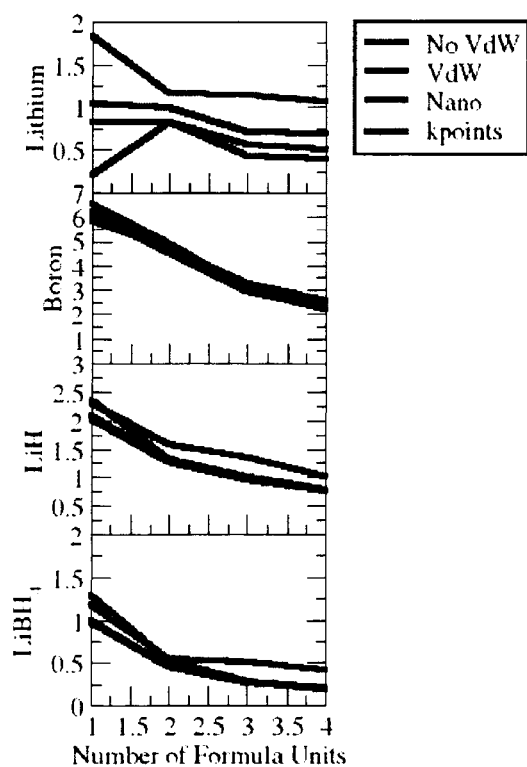


Figure 4.11: Wetting energies of defect free graphene sheet as compared to E_{bulk} .

4.5 VACANCIES

As can be seen in Figure 4.11, none of the compounds involved in LiBH_4 desorption appear to wet a pure defect free sheet of graphene as determined by comparing

E_{ad} with E_{Bulk} . We therefore alter our model to allow for defects in the lattice to more accurately represent the amorphous nature of the carbon which will invariably include defects such as atomic vacancies, grain boundaries for very small graphitic domains, and impurities such as oxygen. Specifically, we introduce a single vacancy by removing a carbon atom from the supercell sheet and allowing the resulting system to relax to an equilibrium configuration as shown in Figure 4.12. To investigate

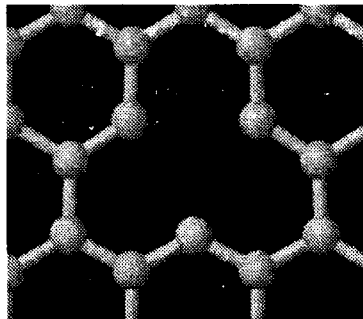


Figure 4.12: Simulated amorphous carbon with a single vacancy.

the effects of defects in the lattice on wetting energies, single formula units of the compounds were placed above the vacancy and allowed to relax while keeping the carbon fixed. Wetting energies are now defined as

$$E_{wv} = E_{bulk} - E_{av} - E_v \quad (4.4)$$

Where E_{wv} is the wetting energy, E_{av} is the DFT energy of the adsorbate in the vacancy, and E_v is the energy of the vacancy defined as the DFT energy of the isolated graphene sheet in which one carbon atom is missing. Figure 4.13 summarizes the resulting configurations and energies. As expected, boron finds a natural place in the lattice participating fully in the sp_2 bonding skeleton yielding a dramatic 6 eV reduction in energy as compared to the boron alpha bulk phase. As can be seen in

Table 4.3, this causes desorption reactions to be strongly downhill which may indicate why a large amount of capacity is immediately lost with respect to bulk as much of the boron is immediately trapped by strong bonding with unsaturated carbon. A lithium

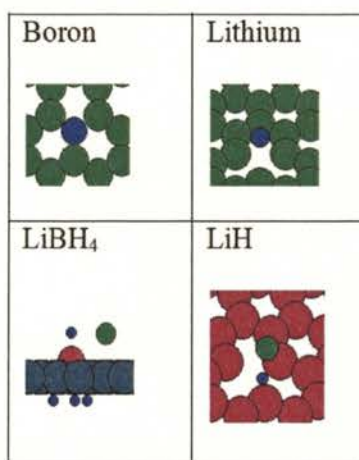


Figure 4.13: Relaxed wetting configuration of species in LiBH₄ desorption on the carbon vacancy.

atom relaxes to a minimum 1.6 Å above the vacancy with roughly the same amount of charge transfer according to Bader analysis but with an energy 1.8 eV lower than on the pure sheet. Lithium hydride is seen to react strongly with the vacancy by way of the hydrogen atom disassociating and bonding to the one of the border carbons lowering the energy by 2.86 eV, achieving a strong wetting of 2.07 eV. LiBH₄ achieved the weakest wetting energy of only 0.86 eV as result of simple relaxation whereby two hydrogen atoms disassociated from the unit to bond with dangling carbon bonds in the vacancy. This configuration still leaves two H atoms bonded to the boron atom perhaps explaining the B-H stretching and bending modes observed by Liu et al. in FTIR measurements[35] without necessarily requiring LiBH₄ to exist in the carbons at all. An even lower energy can be obtained by manually moving a third hydrogen atom to the vacancy achieving a wetting energy of 1.48 eV with a single

hydrogen atom remaining attached to the boron atom although this configuration may be kinetically suspect as it was not achieved by a strict relaxation. VASP linear response[15] was used to calculate phonon energies for the B-H bonds and are listed in Table 4.1 in which rough agreement can be seen with the FTIR result. One would suppose that if this configuration indeed occurs, it would disappear permanently after the first dehydrogenation, in which, in the absence of hydrogen, the boron atom would take full occupancy of the vacancy.

Table 4.1: B-H stretching and bending mode frequencies calculated at gamma by VASP linear response for bulk and various configurations of BH_4 in the vacancy.

System	Bending(cm^{-1})	Stretching(cm^{-1})
Experimental Bulk LiBH_4 [17]	1090-1099	2157-2177
Experimental LiBH_4 in Carbon[35]	1100	2200-2300
DFT Bulk LiBH_4	1066-1304	2348-2439
DFT BH_4 in vacancy with 1 H on boron	1056	2149
DFT BH_4 in vacancy with 2 H on boron	1037,1243	2027,2211

A unit of diborane was also placed on the vacancy and was seen not to interact (all H atoms remaining intact on the gas molecule) suggesting that the suppression in B_2H_6 release is not caused by direct adsorption of the complete gas unit into the carbon framework. It is more likely due to boron reacting strongly with carbon defects as the molecule traverses the carbon pores causing it to decompose into carbon bonded boron and H_2 gas. This is also consistent with the experimental result that diborane is seen at larger particle sizes (4 nm and 6 nm) in which there is less surface interaction. This unfortunately would suggest that the lack of B_2H_6 does not indicate any active material being saved, but simply more boron being trapped in carbon vacancies. Experiments in which hydrogen cycling is repeated several times could

test this hypothesis. If after repeated cycling, B_2H_6 reappears, it would indicate that the vacancies have saturated, thus denying this mechanism to diborane suppression. Continued diborane suppression might suggest that it is instead a result of some catalytic effect of the surface interactions or a change in reaction pathways due to the small particle sizes.

4.6 MAGNESIUM HYDRIDE WETTING

As a further validation of our model we compare the calculated wetting energies of $LiBH_4$, which easily wets the carbon in experiments[35], with that of MgH_2 , which does not, and requires either a wetting layer precursor of Ni or Cu nanoparticles[19], or else initial adsorption of $MgBu_2$ which reacts to form methane and MgH_2 . [54] A single unit of MgH_2 was placed above the vacancy with two initial positions and was allowed to relax onto the vacancy. In the first initial configuration, the two hydrogen atoms faced the vacancy, and the system relaxed such that the two hydrogen atoms disassociated from the magnesium and bonded to the carbon, and the magnesium atoms retreated to an isolated distance 3.3 Å from the sheet. With an initial configuration of the Mg atoms facing the vacancy, the Mg atom bonded with the dangling bonds and the two H atoms formed an independent molecule of H_2 . Both configurations resulted in energies higher than a single formula unit of MgH_2 in the bulk agreeing with observations that MgH_2 does not naturally wet pure carbons. The same calculation was done for a single Mg atom which also showed positive wetting energies, again agreeing with difficulties seen in infiltrating magnesium metal.

4.7 BORON DOPED GRAPHENE SHEETS

Placing the single formula unit nanoparticles directly above the trapped boron atoms was also attempted to evaluate whether the effective boron doping might also

have a wetting effect. The resulting wetting energies can be seen in Table 4.2. While a single hydrogen atom will bond with the doped boron, adding a second hydrogen atom and allowing the system to relax, will cause both of them to separate from the sheet and form an H_2 molecule. This result suggests that the trapped boron atoms can act as catalytic centers for hydrogen desorption, perhaps improving kinetics, and explaining in part the lowered observed desorption temperatures.

Table 4.2: Wetting energies of various compounds for 1 fu adsorbate on both a perfect graphene sheet and one with a single vacancy. Note the positive energies for all compounds on the perfect sheet showing the need for vacancies to account for wetting. Also note the positive wetting energy of MgH_2 on the vacancy which is experimentally observed not to wet nano-porous carbons.

Adsorbate	Wetting of perfect slab $E_{ad} - E_{bulk}(eV)$	Wetting of vacancy $E_{uv}(eV)$	Wetting of boron dopant $E_{BD} - E_{Bulk}(eV)$	Wetting of B-L surface $E_{BL} - E_{Bulk}(eV)$
$LiBH_4$	0.9799	-0.858	0.897	1fu: -0.515 4fu: -1.035
LiH	2.0714	-0.785	1.658	0.161
Lithium	1.0493	-0.753	-1.126	0.556
Boron	6.0644	-5.799	3.605	4.653
MgH_2	2.1714	0.762	-	-
Mg	1.43	0.611	-	-

Given the energetics, it can be imagined that after hydrogen cycling, most of the vacancies are filled with boron atoms. The results of Table 4.2 for $LiBH_4$ indicate that in this state we once again lose $LiBH_4$ wetting. However, since lithium does exhibit considerable wetting energies on the boron doped surface, we can consider a new surface in which lithium atoms are wetted to the boron dopants. Calculating DFT results for $LiBH_4$ placed on this new surface (Figure 4.14) results in a wetting

energy of -0.52 eV compared to bulk. When this calculation is performed with the four formula unit particle as the adsorbate, a wetting energy of -1.04 eV is the result which accounts for the LiBH_4 remaining in the pores after multiple hydrogenation cycles even after vacancies have been filled. LiBH_4 particles strongly anchored to the surface in this manner may also be a source of lattice strain that destroys the local order, tending to amorphize the LiBH_4 . If indeed lithium anchoring is the key to wetting, then another lithium insertion site studied by Mochida et al.[51] that exists on the surfaces of graphite clusters perpendicular to the hexagonal plane may also be responsible for wetting. As these sites are shown to have energies lower than in LiC_6 , it is possible that at higher temperatures and larger nanocluster sizes of lithium, the boron atom is not even necessary.

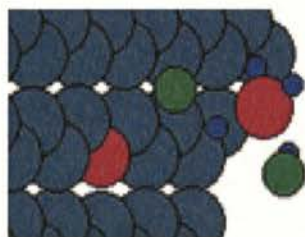


Figure 4.14: LiBH_4 on a boron dopant which has been wetted with lithium.

4.8 COMPARISON OF SURFACE EFFECTS WITH SIZE EFFECTS

With the calculated results from our improved defect model described above, we calculate the energies of the LiBH_4 desorption reactions. The results are summarized in Table 4.3 and plotted in Figure 4.15. One can clearly see that reactions involving the vacancies have become strongly downhill to the extent that one would

expect these reactions to take place immediately upon infiltration. The reaction energies of the isolated nanoparticles are strongly uphill and become more so as particle size is decreased suggesting that size effects alone would in fact cause much higher desorption temperatures. This can be understood as being due to the product metal nanoparticles being of high energy as the delocalization of their conduction electrons is significantly limited. Majzoub et al.[39] found similar results calculating reaction energies of NaAlH_4 nanoclusters. The exception is the desorption of LiH which shows a trend of decreasing reaction energy with decreasing particle size. Wagemans et al.[79] finds a similar trend with MgH_2 particles suggesting that perhaps it is only the hydrides with complex anions whose enthalpies worsen with decreased cluster size. These calculations strongly suggest, therefore, that lower desorption temperatures observed are a result of interaction with the amorphous carbon and not the nanoconfinement. The plots of Figure 4.15 nonetheless show that the interaction with the surface has an overall effect of decreasing desorption energies as compared with the isolated nano-cluster systems. There is some question as to whether the dehydrogenated state of the adsorbate is that of reaction 1 in Table 4.3 ($\text{LiH} + \text{B}$) or reaction 2 ($\text{Li} + \text{B}$). The column for reaction 3 shows the energy differences between the two states. The interaction we see of lithium with all of the surfaces including pure graphene (see Figure 4.11) relative to the other phases including LiH suggest more likelihood that lithium metal is the dominant product, making reaction 2 the favored pathway. In fact, it appears both size effects and carbon interaction work in favor of lithium being the reaction product of choice. In the proximity of a boron dopant atom where lithium is the only wetter, the energetic case is even stronger.

Table 4.3: Reaction energies per molecule H_2 released for four reactions calculated on different surfaces. To show the change in reaction pathways between a product of LiH and metal lithium, the lower energies for each surface are in bold face.

Reaction	Reaction 1 $LiB_4 \rightarrow$ $LiH + B + \frac{3}{2}H_2$	Reaction 1 $LiB_4 \rightarrow$ $Li + B + 2H_2$	Reaction 3 $LiH \rightarrow$ $Li + \frac{1}{2}$	Reaction 4 $H \text{ in vac } \rightarrow$ H_2
Bulk	0.73	0.99	1.76	NA
Vacancy 1fu	-3.09	-1.86	1.82	0.88
Boron Dopant 1fu	3.64	1.78	-3.80	NA
Li-B surface 1fu	4.29	3.85	2.55	NA
carbon 1fu	5.5	4.05	-0.28	NA
carbon 2fu	4.26	3.51	1.25	NA
carbon 3fu	3.18	2.70	1.26	NA
carbon 4fu	2.61	2.36	1.62	NA
Nano 1fu	5.82	4.53	0.68	NA
Nano 2fu	4.54	3.76	1.4	NA
Nano 3fu	3.25	2.94	2.01	NA
Nano 4fu	2.71	2.61	2.29	NA

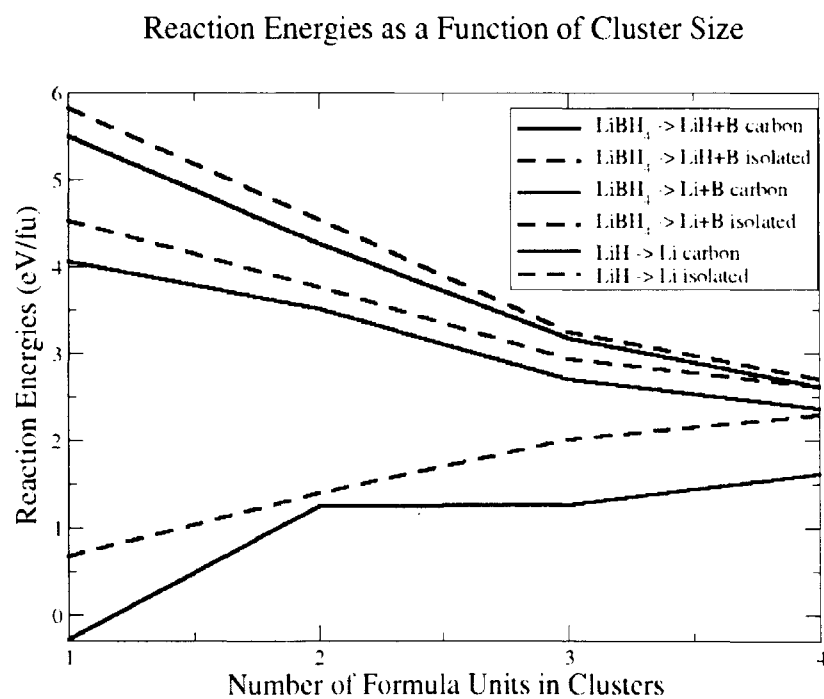


Figure 4.15: Plot of desorption energies for the three reaction pathways considered.

4.9 CONCLUSION

Roughly modeling amorphous carbon with DFT using a graphene sheet successfully reproduces several experimental results if one also introduces vacancies in the graphene without which even simple wetting cannot not be explained. We propose a stable wetting mechanism for LiBH_4 in which the BH_4 anions are bonded to ionic lithium which has transferred its charge to a boron dopant on the surface. We suggest that the amorphous nature of the nanoconfined LiBH_4 could be a result of strong surface interaction with boron atoms that have been trapped by pre-existing vacancies in the carbon. We suggest that diborane gas reduction is also due to boron trapping and that lithium is the more likely reactant instead of LiH as seen in the bulk. This change in reaction pathway may be another explanation for the lack of observed B_2H_6 for all surface environments proposed. The energies of reactions are increased as compared to bulk suggesting that the lower desorption temperatures must be kinetic in nature via a catalytic effect that remains unknown.

5 CONCLUSIONS

The first-principles studies detailed in this thesis, using the density functional theory framework, have resulted in several interesting theoretical finds for the thermodynamics of the studied energy storage systems. We hope that the insights made from these calculations may in a small way add to the understanding of the materials on which there is currently a great deal of interest as potential energy storage applications of the future.

In the first, we pursued the largely unexplored possibilities of using metal hydrides for lithium-ion batteries. Having started with the method developed by Ackbarzadeh et al.[3] to determine phase diagrams of hydrogen storage reactions, and adapting the grand canonical ensemble such that the electrochemical potential of the lithium ions is varied instead of the H_2 chemical potential, we have calculated the thermodynamic viability of metal hydrides in the Li-Mg-B-N-H system as lithium-ion battery anodes at 300 K. To eliminate mixtures that are most obviously irreversible, reactions that involve gas evolution were precluded. The result is 12 new candidate chemistries that have theoretical capacities between 2 and 10 times that of a today's commonly used graphite anode. Furthermore, the expansions in volume of these chemistries are all relatively mild(between 43% and 95%) when compared to that of silicon(400%) which is thought to be an important quantity to minimize for achieving good cyclability. In comparison with an experiment performed to charge cycle $Li_4BN_3H_{10}$, we find excellent agreement in terms of the capacity predicted for each plateau when extracting lithium from the material. When pushing lithium into the material, the lengths of the plateaus were predicted to be much larger than was found by experiment suggesting that there are significant kinetic barriers to forming the relevant imides, amides, nitrides and boronitrides. We recommend experiments to charge cycle the predicted 12 material mixtures to observe their actual performance.

This method of searching stoichiometry space for interesting reactions is completely transferable to other chemical systems assuming energies can be calculated for a reasonably large phase space of the candidate compounds in the system.

DFT was also used to perform surface calculations that roughly model hydrogen desorption LiBH_4 confined to nanosizes by nanoporous carbon scaffolding. An amorphous carbon environment was approximately modeled as a sheet of graphene with a single carbon atom missing from the lattice. Nanoparticles of adsorbate LiBH_4 of varying particle size were placed upon the vacancy and allowed to relax. The resulting total energies were used to calculate wetting strengths as well as desorption energies of the material in the carbon environment. We predict that lithium atoms will strongly wet vacancy sites that have become occupied by boron atoms, and that these electron depleted lithium atoms can act as anchoring sites to LiBH_4 as they attract BH_4 units, thus explaining how LiBH_4 easily wets nanoporous carbons in experiment. This strong interaction with the carbon surface also provides a possible explanation for why the compound becomes amorphous at very small pore sizes.

The large negative wetting energies of boron in the vacancy also supports a possible mechanism responsible for the lack of observed diborane gas (B_2H_6). We propose that as diborane molecules traverse the carbon, they encounter vacancies at which they instantly decompose into trapped boron and hydrogen gas. This theory can be tested by repeated hydrogen cycling to see if vacancy saturation can be achieved at which point B_2H_6 would be expected to reappear. The calculated reaction enthalpies seem to favor lithium as a product of desorption instead of LiH , which is favored in decomposition of bulk LiBH_4 . Such a change in the reaction pathway due to the surface offers another possible explanation for the lack of diborane gas. Calculated energies for the adsorbate product and reactant phases, and also for the isolated nanoparticles exhibit a trend of increasing reaction energies with decreased particle sizes. This suggests that the thermodynamics of the system are made considerably

worse by the small size, although slightly improved by the surface interaction. This leads one to conclude that the lower observed desorption temperatures are a result of improved kinetics provided by either size effects, or a catalytic source on the surface. We show that when we introduce an additional hydrogen atom to a hydrogen atom bound to a trapped boron atom, the two will leave the surface together to form a molecule of H_2 upon relaxation. It is therefore proposed that the boron dopant may be a source of the catalysis.

APPENDIX A.

COMPUTATIONAL SCRIPTS

SHIFT ATOMS

The Shift_atoms script can be used to translate and rotate specified atoms within a POSCAR file. The script takes nine consecutive arguments described below to perform the transformation.

- 1) Specifies the POSCAR file
- 2) Specifies the beginning atom of the atoms to be specified
- 3) Specifies the Final atom of the atoms to be specified
- 4) Translate X
- 5) Translate Y
- 6) Translate Z
- 7) Rotate around X axis
- 8) Rotate around Y axis
- 9) Rotate around Z axis

shift_atoms.sh

```

1  #!/bin/sh
   #shift and rotate selected atoms on a POSCAR in cartesian coordinates
   #use as "shift_atoms poscar_of_choice atom_start atom_end x_shift
       y_shift z_shift

   Pre_POSCAR=$1
6  atom_start=$2
   atom_end=$3
   shift_x=$4
   shift_y=$5
   shift_z=$6
11 rot_x=$7
   rot_y=$8
   rot_z=$9

   if [ -z "$1" ]

```

```

16 then
echo "usage: shift_atom POSCAR atom_start atom_end shift_x shift_y
      shift_z rot_x rot_y rot_z (rot is optional) "
exit
fi

21 #format POSCAR
fix_poscar $Pre_POSCAR > tmp_poscar
POSCAR=tmp_poscar

# get inverse lattice vectors
26 POS_inverse_lat_vectors $POSCAR > tmp_inverse
#convert to XYZ and move to origin
fix_poscar $POSCAR | awk -f ~/awkfiles/POStoXYZ.awk | tail -n +3 >
      tmp_xyz_all

#cut out atoms to be moved
31 sed -n ${atom_start}.${atom_end}p tmp_xyz_all > tmp_xyz_init
#find first atom's distance to origin
R1=`sed -n 1p tmp_xyz_init | awk '{ print $2 }'`
R2=`sed -n 1p tmp_xyz_init | awk '{ print $3 }'`
R3=`sed -n 1p tmp_xyz_init | awk '{ print $4 }'`

36 # rotate structure. Theta is in degrees. euler script requires an
      angle and a rotation axis so this is done for each cart axis

if [ $rot_x -ne 0 ] || [ $rot_y -ne 0 ] || [ $rot_z -ne 0 ]
then
41 #move unit to origen
awk -v R1=$R1 -v R2=$R2 -v R3=$R3 ' {printf(" %5.16f %5.16f %5.16f \n"
      . ($2-R1) . ($3-R2) . ($4-R3)) } ' tmp_xyz_init > tmp_origen
awk -v theta_deg=$rot_x -v Ux=1 -v Uy=0 -v Uz=0 -f /U1/masont/awkfiles/
      euler_rotate.awk tmp_origen > tmp_rotated_x
awk -v theta_deg=$rot_y -v Ux=0 -v Uy=1 -v Uz=0 -f /U1/masont/awkfiles/
      euler_rotate.awk tmp_rotated_x > tmp_rotated_y
awk -v theta_deg=$rot_z -v Ux=0 -v Uy=0 -v Uz=1 -f /U1/masont/awkfiles/
      euler_rotate.awk tmp_rotated_y > tmp_rotated

46 #shift back from origen
awk -v R1=$R1 -v R2=$R2 -v R3=$R3 ' {printf(" %5.16f %5.16f %5.16f \n"
      . ($1+R1) . ($2+R2) . ($3+R3)) } ' tmp_rotated > tmp_pre_shift
else
awk ' {print $2 " " $3 " " $4 } ' tmp_xyz_init > tmp_pre_shift
fi

51 #shift structure in angstroms
awk -v S1=$shift_x -v S2=$shift_y -v S3=$shift_z ' {printf(" %5.16f
      %5.16f %5.16f \n" . ($1+S1) . ($2+S2) . ($3+S3)) } ' tmp_pre_shift
      > tmp_shifted

#####
56 ##### convert XYZ back to POSCAR in frame of host material ###

invX1=`sed -n 1p tmp_inverse | awk '{ print $1 }'`
invY1=`sed -n 2p tmp_inverse | awk '{ print $1 }'`

```

```

61 invZ1='sed -n 3p tmp_inverse | awk ' { print $1 } ' '
invX2='sed -n 1p tmp_inverse | awk ' { print $2 } ' '
invY2='sed -n 2p tmp_inverse | awk ' { print $2 } ' '
invZ2='sed -n 3p tmp_inverse | awk ' { print $2 } ' '

66 invX3='sed -n 1p tmp_inverse | awk ' { print $3 } ' '
invY3='sed -n 2p tmp_inverse | awk ' { print $3 } ' '
invZ3='sed -n 3p tmp_inverse | awk ' { print $3 } ' '

71 awk -v invX1=$invX1 -v invX2=$invX2 -v invX3=$invX3 \
-v invY1=$invY1 -v invY2=$invY2 -v invY3=$invY3 \
-v invZ1=$invZ1 -v invZ2=$invZ2 -v invZ3=$invZ3 \
' { printf(" %1.16f %1.16f %1.16f T T T\n". (invX1*$1 + invY1*$2 +
invZ1*$3) , (invX2*$1 + invY2*$2 + invZ2*$3) , (invX3*$1 + invY3
*$2 + invZ3*$3)) } ' tmp_shifted > tmp_atoms

# forming POSCAR
76 # prepend all of poscar up to atom_start
awk -v start=$atom_start ' NR < (start+7) ' $POSCAR
# insert shifted_rotated atoms
cat tmp_atoms
#insert rest of POSCAR
81 awk -v end=$atom_end ' NR > (end+7) ' $POSCAR

rm -rf tmp_*
#rm -rf tmp_rotat*
#rm -rf tmp_shifted
86 #rm -rf tmp_xyz
#rm -rf tmp_atoms
#rm -rf tmp_inverse

```

CALCULATE INVERSE LATTICE VECTORS

This script reads a POSCAR file and outputs the inverse lattice vectors.

POS_inverse_lat_vectors.sh

```

#!/bin/bash
2 ##### find inverse of POSCAR lattice vector matrix #####
fix_poscar $1 | head -5 | tail -3 > tmp_lat_vectors
7 awk ' {x[NR]=$1; y[NR]=$2 ; z[NR]=$3 } ; \
END {   print "format long"
        printf("a = [ %2.16f . %2.16f . %2.16f  ;\n", x[1],y[1],z[1] )
        printf("      %2.16f . %2.16f , %2.16f  ;\n", x[2],y[2],z[2] )
        printf("      %2.16f . %2.16f , %2.16f] ;\n", x[3],y[3],z[3] )
12      print " a^-1 "      } ' tmp_lat_vectors > tmp.m

octave -q < tmp.m | tail -4 | head -3

rm -rf tmp_lat_vectors
17 rm -rf tmp.m

```

REHOST STRUCTURE TO A NEW UNIT CELL

POS_rehost.sh transforms the coordinates of a structure in a POSCAR file, referenced by the -P option, to the coordinate system of a different unit cell defined by the POSCAR file referenced by -V option. This is useful for taking gas molecules that are defined in a box, and placing them onto crystal system (e.g. the carbon sheet of section 4).

POS_rehost.sh

```
#!/bin/sh
#rehost POSCAR atoms to lattice vectors of a different POSCAR
3 #either declare a vector poscar onto which you wish to rehost the
  structure or set the box size

box_size=0

declare SWITCH
8 while getopts "V:P:B:" SWITCH; do
  case $SWITCH in
    V) VECTOR_POSCAR=$OPTARG ;;
    P) POSCAR=$OPTARG ;;
    B) box_size=$OPTARG ;;
13  esac
done

if [[ $box_size -eq "0" ]]; then
if [[ -z $VECTOR_POSCAR ]]; then
18 echo "please POSCAR with new lat vectors < -V POSCAR > or else Enter
  box size with -B option" | tee /dev/tty
  exit
fi
fi
if [[ -z $POSCAR ]]; then
23 echo "please include POSCAR to be rehosted with < -P POSCAR >" | tee
  /dev/tty
  exit
fi
#fix_poscar $nakedsheet | head -7
atom_types=`fix_poscar $POSCAR | sed -n '1p' | awk '{ for(i=2;i<=NF;i
  ++){print $i} }'
28 atom_count=`fix_poscar $POSCAR | sed -n '6p'

if [[ $box_size -eq "0" ]] ; then
POS_inverse_lat_vectors $VECTOR_POSCAR > tmp_inverse
fix_poscar $VECTOR_POSCAR | head -5 | tail -3 > tmp_lat_vectors
33 else
inv_box_size=`echo " scale = 5; 1/$box_size " | bc`
cat > tmp_inverse <<EOF
```

```

$inv_box_size 0      0
0      $inv_box_size 0
38 0      0      $inv_box_size
EOF
cat > tmp_lat_vectors <<EOF
$box_size 0      0
0      $box_size 0
43 0      0      $box_size
EOF
fi

#convert to XYZ and move to origin
48 fix_poscar $POSCAR | awk -f ~/awkfiles/POStoXYZ.awk | tail -n +3 >
    tmp_xyz_init
#find first atom's distance to origin
B1=`sed -n 1p tmp_xyz_init | awk '{ print $2 }`
B2=`sed -n 1p tmp_xyz_init | awk '{ print $3 }`
B3=`sed -n 1p tmp_xyz_init | awk '{ print $4 }`
53 #move unit to origin
awk -v B1=$B1 -v B2=$B2 -v B3=$B3 '{printf(" %5.16f %5.16f %5.16f \
n". ($2-B1) . ($3-B2) . ($4-B3)) }' tmp_xyz_init > tmp_origen
#shift structure to center
#awk -v B1=$2 -v B2=$3 -v B3=$4 '{printf(" %5.16f %5.16f %5.16f \n
". ($1+B1) . ($2+B2) . ($3+B3)) }' tmp_rotated > tmp_shifted
# start forming POSCAR
58 echo "Z:" $atom_types
#fix_poscar $VECTOR_POSCAR | head -5 | tail -n 4
echo "1.000"
cat tmp_lat_vectors
echo $atom_count
63 echo "Direct"

##### convert XYZ back to POSCAR in frame of host material and shift
to center of unit cell ###
invX1=`sed -n 1p tmp_inverse | awk '{ print $1 }'`
invY1=`sed -n 2p tmp_inverse | awk '{ print $1 }'`
68 invZ1=`sed -n 3p tmp_inverse | awk '{ print $1 }'`
invX2=`sed -n 1p tmp_inverse | awk '{ print $2 }'`
invY2=`sed -n 2p tmp_inverse | awk '{ print $2 }'`
invZ2=`sed -n 3p tmp_inverse | awk '{ print $2 }'`
invX3=`sed -n 1p tmp_inverse | awk '{ print $3 }'`
73 invY3=`sed -n 2p tmp_inverse | awk '{ print $3 }'`
invZ3=`sed -n 3p tmp_inverse | awk '{ print $3 }'`

awk -v invX1=$invX1 -v invX2=$invX2 -v invX3=$invX3 \
-v invY1=$invY1 -v invY2=$invY2 -v invY3=$invY3 \
78 -v invZ1=$invZ1 -v invZ2=$invZ2 -v invZ3=$invZ3 \
'{printf(" %1.8f %1.8f %1.8f \n ". (invX1*$1 + invY1*$2 + invZ1*$3 +
0.5) . (invX2*$1 + invY2*$2 + invZ2*$3 + 0.5) . (invX3*$1 + invY3*
$2 + invZ3*$3 + 0.5)) }' tmp_origen > tmp_atoms

cat tmp_atoms
rm -rf tmp.*

```


FIX POSCAR

POSCAR files come with a slight variety in format. Fix_poscar.sh reads a POSCAR file and reformats it to a form usable by the scripts in this work.

fix_poscar.sh

```

### removes the POSCAR line with alpha atomic names and removes
selective dynamics line
### works both when the POSCAR is the first argument and when it's
piped in
3
if [ -z $1 ]
then
awk ' { if(NR == 6 && $1 !~ /[0-9]/) { } else {print;} } ' | sed '/
Selective/d'
else
8 test=`head -6 $1 | tail -1 | awk ' {print $1} ' | tr -d 0-9`
if [ -z "$test" ] ; then
cat $1
else
sed -e '6d' $1
13 fi | sed '/Selective/d'
fi

```

CALCULATE FREE ENERGY

This awk script reads an OUTCAR file and produces energies as a function of finite temperature using the method described in section 2.30.

free_energy.awk

```

1 BEGIN {hbar=6.582e-16;K=8.617e-5;icount=0}
   #first line skips over imaginary frequencies second line does not.
   { if ($2 == "f" && $6 > 0.001 ) {w[FNR]=$6*1e12 ;skip[FNR]=0 } else {w[
     FNR]=0;skip[FNR]=1;icount+=1 } }
6 END {
   for(T=10; T <= Tmax; T=T+inc){
     tot_energy = 0
11  for(i=1; i <= NR; i++)
     {
       if (skip[i]==0) {
         energy[i] = hbar*w[i]/2 + (K*T)*log(1-exp(-hbar*w[i]/(K*T)))
         tot_energy+=energy[i]
16  }
     }
   print T " " tot_energy/fu
   }
}

```

CONVERT POSCAR TO CIF

The crystal structure visualization program JMOL reads the CIF format but does not read POSCAR files. The POStoCIF.awk script is used to convert crystal structures from the VASP POSCAR format to the CIF format.

POStoCIF.awk

```

BEGIN { }

function crossi(a1,a2,a3,b1,b2,b3){
return (a2*b3 - a3*b2)
5 }
function crossk(a1,a2,a3,b1,b2,b3){
return (a3*b1 - a1*b3)
}
function crossj(a1,a2,a3,b1,b2,b3){
10 return (a1*b2 - a2*b1)
}
function normcross(a1,a2,a3,b1,b2,b3){
return sqrt( (a2*b3 - a3*b2)^2 + (a3*b1 - a1*b3)^2 + (a1*b2 - a2*b1)^2
)
}
15 }

function get_Z( ELMT ) {
if ( ELMT== 1 ) return "H" ;
if ( ELMT== 2 ) return "He" ;
if ( ELMT== 3 ) return "Li" ;
20 if ( ELMT== 4 ) return "Be" ;
if ( ELMT== 5 ) return "B" ;
if ( ELMT== 6 ) return "C" ;
if ( ELMT== 7 ) return "N" ;
if ( ELMT== 8 ) return "O" ;
25 if ( ELMT== 9 ) return "F" ;
if ( ELMT== 10 ) return "Ne" ;
if ( ELMT== 11 ) return "Na" ;
if ( ELMT== 12 ) return "Mg" ;
if ( ELMT== 13 ) return "Al" ;
30 if ( ELMT== 14 ) return "Si" ;
if ( ELMT== 15 ) return "P" ;
if ( ELMT== 16 ) return "S" ;
if ( ELMT== 17 ) return "Cl" ;
if ( ELMT== 18 ) return "Ar" ;
35 if ( ELMT== 19 ) return "K" ;
if ( ELMT== 20 ) return "Ca" ;
}

/Z:/ {
40 #check for repeated atom types and do not repeat them
for(i=0; i < 400; i++) {have[i] = 0}
ntype_print=0

```

```

    for(i=0; i < NF-1; i++) {
        atom_type[i]=$ (i+2)
45         if (have[atom_type[i]] != 1)
                {
                    have[atom_type[i]] = 1
                    ntype_print++
                }
50     }

    ntype = NF-1
}
#read all else in as whole record
/1.0/ {
55  getline
    for(j=0;j<3;j++){
        for(i=0;i<3;i++){lat_vector[i,j]=$ (i+1)}
        getline
    }
60

#check for vasp.5.2 element characters and skip line

if ( $1==$1+0 ) {} else {getline}

65 # gather atom quantities
    for(i=0;i<ntype;i++){type_count[i]=$ (i+1)};
# find number of atoms
    for(i=0;i<ntype;i++){natom = natom + type_count[i]}
getline
70
if ( /electi/ ) {getline}
getline

#get atom positions for each atom type one type at a time
75 for(i=0;i<ntype;i++){
    for(j=0;j<type_count[i];j++){
        for(k=0;k<3;k++){
            atom_pos[i,j,k]= $(k+1)
        }
80         getline
    }
}

}
END {
85
### print total number of atoms

print "data_global"

90 ## figure out a b c

pi=3.141592654

a = sqrt(lat_vector[0.0]^2 + lat_vector[1.0]^2 + lat_vector[2.0]^2)
95 b = sqrt(lat_vector[0.1]^2 + lat_vector[1.1]^2 + lat_vector[2.1]^2)
c = sqrt(lat_vector[0.2]^2 + lat_vector[1.2]^2 + lat_vector[2.2]^2)

```

```

abdot = (lat_vector[0.0]*lat_vector[0.1] + lat_vector[1.0]*lat_vector
[1.1] + lat_vector[2.0]*lat_vector[2.1])
gamma = (180/pi)*atan2(normcross(lat_vector[0.0].lat_vector[1.0].
lat_vector[2.0].lat_vector[0.1].lat_vector[1.1].lat_vector[2.1]).
abdot)
100
acdot = (lat_vector[0.0]*lat_vector[0.2] + lat_vector[1.0]*lat_vector
[1.2] + lat_vector[2.0]*lat_vector[2.2])
beta = (180/pi)*atan2(normcross(lat_vector[0.0].lat_vector[1.0].
lat_vector[2.0].lat_vector[0.2].lat_vector[1.2].lat_vector[2.2]).
acdot)

bcdot = (lat_vector[0.1]*lat_vector[0.2] + lat_vector[1.1]*lat_vector
[1.2] + lat_vector[2.1]*lat_vector[2.2])
105 alpha = (180/pi)*atan2(normcross(lat_vector[0.1].lat_vector[1.1].
lat_vector[2.1].lat_vector[0.2].lat_vector[1.2].lat_vector[2.2]).
bcdot)

print "_cell_length_a " a
print "_cell_length_b " b
print "_cell_length_c " c
110 print "_cell_angle_alpha " alpha
print "_cell_angle_beta " beta
print "_cell_angle_gamma " gamma
print " "
print "loop_"
115 print "_atom_site_label"
print "_atom_site_fract_x"
print "_atom_site_fract_y"
print "_atom_site_fract_z"
print " "
120 ##### iterate through each atom#####
    for (i=0;i<ntype;i++){
        for (j=0;j<type_count[i];j++){
            #####
            x_pos = lat_vector[0.0]*atom_pos[i.j.0] + lat_vector[0.1]*atom_pos[
i.j.1] + lat_vector[0.2]*atom_pos[i.j.2]
125 y_pos = lat_vector[1.0]*atom_pos[i.j.0] + lat_vector[1.1]*atom_pos[
i.j.1] + lat_vector[1.2]*atom_pos[i.j.2]
            z_pos = lat_vector[2.0]*atom_pos[i.j.0] + lat_vector[2.1]*atom_pos[
i.j.1] + lat_vector[2.2]*atom_pos[i.j.2]

printf("%2s%1s %1.4f %1.4f %1.4f \n", get_Z(atom_type[i]).j+1.
atom_pos[i.j.0].atom_pos[i.j.1].atom_pos[i.j.2])
        }
130 }
}

```

CONVERT POSCAR TO CARTESIAN

POStoXYZ converts structure files from the POSCAR file to the XYZ format which can be used for JMOL inputs and is commonly used in this work as an intermediate coordinate system for converting between formats.

POStoXYZ.awk

```

BEGIN { }

function get_Z( ELMT ) {
4  if ( ELMT== 1 )    return "H";
  if ( ELMT== 2 )    return "He";
  if ( ELMT== 3 )    return "Li";
  if ( ELMT== 4 )    return "Be";
  if ( ELMT== 5 )    return "B";
9  if ( ELMT== 6 )    return "C";
  if ( ELMT== 7 )    return "N";
  if ( ELMT== 8 )    return "O";
  if ( ELMT== 9 )    return "F";
  if ( ELMT== 10 )   return "Ne";
14 if ( ELMT== 11 )   return "Na";
  if ( ELMT== 12 )   return "Mg";
  if ( ELMT== 13 )   return "Al";
  if ( ELMT== 14 )   return "Si";
  if ( ELMT== 15 )   return "P";
19 if ( ELMT== 16 )   return "S";
  if ( ELMT== 17 )   return "Cl";
  if ( ELMT== 18 )   return "Ar";
  if ( ELMT== 19 )   return "K";
  if ( ELMT== 20 )   return "Ca";
24 }

/Z:/ {
  #check for repeated atom types and do not repeat them
  for(i=0; i < 200; i++) {have[i] = 0}
29  ntype_print=0
  for(i=0; i < NF-1; i++) {
    atom_type[i]=$ (i+2)
    if (have[atom_type[i]] != 1)
34         {
            have[atom_type[i]] = 1
            ntype_print++
        }
  }

  ntype = NF-1
39 }
#read all else in as whole record
/1.0/ {
  getline
  for (j=0;j<3;j++){

```

```

44     for (i=0;i<3;i++){ lat_vector [ i , j]=$(i+1)}
        getline
        }
        for (i=0;i<ntype; i++){ type_count [ i]=$(i+1)};
# find number of atoms
49     for (i=0;i<ntype; i++){ natom = natom + type_count [ i]}
        getline
        getline

        #get atom positions for each atom type one type at a time
54     for (i=0;i<ntype; i++){

        for (j=0;j<type_count [ i ]; j++){
            for (k=0;k<3;k++){

59                 atom_pos [ i . j . k]= $(k+1)

            }

            getline
        }

64     }

    }

END {

69     ### print total number of atoms
    print natom
    print "XYZ file"

    # compare each atom with others in the unit cell
74     ##### iterate through each atom#####
        for (i=0;i<ntype; i++){
            for (j=0;j<type_count [ i ]; j++){

#####

79         x_pos_l = lat_vector [0.0]*atom_pos [ i . j . 0] + lat_vector [0.1]*
            atom_pos [ i . j . 1] + lat_vector [0.2]*atom_pos [ i . j . 2] + shiftx
            y_pos_l = lat_vector [1.0]*atom_pos [ i . j . 0] + lat_vector [1.1]*
            atom_pos [ i . j . 1] + lat_vector [1.2]*atom_pos [ i . j . 2] + shifty
            z_pos_l = lat_vector [2.0]*atom_pos [ i . j . 0] + lat_vector [2.1]*
            atom_pos [ i . j . 1] + lat_vector [2.2]*atom_pos [ i . j . 2] + shiftz

84         #####euler matrix is as follows
        ## Cos(alpha)*Cos(beta) - Cos(beta)Sin(alpha)Sin(gamma) # Cos(gamma)
            )Sin(alpha) + Cos(alpha)Cos(beta)Sin(gamma) # Sin(beta)Sin(gamma)
        ## -Cos(beta)Cos(gamma)Sin(alpha) - Cos(alpha)Sin(gamma) # Cos(alpha)
            )Cos(beta)Cos(gamma) - Sin(alpha)Sin(gamma) # Cos(gamma)Sin(beta)
        ## Sin(alpha)Sin(beta) # -Cos(
            alpha)Sin(beta) # Cos(beta)

89     #####

    pi = 3.14159265

```

```

alpha = alpha_deg*(pi/180)
beta = beta_deg*(pi/180)
94 gamma = gamma_deg*(pi/180)

R11 = cos(alpha)*cos(beta) - cos(beta)*sin(alpha)*sin(gamma)
R12 = cos(gamma)*sin(alpha) + cos(alpha)*cos(beta)*sin(gamma)
R13 = sin(beta)*sin(gamma)
99
R21 = -cos(beta)*cos(gamma)*sin(alpha) - cos(alpha)*sin(gamma)
R22 = cos(alpha)*cos(beta)*cos(gamma) - sin(alpha)*sin(gamma)
R23 = cos(gamma)*sin(beta)

104 R31 = sin(alpha)*sin(beta)
R32 = -cos(alpha)*sin(beta)
R33 = cos(beta)

x_pos = x_pos_l*R11 + y_pos_l*R12 + z_pos_l*R13
109 y_pos = x_pos_l*R21 + y_pos_l*R22 + z_pos_l*R23
z_pos = x_pos_l*R31 + y_pos_l*R32 + z_pos_l*R33

printf("%2s %1.16f %1.16f %1.16f \n", get_Z(atom_type[i]), x_pos,
      y_pos, z_pos)
114 #####
      }
}
#####
      }

```


GENERATE SUPERCELLS

This script generates supercells from primitive unit cells. It requires the definition of the variables `amax`, `bmax`, and `cmax` which determine the dimensions of the supercell in each lattice direction in terms of the number of repeating primitive cells.

POS_super.awk

```

BEGIN { cell_mult=amax*bmax*cmax;}

3 /Z:/ {
    #check for repeated atom types and do not repeat them
    for(i=0; i < 200; i++) {have[i] = 0}
    ntype_print=0
    ntype=NF-1
8    for(i=0; i < NF-1; i++) {
        atom_type[i]=$(i+2)
        if (have[atom_type[i]] != 1)
            {
13                have[atom_type[i]] = 1
                ntype_print++
            }
        }
    ntype = NF-1
    }
18 #read all else in us whole record
    /1.0/ {
        getline
        for(j=0;j<3;j++){
            for(i=0;i<3;i++){lat_vector[i.j]=$(i+1)}
23        getline
            }
        for(i=0;i<ntype;i++){type_count[i]=$(i+1)};
        # find number of atoms
        for(i=0;i<ntype;i++){natom = natom + type_count[i]}
28    getline
        getline

        #get atom positions for each atom type one type at a time
        for(i=0;i<ntype;i++){
33            for(j=0;j<type_count[i];j++){
                for(k=0;k<3;k++){
                    atom_pos[i.j.k]= $(k+1)
                    }
38            getline
                }
            }
        }
    }

```

```

END {
43  ## print POSCAR heading
    printf("Z: ")
        for (i=0; i<ntype; i++) { printf("%d ", atom_type[i])}

48  ## print lattice vectors adjusted for new supercell
    printf(" \n1.0\n")

        printf("      %3.8f %3.8f %3.8f\n", lat_vector[0,0]*amax,
            lat_vector[1,0]*amax, lat_vector[2,0]*amax)
        printf("      %3.8f %3.8f %3.8f\n", lat_vector[0,1]*bmax,
            lat_vector[1,1]*bmax, lat_vector[2,1]*bmax)
53  printf("      %3.8f %3.8f %3.8f\n", lat_vector[0,2]*cmax,
            lat_vector[1,2]*cmax, lat_vector[2,2]*cmax)

    ##### print atom ordering/count #####
        for (i=0; i<ntype; i++)
            {
58             printf("%d ", type_count[i]*cell_mult)
            }

        printf(" \nDirect\n")

63  ##### iterate through each atom#####
        for (i=0; i<ntype; i++){
            for (j=0; j<type_count[i]; j++){

        ##### the loop again for plus one lattice vector
68         for (a=0; a<amax; a++) {
            for (b=0; b<bmax; b++) {
                for (c=0; c<cmax; c++) {
                    #####

73  ###distuce = lattice vector #####for supercell generation, this will
        create new atom
            a_pos_s = atom_pos[i,j,0]+a
            b_pos_s = atom_pos[i,j,1]+b
            c_pos_s = atom_pos[i,j,2]+c
            printf("      %3.8f %3.8f %3.8f\n", a_pos_s/amax, b_pos_s/bmax, c_pos_s/
                cmax)
78         }}}}
        printf(" \n~")
    }
}
#####

```

LINEAR PROGRAMMING FOR LITHIUM ION BATTERIES

This Octave script is used to perform the phase diagram calculations of chapter 3. It is controlled by the data.dat file described in section 5.

lithium_lp_v7.m

```

# Lithium_lp.m version 6
#
3 #
# find reaction equations for Lithium ion reactions using VASP inputs
#
# version 2 12/02/09 this version sets LB to go negative and sets
# all mass constants to 0.
8 #
# the intention is to be able to find any
# reaction when any free energies relations change
# it also constrains the lithium count isntead of
# letting it run free.
# version 3 12/06/09 this version reverts back to setting mass
# constants appropriately and goes through tie lines
# in ternary phase diagram
# version 4 12/10/09 prints out tieline results into a format
# sortable by reaction type
13 # version 5 12/26/09 reformats data table for vectors reading in as
# columns. got rid of entering
# in "num_phases", added anode/cathode selection and "use or don't use
# " option to eliminate unwanted phases.
# version 6 01/24/11 cleaned up outputs
# T. Mason
# UM-St. Louis
18 # 26 Dec 2009
#
# run with $ octave -qf fname.m | less
#
#
23 # constants
global k_B = 1.38e-23; # in joules/K
global eVtoJ = 1.602e-19;
global JtoHart=2.293710449e+17;
global Avogadro=6.022e23
28 global M_Proton_kg = 1.6737e-27;
global M_H2_kg = 2*M_Proton_kg;
global M_Li_kg = 6.941*1e-3/Avogadro
global H_bar = 1.05457e-34; # J*s
# ideal gas constant hydrogen
33 global R_H2 = 4124; #(J/kg K)
###hydrogen zero point eV
global H_zero = 0.81874;
#variables
global num_phases;
38 global num_atoms;

```

```

global constrain_chem_element;
global tieline;
global tieline_steps;
global Li_static_energy;
43 global phase;
global static_free_energy;
global niLi;
global a;
global b_pre;
48 global start;
global stop;
global b_type
global b;
global electrode;
53 global var;
global const_var;
global const_var_value;
global var_init;
global var_end;
58 global steps;
global increment;
global printall;
global print_comp_map;
global print_quant;
63 global debug;
global Li_temp;
global Li_Vib_j;
global Li_valid;
global f_vib_J;
68 global spec_heat;
global EnergyVib;
global volume;
global valid;
#printall=1
73 maxfu=5;
printcnt=1;
printmax=9;
printflag=0;

78
### read file
#global directory = `C:/users/tim/Documents/umsl/research_majzoub/
linear_programming/LiFePO4/`
global myfile = fopen("data.dat"."r");
readinputs
83 #printinputs

if ! strcmp(const_var, "T") & ! strcmp(const_var, "P") & ! strcmp(
const_var, "C")
printf("\nerror: please specify pressure(P) or temp(T) as constant
variable\n\n");
endif

88
#####settings for GLPK function#####

```

```

# set bounds on atom constraints (F=free)
for i= 1:num_atoms
ctype(i) = "S";
93 endfor

if strcmp(constrain_chem_element, "no")
    ctype(1) = "F";
endif
98

# inteter (I) or continuous (C) soluions
for i= 1:num_phases
    vartype(i) = "C";
103    ub(i) = 200;
    lb_pre(i) = 0;    # lower bound of variables
endfor
lb=lb_pre `;
#ub = [];
108

# lower bounds of variables.
#lb = ( 0*(1:num_phases) - maxfu ) `;
# upper bounds of variables.
#ub = ( 0*(1:num_phases) + maxfu ) `;
113

s = 1;    # maximization (-1) or minimzation (1)
param.msglev = 0;
#param.itlim = 1000;

118 #####
#printf("Gibbs = XmgH2 * ( F(MGH2) - 0.5* U_H2 * 2 )    +    Xmg * (F(mg)
    - 0)\n");

#####calculation#####
if strcmp(const_var, "T")
123 printf("Temperature is %8.2f\n\n",const_var_value);
elseif strcmp(const_var, "P")
printf("Pressure is %8.2f\n\n",const_var_value);
else
printf("Chemical potential only\n\n");
128 endif

#this outer loop varies the compositions from one end of a tie line to
    the other with the
#endpoints spelled out in the input data sheet

133 if strcmp(tieline, "yes")
    num_tl_steps = tieline_steps;
elseif strcmp(tieline, "no")
    num_tl_steps = 0;
else
138 printf("error. please enter yes or no for tieline option\n");
    exit
endif

```

```

total_consts = sum(b_pre);
143 #for tl_step = 0:num_tl_steps

    tie_count=1;
    loop_length(1)=0;
    loop_length(2)=0;
148 loop_length(3)=0;
    loop_length(4)=0;
    loop_length(5)=0;
    for j = 1:num_atoms
        if strcmp(b_type{j}, "tie")
153 tie(j)=tie_count;
            loop_length(tie_count)=num_tl_steps;
            tie_count++;
        endif
    endfor
158 tie_count--;

    for x(1)=0:loop_length(1)
        for x(2)=0:loop_length(2)
            for x(3)=0:loop_length(3)
163 for x(4)=0:loop_length(4)
                for x(5)=0:loop_length(5)

                    for j = 1:num_atoms
                        if strcmp(b_type{j}, "tie")
168 b_pre(j)=start(j) + (x(tie(j))/num_tl_steps)*(stop(j)-
                            start(j));
                        elseif strcmp(b_type{j}, "const")
                            else
                                printf("\nplease select const, start, or end for each
                                    element\n");
                                exit;
173 endif
                            endfor
                            b=b_pre `;

#####
178 #then begins internal loop within a given composition
#####

rxncount=0;
steps = (var_end - var_init)/increment;
183 for i = 0: steps
    var = var_init + i*increment;

    if strcmp(const_var, "T")
        T_RT = const_var_value;
188 else
        T_RT = var;
    endif

    if strcmp(const_var, "T")
193 P = var;

```

```

else
P = const_var_value;
endif
198 kT_eV = k_B*T_RT/eVtoJ;

##quant con = (Mt/2pi(H_bar^2))^3/2    mass = 2 * atomic mass of H
nq = (M_Li_kg*kT_eV*eVtoJ/(2*pi*(H_bar^2)))^(3/2);

203 ##### set Lithium energy #####
    if Li_valid == 1
        Li_vib = interp1(Li_temp, Li_Vib_J, T_RT)*JtoHart/Avogadro;
    else
        Li_vib = 0;
208 endif;
    # Free energy = E_tot - T*S = static free energy - E_vib
    Li_energy = Li_static_energy + Li_vib;

#####
213 ### set free energies for the constant temperature #####
    for j = 1:num_phases
        if valid(j) == 1
            f_vib(j) = interp1(temp(j,:), f_vib_j(j,:), T_RT)*JtoHart/Avogadro;
        else
218         f_vib(j) = 0;
        endif;
        f(j) = static_free_energy(j) + f_vib(j);
    endfor
#####
223

### chem energy = element total energy + chem potential formula

    if strcmp(const_var, "C")
228     mu = var_init + i*increment;
    else
        mu = kT_eV * log(P*1e3/(k_B*T_RT*nq)) + Li_energy; # - H_zero :
    endif

233 c0 = (mu) * niLi;
    g = (f + c0)';
    c = g;
    h = c0;

238 if i != 0
        lastxmin=xmin;
    endif

    [xmin, fmin, status, extra]=glpk(c,a,b,lb,ub,ctype,vartype,s,param);
243 x_i(i+1,:) = xmin;
    fmin_i(i+1) = fmin;

##### print initial distribution ##
    if i == 0

```

```

248 # print composition
      lastxmin = xmin;
      if strcmp(print_comp_map,"yes")
        printf("\ncomposition: ");
        for i=1:num_atoms
253         printf(" %2.2f", b_pre(i));
        endfor
      endif

      printf("\nInitial: ");
258      vol_initial=0;
      for n= 1:num_phases
        if abs(xmin(n)) > 0.00001 && strcmp(electrode{n},"anode
          ")
          printf("%1.2f %-10.10s",xmin(n), phase{n});
          vol_initial=vol_initial+volume(n)*xmin(n);
263          printcnt = printcnt + 1;
        endif
      endfor
      #printf("\n"):
    endif
268 ##### print final distribution ##

      if (i == steps)
# print composition
273
        printf("\nFinal: ");
        final_Li=0;
        vol=0;
        for n= 1:num_phases
278          if abs(xmin(n)) > 0.00001 && strcmp(electrode{n},"anode
            ") && !strcmp(phase{n},"Li_a")
            printf("%1.2f %-10.10s",xmin(n), phase{n});
            final_Li=final_Li + xmin(n)*a(1,n);
            vol=vol+volume(n)*xmin(n);
            printcnt = printcnt + 1;
283          endif
        endfor
        printf("Li_in %4.2f ", final_Li);
        printf("Vol_increase %3.2f ", 100*(vol-vol_initial)/
          vol_initial);
        endif
288 #####print results#####

      # check to see if there has been a reaction
      for n= 1:num_phases
293        if i != 0
          if abs(xmin(n) - lastxmin(n)) > 0.001
            printflag=1;
          endif
        endif
298      endfor

```



```

if ( abs(fmin) > 1e-20 & printflag==1)
rxncount=rxncount+1;
303     if !strcmp(print_comp_map,"yes")
printf("\n#####\n");
printf("# Reaction # %d\n",rxncount);
if strcmp(const_var, "T")
    printf("# Pressure %10.2f. mu %10.2e. fmin %10.2e\n".
308     P.mu.fmin);
elseif strcmp(const_var, "P")
    printf("# Temperature:%10.2f. mu %4.4e. fmin %10.2e\n"
    ".T_RT.mu.fmin);
elseif strcmp(const_var, "C")
    printf("# Chem Potential: mu %4.4e. fmin %10.2e\n".mu.
    fmin);
endif
313 endif

## calculate and print the difference table
if i != 0
for n= 1:num_phases
318     diff(n) = xmin(n) - lastxmin(n);
if debug == 1
    printf("%12.5f ".diff(n));
    printcnt = printcnt + 1;
    if printcnt == printmax
323         printcnt = 1;
        printf("\n");
    endif
    endif
    endfor
328 endif

## Print the LHS of reaction
#printf("\n");
333 printcnt=1;

for print_comp=0:0 # print once with and once WO
    amounts
    printf("\n");
    for n= 1:num_phases
338
if diff(n) < -0.001 && strcmp(electrode{n},"anode")
    if print_comp==1
        printf("%-4s ". phase(n));
    else
343        printf("%1.2f %-4s ".-diff(n).phase{n});
    endif
    printcnt = printcnt + 1;
endif
348 if printcnt == printmax

```

```

    printent = 1;
    printf("\n");
endif
    353     endfor
        ## Print RHS of reaction
        printf("=>");
        printf(" "); printent=1;

    358     for n= 1:num_phases
        #count Lithium transferred
        if diff(n) < 0.001 && strcmp(phase{n},"Li_c")
            Li.in = -diff(n);
        endif;

    363     if diff(n) > 0.001 && strcmp(electrode{n},"anode")
        #if strcmp(print_comp,"1")
        if print_comp==1
            printf("%-4s ", phase(n));
    368         else
            printf("%1.2f %-4s ".diff(n),phase{n});
        endif

        printent = printent + 1;
    373     endif

    if printent == printmax
        printent = 1;
        printf("\n");
    378     endif

        endfor
        endfor
        #printf("\n\n");
        printent=1;

    383     # print composition
        vol=0;
        for n= 1:num_phases
            if abs(xmin(n)) > 0.00001 && strcmp(electrode{n},"anode")
                vol=vol+volume(n)*xmin(n);
    388         endif
        endfor
        if strcmp(print_comp_map,"yes")
            printf("V = %4.2f Li.in %1.1f Vol.increase %2.2f",-mu.
                Li.in . 100*(vol-vol_initial)/vol_initial);
    393     endif

endif
printflag=0;
endfor

398 if rxncount != 0 & !strcmp(print_comp_map,"yes") # print composition if
    reactions found
    printf("composition: ");

```

```

for i=1:num_atoms
    printf(" %2.2f", b_pre(i));
endfor
403 printf("\n\n@@@@@@@@@@@@@@@@@@@@@@@@@@@@@@@@@@@@\n");
    printf("end for this composition\n");
    printf("@@@@@@@@@@@@@@@@@@@@@@@@@@@@@@@@@@@@\n\n\n\n\n\n");
##### print initial distribution ##
    if i == 0
408     printf("awefwfewf\n");
            for n= 1:num_phases
                if abs(xmin(n)) > 0.00001
                    printf("%-10.20s  %12.5f \n", phase{n}. xmin
                        (n));
                    printcnt = printcnt + 1;
413                 endif
            endfor
        printf("\n");
    endif
418
endif

423 #####Print in more compact form
    if debug == 1
        printf("#####\n\n\n");
        if strcmp(const_var, "T")
428 printf("Pres  ");
        elseif strcmp(const_var, "P")
            printf("Temp  ");
        elseif strcmp(const_var, "C")
            printf("Chem  ");
433        endif

        for j = 1:num_phases
438     printf("%-15s ", phase{j});
        endfor
        printf("\n");

        for i = 0: steps
443     printf("%-4.2f ", var_init + i*increment);

            for j = 1:num_phases
                printf("%-4.2f ", x_i(i+1,j));
            endfor
448 printf(" Fmin = %-5.4f \n", fmin_i(i+1));
        endfor
    endif
    printf("\n");
#endfor

```

```
453 endfor
    endfor
    endfor
    endfor
    endfor### end of tie line loop
458 printf("\n");
#####

exit

463 ##### report WARNING if free energy files are missing###
    if strcmp(printall, "yes")
        printf("\n\n");
        for i=1:num_phases
            if valid(i)==0
468             printf("WARNING Missing free energy file for %10s\n", phase{i});
            endif
        endfor

        if Li_valid==0
473         printf("WARNING Missing free energy file for Lithium");
        endif
    endif
#####
```

READ INPUTS SCRIPT

Called by lithium_lp-v7.m, this octave routine reads the data.dat file, and extracts the relevant linear programming inputs.

readinputs.m

```

# readinputs function for linear programming version 5
2 # this function reads the input data file

function [] = readinputs
7

global myfile
global directory
global pre;
12 global num_phases;
global num_atoms;
global constrain_chem_element;
global tieline;
global tieline_steps;
17 global phase;
global Li_static_energy;
global static_free_energy;
global niLi;
global a;
22 global b_pre;
global start;
global stop;
global b_type;
global b;
27 global electrode;
global N_H_ratio;
global const_var;
global const_var_value;
global var_init;
32 global var_end;
global increment;
global printall;
global print_comp_map;
global print_quant;
37 global debug;
global Li_temp;
global Li_Vib_j;
global Li_valid;
global f_vib_J;
42 global spec_heat;
global EnergyVib;
global volume;
global valid;

```

```

47 # read header
   skip = fscanf(myfile, "%s" .1);

   # read whether to constrain chemical potential element
52 skip = fscanf(myfile, "%s" .1);
   constrain_chem_element = fscanf(myfile, "%s" .1);

   # read whether this is a tie line calculation and read tieline steps
   skip = fscanf(myfile, "%s" .1);
57 tieline = fscanf(myfile, "%s" .1);

   skip = fscanf(myfile, "%s" .1);
   tieline_steps = fscanf(myfile, "%d" .1);

62 # read in static energy of free particle.
   skip = fscanf(myfile, "%s" .3);
   Li_static_energy = fscanf(myfile, "%f" .1);

67 #read in phase name free energy and a matrix component for each phase
   skip = fscanf(myfile, "%s" .5);

   num_atoms=-1;
72 num_phases=0;
   end_atoms="start";
   end_phases="start";
   while !strcmp(end_atoms, "end")
       end_atoms = fscanf(myfile, "%s" .1);
77   num_atoms += 1;
   endwhile

   i=1;
   while !strcmp(end_phases, "end")
82   phase{i}=fscanf(myfile, "%s" .1);
       if !strcmp(phase{i}, "end")
           electrode{i}=fscanf(myfile, "%s" .1);
           use_phase = fscanf(myfile, "%d" .1);
           static_free_energy(i) = fscanf(myfile, "%f" .1);
87   volume(i)= fscanf(myfile, "%f" .1);
           for j=1:num_atoms
               a(j,i)=fscanf(myfile, "%f" .1);
           endfor
           if use_phase == 1
92   num_phases += 1;
               i += 1;
           endif
       else
           end_phases = "end";
97   if use_phase == 0 # delete last row if use phase was zero to give
           matrix correct dimensions
               a(:, num_phases+1) = [];

```

```

    endif
  endif
endwhile
102 # read in phase Lithium atom counts (niH) Li should always be first
    atom type in input file
    #skip = fscanf(myfile,"%s".1);
    #for i= 1:num_phases
    # niLi(i) = fscanf(myfile,"%d".1);
107 #endfor

    #construct niLi such that only anode materials contribute
    for i=1:num_phases
    if strcmp(electrode{i}."cathode")
112 niLi(i) = a(1,i);
    elseif strcmp(electrode{i}."anode")
    niLi(i) = 0;
    else
    printf("\n please enter cathode or anode for electrode value\n");
117 exit
    endif
    endfor

122 # read in mass conservation constants
    skip = fscanf(myfile,"%s".2);
    for i=1:num_atoms
    skip = fscanf(myfile,"%s".1);
    b_type{i}=fscanf(myfile,"%s".1);
127 if strcmp(b_type{i}."const")
    b_pre(i)=fscanf(myfile,"%f".1);
    else
    start(i)=fscanf(myfile,"%f".1);
    stop(i)=fscanf(myfile,"%f".1);
132 endif
    endfor

    # read in whether temp or Press constant
    skip = fscanf(myfile,"%s".1);
137 const_var =fscanf(myfile,"%s".1);

    # read in constant variable value
    skip = fscanf(myfile,"%s".1);
    const_var_value =fscanf(myfile,"%f".1);
142

    # read in variable intial value
    skip = fscanf(myfile,"%s".1);
    var_init =fscanf(myfile,"%f".1);

147 #read in variable end value
    skip = fscanf(myfile,"%s".1);
    var_end =fscanf(myfile,"%f".1);

    #read in variable increment

```

```

152 skip = fscanf(myfile,"%s",.1);
    increment =fscanf(myfile,"%f",.1);

    #read in variable printall
    skip = fscanf(myfile,"%s",.1);
157 printall =fscanf(myfile,"%s",.1);

    #read in variable print_comp_map
    skip = fscanf(myfile,"%s",.1);
    print_comp_map =fscanf(myfile,"%s",.1);
162

    #read in variable print_quant
    #skip = fscanf(myfile,"%s",.1);
    #print_quant = fscanf(myfile,"%s",.1);

167 #read in variable debug
    skip = fscanf(myfile,"%s",.1);
    debug =fscanf(myfile,"%d",.1);

    fclose(myfile);
172

    ##### read in Li entropy related energies***
    myfile = fopen([directory,'Li_plus.dat'],'r');
    Li_valid = 1;
177 if myfile != -1
        inc = 1;
        dat = 0;
        while (dat != -1)
            dat = fgetl(myfile);
182         if (dat != -1)

            # this reads in the energies in units of J/mol-c
            [Li_temp(inc) Li_Vib_J(inc)] = sscanf(dat, "%f %f", "C");
            inc++;
187         endif;
        endwhile
        fclose(myfile);
    else
        Li_valid=0;
192 endif;
    #####

    ##### read vibrational energy tables
    *****
    # read in data if it exists or else sets file validity bit to zero
197 for i= 1:num_phases
        valid(i) = 1;
    endfor
    ##### read phase i
    #for i= 1:(list_size)
202 for i=1:num_phases
        myfile = fopen([phase{i}.'.dat'],'r');
        if (myfile != -1)

```



```
207  ### !(strcmp (file_list(i).name , "data.dat"))
      #comp{i}=strtrunc(file_list(i).name,length(file_list(i).name)-4):
      inc = 1;
      dat = 0;
      while (dat != -1)
        dat = fgetl(myfile);
        if (dat != -1)
212    # this reads in the energies in units of J/mol-c
        [temp(i,inc) f_vib_J(i,inc) spec_heat(i,inc) EnergyVib(i,inc)] =
          sscanf(dat, "%f %f %f %f", "C");
        #printf("f-vib-j of phase %5s = %10f\n", phase{i} . f_vib_J(i,inc)):
        inc++;
        endif;
217    endwhile
      fclose(myfile);
      else
        valid(i)=0;
        endif;
222    endfor
```

SAMPLE DATA SHEET

The data.dat file contains all of the inputs for linear programming. It must be prepared in exactly the format as shown in the sample. The variables **free_element** and **tie-line-calculation** should always be set to “yes” as is done in the sample. The variable **tieline-steps** determines the resolution of a tie-line calculation. In these calculations, linear programming runs repeatedly as the stoichiometry is varied between initial and final values indicated in the **mass_conservation_constants** table. If more than one element is set to “tie”, then calculations are run over a multi-dimensional stoichiometric space. Up to 5 elements can be varied. **Tie-line_steps** determines the number of calculations to be run between the initial and final values for each element.

The data table contains all of the phases, each with the following attributes.

Electrode = whether the phase is to be considered in the anode or the cathode.

Use = allows the user to disable the phase by setting to “0”.

Free_energy = the calculated total energy for the compound.

Volume = volume per unit cell in Å³. Linear programming will output the change in volume.

atomic count = the number of each constituent atom in each compound.

The stoichiometry table listed under the words “Mass_conservation_constants” define the desired stoichiometry for the calculation. The second column determines whether the quantity of this element is to be varied for a tie-line calculation. A setting of “const” will hold the quantity constant to the value in column 3. For any other value, column 3 and column 4 determine the initial and final value of the quantity for the tie-line calculation

Constant_variable should be set to “C”, **Constant_variable_value** is ignored but some value must be present. **variable_start**, **variable_end**, and **variable_incr** determine the initial voltage of the cell, the final voltage, and the increment that it is increased for each linear programming minimization respectively.

data.dat

```

1 #Lithium_in_first_column_1
  free_element: yes
  tie-line_calculation: yes
  tieline_steps: 20

6 Lithium static Energy -0.002612913

  phases      electrode use?  Free_energy(ev/fu) volume  Li Mg  B  N  H
  end
H2            anode     1    -3.298640.0           0      0 0  0  0  1
N2            anode     1   -8.3259935000        0.0     0 0  0  1  0
11 Li_a        anode     1   -1.8909667200        20.40    1 0  0  0  0
  Li_c        cathode    1   -1.8909667200         0.0     1 0  0  0  0
Mg            anode     1   -1.5390698000        22.87    0 1  0  0  0
B             anode     1   -6.5634110000         7.25    0 0  1  0  0
NH3           anode     1  -18.7763580000        0.0     0 0  0  1  3
16 B2H6        anode     1  -32.7179300000        0.0     0 0  2  0  6
  LiH         anode     1   -5.9874650000        16.07    1 0  0  0  1
  LiNH2        anode     1  -18.5174670000        32.72    1 0  0  1  2
  Li2NH         anode     1  -17.2606080000        34.12    2 0  0  1  1
  Li4NH         anode     1  -21.4763140000        58.53    4 0  0  1  1
21 Li4BN3H10   anode     1  -79.0055800000       149.93    4 0  1  3  10
  Li3B2NH8     anode     1  -60.3526800000       123.58    3 0  1  2  8
  Li2BNH6      anode     1  -41.8936800000        92.15    2 0  1  1  6
  Li3N         anode     1  -15.5053530000        44.52    3 0  0  1  0
  LiN3         anode     1  -27.2512560000        45.24    1 0  0  3  0
26 LiBH4        anode     1  -23.3192300000        53.25    1 0  1  0  4
  Li2Mg(NH)2   anode     1  -32.4696880000        64.50    2 1  0  2  2
  Li2Mg2(NH)3  anode     1  -46.7387100000        91.04    2 2  0  3  3
  Li4Mg(NH)3   anode     1  -49.7090000000        93.63    4 1  0  3  3
  Li3BN2       anode     1  -33.9815440000        56.97    3 0  1  2  0
31 Mg3N2        anode     1  -25.2899230000        62.34    0 3  0  2  0
  LiMgH3       anode     1  -14.5534810000        47.05    1 1  0  0  3
  Mg(NH2)2     anode     1  -34.4643300000        72.04    0 1  0  2  4
  end

36 Mass_conservation_constants

  Li    const 200
  Mg    const 10
  B     const 13
41 N    const 3
  H     const 60

  Contant_variable(T(K)_or_P(KPa):  C
  Const_variable_value(K_or_KPa):    101.325
46 variable_start: -10
  variable_end: 0
  variable_incr: .1
  printall: yes
  print_comp_map: yes
51 debug: 0

```

APPENDIX B.

PERMISSIONS FOR FIGURES

Permission from Dr. Alireza Akbarzadeh for Figure 2.4

Hi Tim,

no problem from my side! congratulations! are you writing your dissertation, that is great, good luck, Ali

Permission from Dr. Candace Chan for Figure 3.1

Hi Tim,

6 Yes, you may use the TEM image as long as you cite the journal publication wherein you borrow the image.

Best, Candace

Permission from Dr. Chris Marianetti for Figures 2.2 and 2.3

Dear Tim, I do not see any problem at all assuming the reference is provided. I am glad that the work has been of use to you. Sincerely,

chris

BIBLIOGRAPHY

- [1] P. Adelhelm, K. de Jong, and P. de Jongh. How intimate contact with nanoporous carbon benefits the reversible hydrogen desorption from NaH and NaAlH₄. *Chemical Communications*, pages 6261–6263, 2009.
- [2] US Energy Information Administration. Alternatives to traditional transportation fuels 2009, 2011. Accessed 3/3/2011.
- [3] Alireza R. Akbarzadeh, Vidvuds Ozolin, and Christopher Wolverton. First-principles determination of multicomponent hydride phase diagrams: Application to the li-mg-n-h system. *Advanced Materials*, 19:3233–3239, 2007.
- [4] Anders Andreasen. Predicting formation enthalpies of metal hydrides. Technical report, Ris National Laboratory, 2004.
- [5] Antonino Salvatore Arico, Peter Bruce, and Bruno Scrosati et al. Nanostructure materials for advanced energy conversion and storage devices. *Nature Materials*, 4:366–377, 2005.
- [6] Stefano Baroni, Stefano de Gironcoli, and Andrea Dal Corso. Phonons and related crystal properties from density-functional perturbation theory. *Rev. Mod. Phys.*, 73:515–562, 2001.
- [7] P.E. Blochl. Projector augmented-wave method. *Physical Review B*, 50(24):17953–17979, 1994.
- [8] P.E. Blochl. Projector augmented-wave method. *Physical Review B*, 50:17953–17979, 1994.
- [9] P.E. Blochl, Clemens J Forst, and Johannes Schimpl. Projector augmented wave method: ab initio molecular dynamics with full wave functions. *Bull. Mater. Sci.*, 26(1):33–41, 2003.
- [10] Borislav Bogdanovic, R. Brand, A. Marjanovic, M. Schwickardia, and J. Tolle. Metal-doped sodium aluminium hydrides as potential new hydrogen storage materials. *Journal of Alloys and Compounds*, 302:36–58, 2000.
- [11] Borislav Bogdanovic and Manfred Schwickardi. Ti-doped alkali metal aluminum hydrides as potential novel reversible hydrogen storage materials. *Journal of Alloys and Compounds*, 298:1–9, 1997.

- [12] Candace K. Chan and Halim Peng et al. High-performance lithium battery anodes using silicon nanowires. *Nature Nanotechnology*, 3:31–35, 2007.
- [13] P Chen, Z. Xiong, J. Luo, J. Lin, and K. Tan. Interaction of hydrogen with metal nitrides and imides. *Nature*, 420:302–304, 2002.
- [14] John W. Eaton. *GNU Octave Manual*. Network Theory Limited, 2002.
- [15] Paolo Giannozzi, Stefano de Gironcoli, Pasquale Pavone, and Stefano Baroni. Ab initio calculations of phonon dispersion in semiconductors. *Physical Review B*, 43:7231, 1990.
- [16] G. Girishkumar, B. McCloskey, A. C. Luntz, S. Swanson, and W. Wilcke. Lithium-air battery: Promise and challenges. *The Journal of Physical Chemistry Letters*, 1:2193–2203, 2010.
- [17] S. Gomes, H. Hagemann, and K. Yvon. Lithium boro-hydride LiBH_4 : raman spectroscopy. *Journal of Alloys and Compounds*, 346:206–210, 2002.
- [18] Stefan Grimme. Semiempirical gga-type density functional constructed with a long-range dispersion correction. *Journal of Computational Chemistry*, 27:1787–1799, 2006.
- [19] A. Gross, C. Ahn, S. Van Atta, P. Liu, and J. Vajo. Fabrication and hydrogen sorption behaviour of nanoparticulate MgH_2 incorporated in a porous carbon host. *Nanotechnology*, 20:204005, 2009.
- [20] A. Gross, J. Vajo, S. Van Atta, G. Olson, S. Skieth, and F. Mertens. Enhanced hydrogen storage kinetics of LiBH_4 in nanoporous carbon scaffolds. *Journal of Physical Chemistry C*, 112:5651, 2008.
- [21] S. Gunn and L. Green. The heats of formation at 25° of the crystalline hydrides and deuterides and aqueous hydroxides of lithium, sodium and potassium. *Journal of the American Chemical Society*. page 47824786, 1958.
- [22] D.R. Hamann. Generalized norm-conserving pseudopotentials. *Physical Review B*, 40:2980–2988, 1989.
- [23] G. Henkelman, A. Arnaldsson, and H. Jansson. A fast and robust algorithm for bader decomposition of charge density. *Computational Material Science*, 36:254–360, 2006.
- [24] P. Hohenberg and W. Kohn. Inhomogeneous electron gas. *Physical Review*, 136(3B):B864–B871, 1964.

- [25] J. Johnson and D. Sholl. DOE hydrogen program 2006 annual progress report, 2006.
- [26] U. Kasavajjula, C. Wang, and J. Appleby. Nano and bulk silicon based insertion anodes for lithium-ion secondary cells. *Journal of Power Sources*, 163:1003–1039, 2007.
- [27] C. Kim, S. Hwang, R. Bowman, Jr., J. Reiter, J. Zan, J. Kulleck, H. Kabbour, E. Majzoub, and V. Ozolins. LiSc(BH₄)₄ as a hydrogen storage material: Multi-nuclear high-resolution solid-state NMR and first-principles density functional theory studies. *Journal of Physical Chemistry*, 113:99569968, 2009.
- [28] Charles Kittel and Herbert Kroemer. *Thermal Physics Second Edition*. W. H. Freeman and company, New York, NY, 1980.
- [29] W. Kohn and L. J. Sham. Self-consistent equations including exchange and correlation effects. *Physical Review*, 140(4A):A1133–A1138, 1965.
- [30] G. Kresse and J. Furthmuller. Efficiency of ab-initio total energy calculations for metals and semiconductors using a plane-wave basis set. *Comput. Mat. Science*, 6:15, 1996.
- [31] G. Kresse and J. Furthmuller. Efficient iterative schemes for ab initio total-energy calculations using a plane-wave basis set. *Physical Review B*, 54:11169, 1996.
- [32] G. Kresse and J. Hafner. Ab initio molecular dynamics for liquid metals. *Physical Review B*, 47:558, 1993.
- [33] G. Kresse and J. Hafner. Ab initio molecular-dynamics simulation of the liquid-metalamorphous-semiconductor transition in germanium. *Physical Review B*, 49:14251, 1994.
- [34] G. Kresse and J. Joubert. From ultrasoft pseudopotentials to the projector augmented-wave method. *Physical Review B*, 59:1758, 1999.
- [35] X. Liu, D. Peaslee, C. J. Jost, and E. Majzoub. Controlling the decomposition pathway of libh₄ via confinement in highly ordered nanoporous carbon. *Journal of Physical Chemistry C*, 114:14036–14041, 2010.
- [36] W. Luo. LiNH₂-MgH₂: a viable hydrogen storage system. *Journals of Alloys and Compounds*, 381:284–287, 2004.

- [37] W. Luo and S. Sickafoose. Thermodynamic and structural characterization of the mglnh hydrogen storage system. *Journals of Alloys and Compounds*, 407:274–281, 2006.
- [38] H. Maekawa and M. Matsuo et al. Halide-Stabilized LiBH_4 , a Room-Temperature Lithium Fast-Ion Conductor. *JACS*, 134:894–895, 2009.
- [39] E. Majzoub, F. Zhou, and V. Ozolins. First-principles calculated phase diagram for nanoclusters in the na-al-h system: A single-step decomposition pathway for naalh₄. *Journal of Physical Chemistry C*, 115:2636, 2011.
- [40] E. H. Majzoub and E. Ronnebro. Crystal structures of calcium borohydride: Theory and experiment. *Journal of Physical Chemistry C*, 113:3352–3358, 2009.
- [41] E.H. Majzoub and K.J. Gross. Titanium-halide catalyst-precursors in sodium aluminum hydrides. *Journal of Alloys and Compounds*, 356-357:363–367, 2003.
- [42] E.H. Majzoub, Fei Zhou, and V. Ozolins. First-principles calculated phase diagram for nanoclusters in the na-al-h system: A single-step decomposition pathway for naalh₄. *Journal of Physical Chemistry C*, 115:26362643, 2011.
- [43] R. Malini, U. Uma, T. Sheela, M. Ganesan, and N.G. Renganathan. Conversion reactions: a new pathway to realise energy in lithium-ion battery–review. *Ionics*, 15:301–307, 2009.
- [44] Richard M Martin. *Electronic Structure: Basic Theory and Practical Methods*. Press syndicate of the University of Cambridge, New York, NY, 2004.
- [45] M. Matsuo, Y. Nakamori, S. Orimo, H. Maekawa, and H. Takamura. Lithium superionic conduction in lithium borohydride accompanied by structural transition. *Applied Physics Letters*, 91:224103, 2007.
- [46] M. Matsuo, A. Remhof, P. Martelli, R. Caputo, M. Ernst, Y. Miura, T. Sato, H. Oguchi, H. Maekawa, and H. Takamura. Complex hydrides with $(\text{BH}_4)^-$ and $(\text{NH}_2)^-$ anions as new lithium fast-ion conductors. *Journal of the American Chemical Society*, 131:1638916391, 2009.
- [47] P. Mauron, F. Buchter, O. Friedrichs, A. Remhof, M. Bielmann, C. Zwicky, and A. Zuttel. Stability and reversibility of LiBH_4 . *Journal of Physical Chemistry B*, 112:906–910, 2008.
- [48] P. Medeiros, F. Mota, A. Mascarenhas, and C. de Castillo. Adsorption of monovalent metal atoms on graphene: a theoretical approach. *Nanotechnology*, 21:115701, 2010.

- [49] K Miwa, N Ohba, and S. Towata. First-principles study on lithium borohydride LiBH_4 . *Physical Review B*, 69:241520, 2004.
- [50] R. Miyazaki, T. Karahashi, N. Kumatani, Y. Noda, M. Ando, H. Takamura, M. Matsuo, S. Orimo, and H. Maekawa. Room temperature lithium fast-ion conduction and phase relationship of LiI stabilized LiBH_4 . *Solid State Ionics*, 192:143–147, 2011.
- [51] I. Mochida, C. Ku, and Y. Korai. Anodic performance and insertion mechanism of hard carbons prepared from synthetic isotropic pitches. *Carbon*, 39:399–410, 2001.
- [52] Gholamabbas Nazri and Gianfranco Pistoia. *Lithium batteries: science and technology*. Kluwer Academic Publishers Group, Dordrecht, The Netherlands, 2004.
- [53] Peter Ngene, M. van Zwienen, and Petra E. de Jongh. Reversibility of the hydrogen desorption from LiBH_4 : a synergetic effect of nanoconfinement and Ni addition. *Chemical Communications*, 46:8201–8203, 2010.
- [54] T. Nielsen, K. Manickam, M. Hirscher, F. Besenbacher, and T. Jensen. Confinement of MgH_2 nanoclusters within nanoporous aerogel scaffold materials. *ACS Nano*, 3:35213528, 2009.
- [55] US Department of Energy Office of Energy Efficiency and Renewable Energy and The FreedomCAR and Fuel Partnership. Targets for onboard hydrogen storage systems for light-duty vehicles, 2009.
- [56] N. Ohba, K. Miwa, M. Aoki, T. Noritake, and S. Towata. First-principles study on the stability of intermediate compounds of LiBH_4 . *Physical Review B*, 74:075110–1–075110–7, 2006.
- [57] S. Orimo, Y. Nakamori, N. Ohba, K. Miwa, M. Aoki, S. Towata, and A. Zuttel. Experimental studies on intermediate compound of LiBH_4 . *Applied Physics Letters*, 89:021920, 2006.
- [58] Y. Oumellal, A. Rougier, and G. A. Nazri. Metal hydrides for lithium-ion batteries. *Nature Materials*, 7:916–921, 2008.
- [59] V. Ozolins and E. H. Majzoub. Prototype electrostatic ground state approach to predicting crystal structures of ionic compounds: Application to hydrogen storage materials. *Phys. Rev. B*, 77:104115, 2008.

- [60] V. Ozolins, E. H. Majzoub, and C. Wolverton. First-principles prediction of a ground state crystal structure of magnesium borohydride. *Phys. Rev. Lett.*, 100:135501, 2008.
- [61] V. Ozolins, E. H. Majzoub, and C. Wolverton. First-principles prediction of thermodynamically reversible hydrogen storage reactions in the li-mg-ca-b-h system. *Journal of American Chemical Society*, 131:230–237, 2008.
- [62] M. C. Payne, M. P. Teter, D. C. Allan, T. A. Arias, and J. D. Joannopoulos. Iterative minimization techniques for ab initio total-energy calculations: molecular dynamics and conjugate gradients. *Rev. Mod. Physics*, 64:1045–1097, 1992.
- [63] J. Perdew, J. Chevary, S Vosko, K. Jackson, M. Pederson, D. Singh, and C. Fiolhais. Atoms, molecules, solids, and surfaces: Applications of the generalized gradient approximation for exchange and correlation. *Physical Review B*. 46:6671, 1992.
- [64] J. Perdew, J. Chevary, S Vosko, K. Jackson, M. Pederson, D. Singh, and C. Fiolhais. Erratum: Atoms, molecules, solids, and surfaces: Applications of the generalized gradient approximation for exchange and correlation. *Physical Review B*, 48:4978, 1992.
- [65] F. Pinkerton, G. Meisner, M. Meyer, M. Balogh, and M. Kunderat. Hydrogen desorption exceeding ten weight percent from the new quaternary hydride $\text{Li}_3\text{BN}_2\text{H}_8$. *Journal of Physical Chemistry B*, 109:6–8, 2005.
- [66] Andrew Ritchie and Wilmont Howard. Recent developments and likely advances in lithium-ion batteries. *Journal of Power Sources*, 162:809812, 2006.
- [67] C. Rongeat, I. Llamas-Jansa, S. Doppiu, S. Deledda, A. Borgschulte, L. Schultz, and O. Gutfleisch. Determination of the heat of hydride formation/decomposition by high-pressure differential scanning calorimetry (hp-dsc). *Journal of Physical Chemistry B*, 111:13301–13306, 2007.
- [68] B. Rozdzyńska-Kielbik, W. Iwasieczko, H. Drulis, V.V. Pavlyuk, and H. Bala. Hydrogenation equilibria characteristics of $\text{LaNi}_{5-x}\text{Zn}_x$ intermetallics. *Journal of Alloys and Compounds*, 298:237–243, 2000.
- [69] Stephan Rudolph. Boron nitride, minerals review 2000. *The American Ceramic Society Bulletin*, 79:50, 2000.
- [70] Jean Schneider. Gnu linear programming kit. version 4.3. <http://www.gnu.org/software/glpk/glpk.htm>. Accessed 4/21/2011.

- [71] Yang Shao-Horn, Laurence Croguennec, Claude Delmas, E. Chris Nelson, and Michael A. O’Keefe. Atomic resolution of lithium ions in LiCoO_2 . *Nature Materials*, 2:462467, 2003.
- [72] L. Shclapbach and A. Zuttel. Hydrogen-storage materials for mobile applications. *Nature*, 414:353–358, 2001.
- [73] Donald J. Siegel, C. Wolverton, and V. Ozolin. First principles study of the crystal structure and dehydrogenation pathways of $\text{Li}_4\text{BN}_3\text{H}_{10}$. *Physical Review B*, 75:014101, 2007.
- [74] H. Smithson and C.A. Marianetti et al. First-principles study of the stability and electronic structure of metal hydrides. *Physical Review B*, 66:144107, 2002.
- [75] Grigorii Soloveichik. Metal borohydrides as hydrogen storage materials. *Material Matters*, 1933-9631, 2007.
- [76] J. Tarascon and M. Armand. Issues and challenges facing rechargeable lithium batteries. *Nature*, 414:359–367, 2001.
- [77] United States Energy Information Agency. US refinery yields, 2011. Accessed 5/22/2011.
- [78] F. Valencia, A. Romero, F. Ancilotto, and P. Silvestrelli. Lithium adsorption on graphite from density functional theory calculations. *Journal of Physical Chemistry B*, 110:14832–14841, 2006.
- [79] R. Wagemans, J. van Lenthe, P. de Jongh, A. van Dillen, and K. de Jong. Hydrogen storage in magnesium clusters: Quantum chemical study. *J. AM. CHEM. SOC.*, 127:16675–16680, 2005.
- [80] F. Wang and D. Landau. Determining the density of states for classical statistical models: A random walk algorithm to produce a flat histogram. *Physical Review E*, 64:056101, 2001.
- [81] L. Wang, S. Khare, V. Chirita, D. Johnson, A. Rockett, A. Frenkel, N. Mack, and R. Nuzzo. Origin of bulklike structure and bond length disorder of Pt_{37} and $\text{Pt}_6\text{Ru}_{31}$ clusters on carbon: Comparison of theory and experiment. *Journal of Physical Chemistry*, 128:131–142, 2005.
- [82] M. Winter and R. Brodd. What are batteries, fuel cells, and supercapacitors? *Chem. Rev.*, 104(10):4245–4269, 2004.

- [83] Y. Yah and J.Y. Zhang et al. First-principles study of high pressure phase transformations in Li_3n . *European Phys. J*, 61:397–403, 2008.
- [84] A. Zaluska, L. Zaluski, and J.O. Strom-Olsen. Structure, catalysis and atomic reactions on the nano-scale: a systematic approach to metal hydrides for hydrogen storage. *Applied Physics A*, 72:157–165, 2001.

VITA

Tim Mason was born in St. Louis, Missouri in 1979. In May, 2001 he received his B.S. in Electrical Engineering from the University of Tulsa. He worked first for Los Alamos National Laboratories in Los Alamos, New Mexico as a digital and analog circuit designer. He returned to St. Louis in May 2003 to work for the Boeing Company as a systems integration engineer until June 2010. During this time he completed his M.S. in Physics from the University of Missouri-St.Louis.